The art of soaking rocks: systematic study of liquid and solute flow in packed rock beds in the context of heap leaching

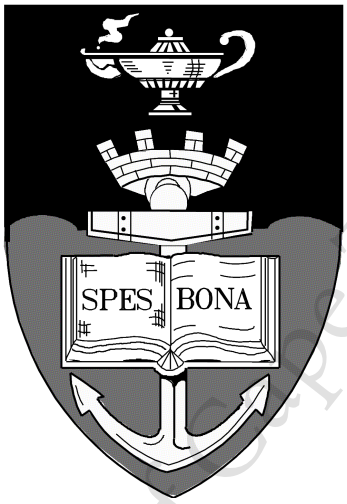

Alexey Cherkaev

Department of Chemical Engineering

Engineering and Built Environment Faculty

University of Cape Town

This dissertation is submitted for the degree of

Doctor of Philosophy in Chemical Engineering

February 2019

In memory of my late supervisor and mentor Prof. Ya.V. Tatarinov

Declaration

I, Alexey Cherkaev, declare that this thesis is my own work (except where acknowledgements indicate otherwise). Neither the whole work nor part thereof has been, is being, or is to be submitted for any degree or examination at any other university.

I empower the University of Cape Town to reproduce for the purposes of research either the whole or any part of the contents of this thesis, in any manner whatsoever.

Signature of candidate:

Signed by candidate

Signed on the 31st of January, 2019

Acknowledgements

This thesis would not have come to light without the help of many people who were involved in it directly or indirectly.

I would like to express my gratitude to my supervisor, Prof. Jochen Petersen, who allowed and provided the support for me to direct this project. I would like to thank him for his encouragement to explore different investigation avenues, patience at times of failure, and guidance to produce a composed thesis. I wish to thank all the members of the Hydromet group for their advice, constructive criticism and support. In particular, many thanks are due to Dr. James Mwase and Dr. Rahul Ram who helped me to run the experiments and Dr. Thandazile Moyo and Nicole Uys who helped me to bring this manuscript into a readable form.

I am grateful to my co-supervisor, Prof. Sue Harrison, for the financial support of the project and for her help and guidance with the experimental work. These thanks extend to the staff and the students of the CeBER lab. I wish to specially thank Emmanuel Ngoma and Tich Samkange who helped me to solve a multitude of technical issues with the rig, and Lesley Mostert who helped me get organised with various tasks that the project involved.

I would like to acknowledge SAMMRI for financial support of this project.

The data capturing setup for my rig was designed by Bill Randall and Kyle Hauslaib, for which I am grateful. I would also like to thank Prof. Jeremy Mann, Sandip Naik and Bernard Oostendorp who helped me to obtain and prepare the ore sample. I wish to thank Petrus van Staden and Prof. Mike Nicol for their advice on various aspects of the data analysis.

Я хочу отдельно поблагодарить моих родителей, Надежду и Владимира Черкаевых, и мою сестру, Наталию Черкаеву, за поддержку, терпение и заботу.

I owe a special gratitude to my wife, Dr. Bianca Cherkaev. Her love, encouragement and patience allowed me to finish this long journey.

Я посвящаю эту работу памяти моего первого научного руководителя, учителя с большой буквы и талантливого ученого Ярослава Всеволодовича Татаринова. Ярослав Всеволодович открыл для меня мир математики и исследования. И несмотря на то, что область этого исследования далека от неголономной механики, теории бифуркаций или Лоренц-инвариантной динамики, его успешное завершение оказалось бы невозможным без наставлений которые я в свое время получил от Ярослава Всеволодовича.

Abstract

Heap leaching is a technology for the low-cost processing of low-grade ores. Despite numerous advantages, its low efficiency — slow recovery rates and low mineral conversion — hinders its wider application. Reagent delivery to the mineral surface and product removal are key to achieving high efficiency. Both are governed by solution flow and solute transport phenomena. These phenomena are multi-scale in nature. Micro-scale transport (within the ore particle) has been investigated extensively, both experimentally and via modelling approaches. Macro-scale transport, on the other hand, has been studied predominantly using models. In this area, model calibrations are scarce and model validations are almost non-existent. While a few recent studies focused on flow visualisation, their main focus was the development of the technique and no systematic application was shown. Nonetheless, there is an indication that the flow occurs in a network of channels that cannot be approximated by the commonly used continuous models. In a heap leaching context, both modelling and experimental studies still fail to provide satisfactory answers about the effect of operation parameters, such as ore particle size distribution (PSD), heap height, solution flow rate, and aeration rate on metal recovery. This project aims to investigate the effect of PSD and the solution flow rate from a single drip emitter on the hydrodynamics of the heap. The study was conducted using both modelling and experimental approaches. Models play the role of condensed formalised understanding of a process. They help to guide the experimental work in validating models results. At the same time, they arise from experimental data analysis as our understanding improves.

Our understanding of the flow through packed rock beds is based on the theory of unsaturated flow through porous media. This theory was first developed in applications for oil extraction and then adapted for soil hydrology studies. The foundation of the theory is the Richards equation coupled with semi-empirical material relations. This equation can help to find liquid distribution and its local velocities in the domain based on the solid matrix properties and boundary conditions. As it is a highly

non-linear equation, it is difficult to investigate the properties of its solutions directly. Some reasonable assumptions, such as a steady-state or initially uniform liquid content for drainage problems, provide considerable simplifications making it amenable to a deeper mathematical analysis. Reducing the model analysis to two dimensions at steady state resulted in the derivation of constraints on the capillary pressure gradient that must be satisfied at every point of the medium. Further simplification resulted in the formulation of a one-dimensional steady-state uniform model (SSUM). With the help of this model it was shown that saturation is insensitive to the inlet flow rate, but it is highly sensitive to a parameter that represents the internal matrix structure. The dynamic behaviour during infiltration and drainage was demonstrated using a transient one-element model (TOEM).

The results of these simplified models were validated using a numerical solution of the Richards equation in one- and two-dimensional domains. The two-dimensional model was also used to demonstrate the flow configuration in the presence of a hydraulic barrier, an area with low conductivity. The results demonstrated by the models are direct consequences of the unsaturated flow theory, according to which the liquid is moving due to effects of gravity and capillary forces. Experimental validation of these results provides validation for the theory and it can help to find the correspondence between ore properties and hydraulic parameters.

Experimental work was designed to test the effect of PSD and the inlet flow rate on the liquid hold-up and to characterise the flow. Various blends of a gold ore were prepared with varying content of -1.4 mm particles (referred as "fines"): from 0 wt% to 48 wt%. The ore was packed into cylindrical columns and suspended on load cells. Inlet flow rates ranged from about 2 to 45 $\mathrm{L \cdot m^{-2} \cdot h^{-1}}$, encompassing and greatly exceeding the flow rates used in heap leach practice. The inlet solution was administered by a single drip emitter placed at the top of the packing on the cylindrical column axis. To achieve steady-state flow in a reasonable time, the columns were flooded and drained prior to the start of the experiments. The liquid hold-up was investigated using gravimetric studies, whereas the information on the liquid flow was obtained by residence time distribution (RTD) studies. For gravimetric studies, each packing was subjected to a fixed inlet flow rate, until its weight reached a steady value which was recorded. Then the experiment was repeated at another flow rate. The recorded steady-state weights were converted to liquid content. Furthermore, time-dependent final drainage was recorded over 24 and 48 hours. RTD studies used the inflow step-change in the concentration of the chemical tracer, potassium nitrate. Each study was performed with step-up and step-down of the

tracer concentration. The outflow concentration was measured using a conductivity meter.

The steady-state gravimetric results confirmed the hypothesis of the liquid hold-up insensitivity towards the variation of the inlet flow rate. Furthermore, the strong dependency of liquid content on PSD was observed. Fast imbibition and slow drainage predicted by the TOEM were confirmed in the experiment. Experimental results, however, could not be successfully reconciled with either steady-state or one-element models. It was further established that there was extremely high uncertainty in the calibrated hydraulic parameter values due to the resulting narrow range of liquid content change in each experiment. This points to the inadequacy of the Richards equation in heap leaching systems. The core reason for this is small variation of water content with the change in inlet flow rate within heap leach operating conditions. An alternative model relating PSD to water content under low irrigation flow rates was developed. It was proposed that variation in liquid hold-up can be accounted for if it is assumed that the liquid encircles all ore particles, except for ultra-fines that either remain attached to larger particles or suspended in the liquid phase. Thus, the liquid content must be proportional to the total area of solids in the packing. The experimental results show good agreement with this model. The model calibration has established that -0.265 mm particles can be categorised as "ultra-fines". The model was further validated against experimental data from literature and industry.

The F-curves from RTD experiments could not be compared directly, as effective volumes of packings were different due to different water contents. However, correction for the working reactor volume and inlet flow rate unified the curves. The shape of most of the curves resembled the RTD curve of a CSTR or of two-CSTRs-in-parallel. This, however, presents an unrealistic picture since there is no active mixing present. An alternative view was proposed, that comprises different length Plug-Flow Reactors connected in Parallel (PFRP). This model shows that although an RTD study may result in a curve closely resembling a CSTR, this reactor can exhibit very different behaviour compared to a true CSTR if non-linear mineral dissolution kinetics is considered.

Considering the inadequacy of the Richards equation model to describe the flow in packed rock beds, a different approach to describe the flow is offered. According to this approach, the solid matrix is represented by a grid of interconnected pores. Individual liquid particles can move between these pores. Each pore, depending on its current liquid content, may expel or keep a liquid particle. This decision is made probabilistically, with increased probability of expelling the particle if the pore liquid content is high. Furthermore, this model can include pores with different hydrodynamics. For example,

a wide pore in the solid matrix would generally conduct the liquid with ease, but, due to relatively low capillary forces, will not be able to retain high liquid content ("body pore"). In contrast, a narrow pore would retain more liquid, but has lower hydraulic conductivity near saturation point ("throat pore"). These properties can be encoded in pores by assigning different probabilities of accepting or expelling liquid particles. It is proposed that this model can better connect solid matrix properties, such as PSD or particle morphology, and hydraulic responses, compared to the Richards equation models. Validation of this proposition, however, lies outside the scope of this study.

This research project provides an initial systematic study of the hydrodynamics of heap leaching that combines modelling and experimental approaches. A model connecting steady-state liquid content and PSD of the ore was proposed and validated. Inadequacy of the commonly used Richards equation-based models was demonstrated. The idea of the solution flowing in channels was further solidified. For future work, the results of this study need to be tested against the experiments using ores with different mineralogies and particle morphologies and conducted at a larger scale.

Contents

Contents vii

List of Figures xiii

List of Tables xviii

Chapter I Introduction 1

§ 1 Transport phenomena in heap leaching 1

§ 2 Heap leaching practice 3

1 The ore bed. 3

2 Heap irrigation. 5

§ 3 Macro-scale theory of solution transport in packed rock beds 5

1 The details of micro-scale mechanics. 5

2 Darcy's law. 6

3 The Richards equation. 7

4 Material properties: unsaturated model. 8

5 Boundary conditions (BC). 10

6 Solution of the Richards equation. 11

7 Extensions of the Richards equation. 12

8 Preferential flow. 12

§ 4 Theory of solute transport 13

1 Advection-dispersion equation. 13

2 On the dispersion coefficient. 13

3 Advection-diffusion models. 14

4 Compartment models 15
§ 5 Experimental data 16
1 Model calibration. 16
2 Model validation. 16
3 Experimental studies on preferential flow. 17
4 Direct flow observations: tomography techniques 17
§ 6 Problem statement 19

Chapter II Hydraulic models for heap leaching **21**
§ 1 The Richards equation model in 2D: problem statement 21
1 Domain 21
2 The Richards equation 22
3 Boundary conditions, ... 23
4 Initial saturation 23
5 Effects that are investigated. 23
§ 2 Two-dimensional steady-state Richards' equation 24
§ 3 The steady-state uniform model (SSUM) 27
1 Solution. 27
2 Stability of the steady-state solution. Solution dependence on model parameters. 29
§ 4 Transient one-element model (TOEM) 33
§ 5 Numerical solution of the one-dimensional Richards equation 36
1 Formulation. Finite volumes scheme. 36
2 Infiltration curve. 38
3 Independence from the mesh. 40
4 Drainage. 40
5 Intermittent flow. 41
6 Hydraulic parameter perturbation. 44
§ 6 Numerical solution of the two-dimensional Richards equation: Richards2D model . 46
1 Finite volumes scheme. 47
2 Single drip emitter position. 48

3 Channelling effect. . . . 50
4 Barrier. . . . 50
5 Modelling of the experiment by Wu et al. (2007). . . . 50
§ 7 Advection-dispersion model of the solute transport . . . 54
§ 8 Simple compartment models . . . 56
1 Two CSTRs in parallel (2-CTSR-P). . . . 58
2 CSTR-dead volume reactor. . . . 58
3 Multiple CSTR in series (N-CSTR-S). . . . 59
4 Stacked two CSTR in parallel (Stacked-2CSTR-P). . . . 60
§ 9 Plug-flow reactors in parallel (PFRP) . . . 61
1 Rationale and description. . . . 61
2 Numerical scheme. . . . 67
3 Model results . . . 71
§ 10 Summary . . . 72

Chapter III Experimental materials and methods **74**

§ 1 Materials . . . 74
1 Ore. . . . 74
2 Solution composition. Tracer. . . . 75
§ 2 Apparatus . . . 75
1 Columns. . . . 75
2 Load cell. . . . 76
3 Pump. . . . 76
4 Conductivity cell. . . . 76
5 Conductivity meter. . . . 77
§ 3 Methods . . . 78
1 Particle size distributions. . . . 78
2 Fines distribution. . . . 78
3 Agglomeration. . . . 80
4 Packing. . . . 80

5 Flooding and drainage. . . . 80
6 Infiltration studies. . . . 81
7 Steady-state gravimetric studies 81
8 Note on hysteresis. . . . 81
9 Final drainage. . . . 82
10 Intermittent infiltration studies. . . . 82
11 Conductivity meter calibration. . . . 82
12 Residence time distribution (RTD) studies. . . . 83
13 Experimental matrix. . . . 84

Chapter IV Experimental results and discussion **87**

§ 1 Preliminary and side experiments 88
1 Column flooding. . . . 88
2 Hysteresis. . . . 88
§ 2 Solution flow results 90
1 Summary of steady-state results. . . . 90
2 Infiltration curves. . . . 90
3 Intermittent infiltration. . . . 91
4 Drainage. . . . 91
§ 3 Solution flow discussion based on the Richards equation model 93
1 Choice of residual water content ϑ_r. . . . 93
2 Application of the steady-state uniform model (SSUM) to experimental data. 94
3 Application of the transient one-element model (TOEM) to the experimental data. . . . 96
§ 4 A novel model for the steady-state liquid hold-up 102
1 Model assumptions. . . . 102
2 Model derivation. . . . 104
3 Cut-off minimum size. Specific surface area for GGS. . . . 105
4 Specific area of blends. . . . 106
5 Average water content. . . . 109

6 Model calibration. . . . 109
7 Validation against independent data. . . . 110
§ 5 Solute transport results . . . 112
1 The dataset from the first experiment. . . . 112
2 Raw RTD results. . . . 112
3 Dimensionless form. . . . 115
4 Comparison with the literature. . . . 116
§ 6 Discussion of solute transport . . . 117
1 Advection-dispersion model (ADM) . . . 117
2 Single CSTR and 2-CSTR in parallel. . . . 117
3 *E*-curves, . . . 118
4 PFRP to rescue. . . . 121
§ 7 Potential route forward: stochastic pore model . . . 122
1 Domain: lattice. . . . 122
2 Time . . . 124
3 Irrigation . . . 124
4 Simulation : rules. . . . 124
5 Particle residence time. . . . 125
6 Results. . . . 125

Chapter V Conclusions **128**

§ 1 Key findings . . . 129
1 The Richards equation models. . . . 129
2 Liquid hold-up model. . . . 129
3 Solute flow. . . . 130
§ 2 Future work . . . 130
1 Further validation of liquid hold-up model. Model improvements. . . . 130
2 PFRP validation. . . . 131
3 Stochastic pore model improvements. . . . 131
4 Addressing experimental caveats. . . . 131

5 Initial infiltration, final drainage and hysteresis. 132

Bibliography **133**

A Program listings **145**

B Gravimetric data **148**

C RTD data **149**

List of Figures

I.1 Schematic diagram of a heap. 4

I.2 Comparison of a hypothetical coarse and fine material hydraulic conductivity curve. . . . 10

I.3 PET image of the solution flow though a small column packed with ore obtained during preliminary studies by the author (published in Petersen, 2015). The white frame indicates the boundary of the column. 18

II.1 Rectangular 2D domain can be mapped to trapezoid or even curve-shaped domain by the coordinate transformation. 23

II.2 Graphical representation of the constraint on the capillary pressure gradient for the steady-state problem II.7. 26

II.3 Infiltration and drainage curves of the transient one-element model run with parameters listed in Table II.1. 35

II.4 The results of TOEM with increased and decreased inlet flow rate. The dashed line shows a steady-state saturation at the original (and final) flow rate. 36

II.5 Example of the model run with parameters shown in Table II.2: (a) variation of saturation with depth at different time points and (b) variation of saturation with time for different depths. 39

II.6 Model results on different mesh sizes showing independence of the model from the mesh size. 40

II.7 Variance of saturation (a) with depth at different time points and (b) with time for the top element for the drainage simulation with parameters of Table II.2 with exception of $q_{\text{in}} = 0$, $s_0 = 0.28$ and $t_{\text{max}} = 48$ hours. 41

II.8 Infiltration curve of the dimensionless model with parameters listed in Table II.3 for intermittent flow with short "on" and "off" intervals. 43
II.9 Infiltration curve of the dimensionless model for intermittent flow with the parameters listed in Table II.3 except for $\tau_{on} = 10^5$ and $\tau_{off} = 3 \times 10^5$, approximately equivalent to 5 hours "on" and 15 hours "off" for the parameters of Table II.2, and longer simulation time. 44
II.10 Predicted relative flow rate out of the column for the intermittent inlet flow with long "on" and "off" periods of irrigation ($\tau_{on} = 10^5$ and $\tau_{off} = 3 \times 10^5$ respectively). 44
II.11 An example of the results of the perturbed model with the base parameters listed in Table II.2 with each of $\lg(q_{in}/K_s)$, α and s_0 randomly perturbed by maximum of $\pm 5\%$ (compare with the results of unperturbed model in Figure II.5). 45
II.12 Saturation distribution with increased depth for the model with the base parameters listed in Table II.2 and with parameter n (and, as a result, $m = 1 - 1/n$ as well) perturbed by 5% at each element boundary. 46
II.13 Saturation profile according to the Richards2D model with base parameters at time $t = 8$ h. 49
II.14 Saturation profile according to the Richards2D model with base parameters at time $t =$ 8 h and single drip emitter placed on the left. 49
II.15 The effect of a highly conductive channel on the saturation profile. 50
II.16 The effect of an impermeable barrier in the domain on the saturation profile. 51
II.17 Richards2D model results with impermeable barrier with a single narrow opening in it. . . 51
II.18 Saturation distribution in a model following Wu et al. (2007) experiment. 53
II.19 Result from the approximated solution of the advection-dispersion equation. 55
II.20 Results of the numerical solution of the advection-dispersion equation at $\zeta = 1$ and different Péclet numbers. 56
II.21 Ideal plug-flow reactor concentration profile. 57
II.22 Concentration over time from an ideal CSTR. 57
II.23 Comparison of a single CSTR model and 2-CSTR-P. 59
II.24 Comparison of N-CSTR-S and ADM for various number of CSTRs and Péclet numbers respectively. 60

II.25 Concentration outputs from levels 1 to 3 of the Stacked-2CSTR-P model with $\nu_1 = 3/4$ and $q_1 = 1/4$. 61
II.26 CSTR and PFRP model comparison: no reaction. 72
II.27 Concentration inside the plug-flow reactor in absence of a reaction at different time points. The second order approximation together with fine mesh help to keep numerical diffusion to a minimum. 72
II.28 Mineral conversion differences between CSTR and PFRP model run with the same parameters. 73

III.1 Cataloguing the weight fractions of the ore sample. Photo is courtesy of Bernard Oostendorp. 75
III.2 Schematic drawing of the column and the picture of the reactor with four columns. . . . 76
III.3 Schematic of the conductivity cell: A is the funnel collecting the outflow solution from the column, B is a working chamber with electrodes, C is the outflow opening, and D is the cap with the electrodes that fits tightly into the chamber B with two electrodes mounted on to it. 77
III.4 The photographic picture of the conductivity cell. 77
III.5 Example of CDF curves of GGS distribution with various values of the parameter λ. . . 79
III.6 CDF curves for true GGS distribution with $\lambda = 0.97$ and for GGS097(P14). 79
III.7 PSD of -1.4 mm fraction of the sample. 80
III.8 An example of the conductivity meter calibration curve. 83
III.9 Experimental procedure diagram. The approximate durations of each experimental step are encoded by colour: blue denotes the step that lasted one day, orange — two days, and green — five days. The final drainage lasted one day for some experiments and two days for others. 85

IV.1 Hysteresis demonstrated by different liquid hold-ups at the same flow rates depending whether the rate was increased (step-up, infiltration) or decreased (step-down, drainage). The minimum weight value for each chart is set to the dry packed column weight emphasizing the overall liquid gain. 89

IV.2 Steady-state experiments results showing little effect of different flow rates on water content. There is, however, a significant effect of PSD. 90
IV.3 Example of the infiltration curve starting from some initial saturation (after two-day drainage), conducted at a flow rate of 40 $\mathrm{L} \cdot \mathrm{m}^{-2} \cdot \mathrm{h}^{-1}$. The smallest value of the y-axis on each chart is selected to be the dry column weight. The curve of the GGS075(P11) chart has a dip due to tubing breakage that occurred two hours after the start of the experiment. 92
IV.4 Results of intermittent flow experiments of columns that were not previously flooded. . . 92
IV.5 Results of the drainage experiment for the columns of the three sets. 93
IV.6 Contour plots of the penalty function for GGS075(P11) and GGS075(P21) data with the light red and light green points showing the identified minimum for P11 and P21. These plot suggest no confident minimum of the penalty function can be determined from the experimental data. 96
IV.7 Dependence of saturation on hydraulic parameters n and $\hbar$. 97
IV.8 Jacobian A of ODE (II.10) as a function of hydraulic parameters n and $\hbar$. 97
IV.9 Comparison of the drainage experimental data and the results of TOEM with parameters listed in Table IV.3 for the first set of columns. Solid blue line refers to the model results. Dotted red line is showing experimental data. 98
IV.10 Comparison of the drainage experimental data and the results of TOEM with parameters listed in Table IV.3 for the second set of columns. 99
IV.11 Result of calibration of TOEM for the first set of experiments. 100
IV.12 Results of calibration of TOEM for the second set of experiments. 100
IV.13 Comparison of steady-state saturations between the model and experimental results for the first set of experiments. The model parameters were set by fitting drainage data. . . . 101
IV.14 Comparison of steady-state saturations between the model and experimental results for the second set of experiments. The model parameters were set by fitting drainage data. . 102
IV.15 Comparison of water content and specific area for various Ξ/ξ ratios. All cases demonstrate a reasonable fit to a straight line. 110
IV.16 Comparison of the experimental data obtained in this study with the data from the literature and from industry using the cut-off size $\xi = 0.265$ mm. 111

IV.17 Conductivity measurement and its conversion to concentration for the first set of RTD studies. . . . 113
IV.18 F-curve for columns GGS025(P12) and GGS097(P14) at 3 $L \cdot m^{-2} \cdot h^{-1}$. . . . 114
IV.19 F-curve for columns GGS075(P11), GGS025(P12) and GGS097(P14) at 20 $L \cdot m^{-2} \cdot h^{-1}$. 114
IV.20 F-curve for columns GGS075(P21)–GGS040(P24) at 3 $L \cdot m^{-2} \cdot h^{-1}$. . . . 115
IV.21 F-curve for columns GGS075(P21)–GGS040(P22) at 10 $L \cdot m^{-2} \cdot h^{-1}$. . . . 115
IV.22 Unitless form of F-curves for all step-down experiments. No legend is given as the main purpose is to demonstrate the congruence of these curves. . . . 116
IV.23 Comparison of the RTD experiments results with the results of Bouffard and Dixon (2001) and Dixon and Afewu (2010). . . . 117
IV.24 Comparison of ADM with experimental data for various Péclet numbers. . . . 118
IV.25 Comparison of a single CSTR model and RTD experiments. . . . 118
IV.26 Comparison of 2-CSTR in parallel, single CSTR and experimental data. . . . 119
IV.27 E-curves for all step-down experiments. . . . 120
IV.28 The selection of E-curves forming a bundle. . . . 120
IV.29 The outliers among the E-curves. . . . 120
IV.30 Comparison of the experimental E-curves with the selected models. . . . 121
IV.31 Graphical representation of the domain lattice with each line being a bond and each point being a site. . . . 123
IV.32 Screenshot of the running program. . . . 126
IV.33 Example of the stochastic model results: (a) liquid hold-up and (b) RTD. Flow was stopped at time step 3714. . . . 126

List of Tables

I.1 Comparison of hydraulic parameters (van Genuchten model) reported for different ores. The value of van Genuchten parameter m for Mantoverde ore was fitted independently of n, instead of using $m = 1 - 1/n$. 17

II.1 Typical parameters for the simple transient model. 35

II.2 Parameters used for infiltration simulation. 39

II.3 Dimensionless model parameters, roughly equivalent to parameters listed in Table II.2, for intermittent flow with short "on" and "off" intervals. 43

II.4 Base parameter values of Richards2D model 48

II.5 52

II.6 Parameters for PFRP model simulation. 71

III.1 Overview of the experimental matrix. 85

IV.1 Results of the flooding stage of the experiments. 88

IV.2 Comparison of two heuristic rules to choose residual water content from drainage data. . 94

IV.3 Experimentally determined values of hydraulic parameters K_s and m. 95

IV.4 Sensitivities of saturation towards the change of hydraulic parameters for experiments and inlet flow rate $q_{\text{in}} = 5\ \text{L} \cdot \text{m}^{-2} \cdot \text{h}^{-1}$. 96

IV.5 Experimentally determined values of hydraulic parameters K_s and m from drainage data. 99

IV.6 Specific area calculated for PSD blends used in the experiments. Relative specific area a_r is the fraction of the area when compared with GGS075 blend. 107

IV.7 Ratio of the relative specific area change with the change of ξ. 109

IV.8 Example of stochastic model parameters. 125

Nomenclature

α	The inverse of bubbling pressure
CDF	Cumulative distribution function
c_j	Concentration of species j
$\mathbf{D}$	Dispersion tensor
$\mathfrak{D}$	Molecular diffusivity
$\partial\Omega$	Boundary of the domain
$\Delta\vartheta$	Difference between saturated and residual water content
$F(t)$	F-curve of residence time distribution
ϕ	Rock bed porosity
$\mathbf{\Gamma}$	Relative perturbance matrix
GGS	Gates-Gaudin-Schumann
GGSxxx(Pyz)	Experiment identification: "xxx" is GGS parameter, "y" is the experiment set number and "z" is the number of the experiment within the set
H	Vertical dimension of the domain (height)
h	Capillary pressure expressed in meters
s	Effective saturation

$\mathbf{K}$	Tensor of hydraulic conductivity
$\mathbf{k}$	Tensor of hydraulic permeability
K_r	Relative hydraulic conductivity
$\mathbf{K}_s$	Saturated hydraulic conductivity
$\mathscr{k} = q_{\text{in}}/K_s$	Fraction of the flooding rate
ℓ	Mualem hydraulic parameter, usually assumed to be $1/2$
λ	GGS distribution parameter
m	Van Genuchten model fitting parameter
n	Van Genuchten model fitting parameter
Ω	Spatial domain
$\mathscr{P}$	Cumulative probability function (CDF)
$\mathscr{p}$	probability density function (PDF)
PDF	Probability distribution function
PSD	Particle size distribution
ϑ	Water content: ratio of watrer volume to the total volume of the medium
Q	Volumetric flow rate
q_{in}	Inlet flow rate
ϑ_r	Residual water content
ϑ_s	Saturated water content
RTD	Residence time distribution
$\mathbf{\Sigma}$	Relative perturbance matrix for ODE

τ	Dimensionless time
$\Theta(x)$	Heaviside theta-function (step-function).
$\boldsymbol{V}$	Specific discharge (superficial velocity)
v	Advective velocity
W	Horizontal dimension of the domain (width)
Ξ	Lagest particle size
ζ	Dimensionless vertical coordinate

Chapter I

Introduction

§ 1. Transport phenomena in heap leaching

The global demand for metals and the depletion of the known reserves push mining companies to process refractory ores and ores with lower metal grades or more complex mineralogy (Bennett et al., 2012; Deloitte, 2013; Arezki et al., 2015). Conventional methods, either pyro-metallurgical or tank-leaching, may become uneconomical for such ores. Heap leaching presents an alternative particularly suited for low-grade ores.

To understand heap leaching technology, it is informative to consider its development using copper as an example. For a long time copper oxide ores were the main minerals used to extract copper. However, it is difficult to upgrade these ores using flotation. Thus, only high grade copper oxide ores were processed and low grade material was sent to waste dumps. Heap leaching started as dump leaching from these waste piles (Roman et al., 1974; John, 2011). It was later realised that more value can be extracted using relatively inexpensive ore crushing and leaching pad preparation. Introduction of the solvent extraction (SX) process to selectively recover copper from leach liquors further improved heap leaching efficiency. As oxides became depleted, heap leaching was further developed to use bio-leaching to extract copper from secondary sulphide minerals in low-grade ores[1]. Because of a combination of mass transfer and reaction rate constraints, heap bio-leaching is a considerably slower process (Dixon, 2003; Watling, 2006). Heap bio-leaching faces further challenges in processing primary

[1] Prior to the development of bio-leaching, Rio Tinto was using roasting together with heap leaching to extract copper since the 18th century (John, 2011).

sulphides, such as chalcopyrite, due to particularly slow reaction kinetics.

Despite the noticeable advantages of heap leaching to process low grade ores, its low efficiency and incomplete metal recovery remain main prohibitive factors for wider adoption of the process. Slow recovery rates mean delayed returns on investment and require large inventory to make the process profitable. This, in turn, results in higher capital cost. Reagent delivery to the mineral surface and product removal from the heap are key to achieving higher efficiency. Both of the processes are governed by the solution flow and solute transport phenomena that are multi-scale in nature.

The micro-scale is the scale of individual mineral grains with mineral dissolution kinetics being a limiting factor. In oxide leaching, since the reaction rates are fast, the dissolution is often constrained by mass transfer through the liquid film (Roman et al., 1974; Levenspiel, 1999). In oxidative leaching, reaction kinetics restriction may result in the process being reaction controlled (Petersen and Dixon, 2007). Since the products of the reactions are usually liquid, the mineral grain dissolution is approximated by the shrinking sphere model (Roman et al., 1974). If the distribution of spheres of different sizes is considered, an efficient model governing mineral dissolution rate can be formulated as

$$\frac{\partial X}{\partial t} = (1 - X)^{\varphi},$$

where φ is a fitting parameter dependent on size distribution (Dixon, 1992).

The meso-scale transport is concerned with the reagent transfer from the bulk leaching solution to the mineral surface and the reverse transport of the product. These phenomena are governed by the diffusion inside ore particles or particle agglomerates (Ogbonna, 2006). The diffusion process is often simplified using the shrinking core model. However, recent studies have shown that there is very shallow reagent penetration in large particles (Ghorbani et al., 2013) and the use of a simplified model may be incorrect.

Solution and reagent distribution within a packed rock bed represents macro-scale transport phenomena. Solution flows downwards due to gravity and disperses into the solid matrix due to capillary forces. If the solution flows through a dry matrix, it needs to partially displace the air present in the pores. A solute follows the flow of the solution but also undergoes an additional dispersion due to micro-differences in liquid velocities (Bear, 1969; McBride et al., 2006; Dixon and Afewu, 2010; Bear, 2018).

The phenomena at each scale have been studied independently in various engineering and scientific

fields (Bear and Verruijt, 1987; Levenspiel, 1999; Ogbonna et al., 2005). However, the extent of the studies specific for heap leaching is not uniform across the scales. Micro-scale mineral dissolution kinetics have been extensively studied at the laboratory scale and is an active area of research for the leaching of refractory minerals, such as chalcopyrite (Watling, 2013, 2014). Meso-scale transport has seen growing attention, with recent studies focussing on experimental validation of previously formulated models (see, for example, Ghorbani et al., 2013). The study of macro-scale transport in heaps has almost exclusively been confined to modelling work. Very few studies have gone as far as to calibrate proposed models. Even fewer actually validated their models (Petersen and Dixon, 2007; van Staden et al., 2017). It must be noted, a few recent studies focused on flow visualisation (Fagan et al., 2013; Ilankoon et al., 2013; Petersen, 2015). However, the focus of these studies was the development of the visualisation technique and no systematic conclusions regarding actual flow were drawn. Nonetheless, there is an indication from these studies that the liquid flow occurs in a network of relatively isolated channels occupying a small volume. This conceptual picture, however, contradicts currently widely used mathematical model based on the Richards equation in which the solution is assumed to be continuously distributed through the solid matrix with continuously distributed local velocities.

This work focuses on macro-scale transport since it has the least established knowledge base. It aims to provide the bridge between the theory (model) and experiments for materials and conditions typical to heap leaching. To find the location for this "bridge", the practice of heap leaching related to solution transport, solution transport theory and existing experimental results need to be examined.

§ 2. Heap leaching practice

1. The ore bed. The mineral dissolution rate is proportional to the exposed mineral surface. To achieve higher mineral surface, run-of-mine ore is usually crushed to -25 mm (1 inch). While the finer crushing results in higher leaching efficiency, it increases the cost of crushing and may cause bed clogging or mechanical instability due to high liquid saturation. Overall, the ore particle size distribution (PSD) is dependent on a particular ore and crusher settings (John, 2011).

It is common to agglomerate the ore prior its stacking. During the agglomeration the ore is mixed with a small amount of liquid and maybe a binding agent such as sulphuric acid or cement (Bouf-

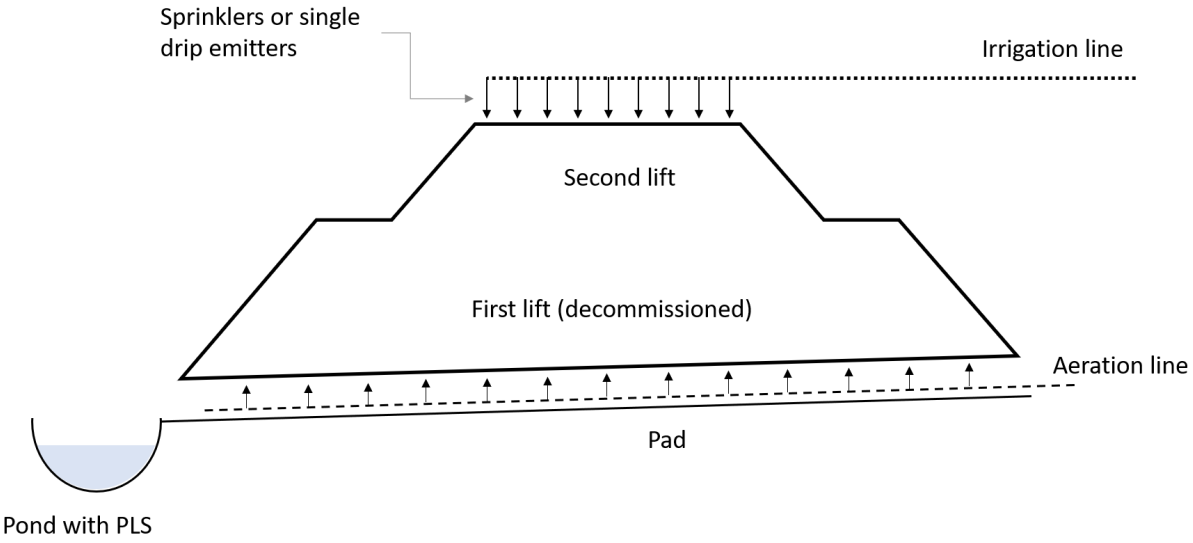

Figure I.1: Schematic diagram of a heap.

fard, 2008). The presence of liquid creates strong capillary forces. This results in the formation of lumps containing multiple particles stuck together. If these lumps are viewed as individual particles, agglomeration effectively narrows PSD. Agglomeration is generally practised for ores with a high fines content.

The pad for the heap is prepared on a slope to ease the collection of the outflow solution (commonly known as pregnant leach solution, PLS). To prevent solution seepage into the ground, the pad is covered with an impermeable material. Due to the active role oxygen plays in bio-leaching, heap bio-leaching pads contain aeration lines to provide airflow through the heaps. Finally, a layer of coarse material is put on the pad to facilitate solution drainage (John, 2011).

The ore is placed on the prepared pad using either a conveyor belt or by dumping it from trucks. The latter is discouraged as truck paths cause ore compaction that may result in a problematic heap hydrology. To minimise the land use, a heap may be located on the top of a decommissioned heap, creating multiple lifts. The heap height varies from 6 to 30 m. Higher heaps minimise the land use, more efficiently utilises other equipment used, such as solution sprinklers, and helps to conserve heat. However, it can also cause considerable ore compaction disrupting solution flow and aeration, especially in lower lifts (Figure I.1).

2. Heap irrigation. The solution with the dissolved reagents — known as *barren solution* containing acid, ferric sulphate or cyanide depending on the particular ore and the process — is administered at the top of the heap by a grid of sprinklers or drip emitters (Ghorbani et al., 2015). The former were found to lead to development of ponding and excess water loses due to evaporation and, thus, were mostly replaced by drip emitters. A typical superficial flow rate of the heap leaching lies in the range of 3–10 $\mathrm{L} \cdot \mathrm{m}^{-2} \cdot \mathrm{h}^{-1}$. Due to a large space between individual drip emitters, actual flow rate from a single drip emitter may be as high as 10 $\mathrm{L} \cdot \mathrm{h}^{-1}$. As the liquid moves through the heap, dissolved reagents react with minerals in the ore, dissolving the metals and forming what is known as a *pregnant leach solution* (PLS). At the bottom of the heap PLS flows down the slope of the pad and it is collected in the pond for downstream processing (see Figure I.1).

The liquid moves inside the bed through the network of pores formed by the space between the solids. There are two main forces acting on each small liquid element: gravity pulling it downwards and capillary forces, induced by liquid surface tension at the liquid-air interface. The droplet moves towards the location with the highest pull. The theoretical macro-scale description of this movement is discussed next.

§ 3. Macro-scale theory of solution transport in packed rock beds

1. The details of micro-scale mechanics. Formulation of the macro-scale theory becomes clearer once micro-scale effects are examined. Primarily, the comparison of gravity and capillary pulls that a liquid droplet can experience needs to be examined.

Based on the interaction with the solid, the liquid can be classified as wetting if the liquid maximises its contact surface with the a given solid, otherwise it is non-wetting. In the case of aqueous solution flow in heaps, the water solution is considered wetting liquid whereas air is non-wetting. Furthermore, when water in the pore also comes into contact with air, the surface tension at the liquid-gas interface results in a pressure drop across this interface. This pressure drop is referred as *capillary pressure*, which depends on the magnitude of the surface tension, contact angle with the solid, and pore radius. It is

expressed as (Extrand, 2015)

$$p_c = \frac{2\gamma \cos\theta}{r},$$

where p_c is capillary pressure, θ is liquid-solid contact angle, γ is surface tension and r is pore radius. Surface tension γ is a function of temperature and can be expressed as follows (Petrova, 2014):

$$\gamma = 235.8 \left(1 - \frac{T}{T_C}\right)^{1.256} \left[1 - 0.625 \left(1 - \frac{T}{T_C}\right)\right] \quad \text{mN} \cdot \text{m}^{-1},$$

where T and $T_C = 647.096$ K are temperature and critical temperature in Kelvin respectively. This expression is valid for pure water in the temperature range from 0.01 C° to critical temperature $T_C = 374.096$ C°. Using this expression and assuming $\theta \approx 0$, capillary pressure at 20°C can be approximated as follows:

$$p_c \approx \frac{100}{r} \quad \text{Pa},$$

where radius r is in millimetre. It implies that a 1 mm pore can hold approximately a 10 mm high column of water[2]. If the height of liquid in such a pore exceeds 10 mm, the excess water will drain.

2. Darcy's law. Although it is possible to consider the flow through individual pores in packed rock beds (see Jafari et al., 2008; Augier et al., 2010; Barker et al., 2012), there are high experimental and computational costs associated with this approach. A more practical macroscopic view has been developed based on Darcy's law, known as flow through a porous medium (Bear, 1976). The transition from a microscopic view to a macroscopic view is known as upscaling. This process can be performed based on either averaging techniques (Hassanizadeh and Gray, 1983a,b) or through a phenomenological approach by which macro-scale "laws" are stated directly and verified empirically (Bear, 2018). Newton's law of cooling, Fourier's law of heat conduction, and Fick's law of diffusion are examples of such macroscopic phenomenological laws (Bird et al., 2002). In hydrology, Darcy's law states that the fluid flow rate through the porous medium is proportional to the drop of fluid pressure or, expressed mathematically,

$$\boldsymbol{V} \propto -\boldsymbol{\nabla} p,$$

where $\boldsymbol{V}$ is superficial velocity, i.e. the flow rate across the total surface area, also known as specific discharge and p is liquid pressure. The flow typical in heaps is unsaturated as only a portion of pores

[2] If water contains solutes affecting its viscosity and density this number will change

are filled with water. Thus, the movement of both liquid and gas must be taken into account (in the context of heap leaching this was done by Cariaga et al., 2005). This is common practice, for example, in oil extraction models, where instead of air-water system water-oil phases are considered (Khlaifat, 2008). However, since there is no significant variation in air pressure in heaps when compared to the variation in capillary pressure, it can be assumed to be constant. As a result, only liquid movement is considered and it can be assumed that capillary pressure is equal to water pressure, $p_c = p_{\text{water}}$. This approach results in the Richards equation (Richards, 1931)[3].

3. The Richards equation. Mass balance in a porous medium is usually described via variation of water content within the bed:

$$\vartheta(\boldsymbol{x}) = \frac{\Delta\mathcal{V}_{\text{water}}}{\Delta\mathcal{V}},$$

where $\Delta\mathcal{V}$ is the volume around point $\boldsymbol{x}$ and $\Delta\mathcal{V}_{\text{water}}$ is the volume of (liquid) water within $\Delta\mathcal{V}$. $\Delta\mathcal{V}$ is chosen to be large enough to incorporate "enough" pores but still small compared to macroscopic scale and is known as the representative elemental volume (REV; Bear, 2018). Assuming negligible variation in water density, putting $p_c = p_{\text{water}} = g\rho h$, the mass balance results in the Richards equation (Richards, 1931):

$$\frac{\partial\vartheta}{\partial t} - \boldsymbol{\nabla}\cdot[\mathbf{K}\cdot(\boldsymbol{\nabla}h - \boldsymbol{e}_z)] = 0, \tag{I.1}$$

where $\mathbf{K}$ is the tensor of hydraulic conductivity, h is capillary pressure expressed in meters and $\boldsymbol{e}_z$ is a unit vector pointing in the direction of gravity. Capillary pressure h ranges from $-\infty$ for an extremely dry medium to 0 for the moment of full saturation and is positive if the flow becomes pressurised. The Richards equation describes the spread of a liquid in a porous medium due to gravity ($\boldsymbol{e}_z$ component) and differences in capillary pressure.

Note. As it was mentioned earlier, the Richards equation is a simplification of a more general mass balance equation in which air pressure is not constant. In this generalised form, equation (I.1) is

[3]This equation was actually first proposed by L.F. Richardson in 1922 (see Chapter 4 of Richardson, 2007).

replaced by two equations:

$$\frac{\partial \vartheta^l}{\partial t} - \boldsymbol{\nabla} \cdot \left[\mathbf{K}^l \cdot \boldsymbol{\nabla} h^l\right] = 0,$$
$$\frac{\partial \vartheta^a}{\partial t} - \boldsymbol{\nabla} \cdot \left[\mathbf{K}^a \cdot \boldsymbol{\nabla} h^a\right] = 0,$$

where superscripts l and a refer to liquid and air respectively. h^l in this case is a full liquid pressure, that includes the effect of gravity. Capillary pressure then is defined as $h = h^l - h^a$. This form of the model was used by Orr and Vesselinov (2002) and Cariaga et al. (2005). The problem of wetting front instability during infiltration can only be studied using this extended model (Bear, 2018).

4. Material properties: unsaturated model. Water content ϑ, hydraulic conductivity $\mathbf{K}$ and capillary pressure h are connected using empirical constitutive relations. While there is a wide range of such relations (Leij et al., 1997), currently the most widely used model is that of van Genuchten (van Genuchten, 1980) which is based on the Mualem theory (Mualem, 1976):

$$s(h) = \frac{\vartheta - \vartheta_r}{\vartheta_s - \vartheta_r} = \left(\frac{1}{1 + |\alpha h|^n}\right)^m, \tag{I.2}$$

$$\mathbf{K}(s) = \mathbf{K}_s K_r(s) = \mathbf{K}_s s^\ell \left(1 - \left[1 - s^{1/m}\right]^m\right)^2, \tag{I.3}$$

where $s \in [0, 1]$ is effective saturation (in this manuscript word "effective" will be dropped as no other saturation will be considered), ϑ_r and ϑ_s are residual and saturated water contents respectively, $\mathbf{K}_s$ is saturated hydraulic conductivity, function $K_r \colon s \to [0, 1]$ is referred to as relative conductivity, and α, ℓ, n and $m = 1 - 1/n$ are model parameters.

Saturated water content ϑ_s has a simple physical meaning: it is the maximum possible water content in the medium. It can be approximated by the medium porosity, but in general it is slightly less due to immovable air bubbles trapped inside the packing (Schaap et al., 2003). Residual water content ϑ_r is achieved when an infinitely large external air pressure is applied to a medium causing the air to displace most but not all the liquid inside the medium, or mathematically $h \to -\infty$ as $\vartheta \to \vartheta_r$. The problem with this definition is that it is practically impossible to establish ϑ_r directly. Instead, ϑ_r is found as an extrapolation of ϑ from measured values by taking $h \to -\infty$ (Schaap et al., 2003). Dixon and Afewu (2010) used drainage for over 4 days from a small sample to establish ϑ_r.

Hydraulic conductivity $\mathbf{K}(s) = \mathbf{K}_s K_r(s)$ represents three factors contributing to the flow in a porous medium:

1. The viscosity of the liquid. In a heap leaching context, where the solution is diluted, this parameter varies insignificantly unless surfactants are used. Liquid viscosity is a part of saturated conductivity $\mathbf{K}_s$.

2. The structure of the solid matrix and pores. Particle size distribution (PSD), the surface properties of the particles and how compactly these particles are packed define this factor. Their effect is also a part of saturated hydraulic conductivity $\mathbf{K}_s$ and is often grouped into porous medium permeability $\mathbf{k}$:

$$\mathbf{K}_s = \frac{\rho g}{\mu}\mathbf{k},$$

where ρ and μ are liquid density and dynamic viscosity respectively and g is acceleration due to gravity.

3. Solid-liquid-gas contact angle and the number of links connecting small pools of liquid established at different saturation levels is incorporated into relative conductivity $K_r(s)$.

The effect of PSD on permeability $\mathbf{k}$ has been modelled using the Carman-Kozeny equation (CK) by Sheikhzadeh et al. (2005), Trang et al. (2006) and Bao-hua et al. (2008). The CK model establishes the correlation between the isotropic permeability

$$\mathbf{k} = k\mathbf{I}, \quad \mathbf{I}\colon\ I_{ij} = \delta_{ij}$$

and effective particle size x, porosity ϕ and tortuosity τ. For example, the following form of the CK equation

$$k = \frac{\phi^2 x^2}{72\tau(1-\phi)^2}$$

was used by Trang et al. (2006), whereas Sheikhzadeh et al. (2005) used

$$k = \frac{x^2}{180}\frac{\phi^2}{1-\phi^2}.$$

Despite its convenience, the CK model has limited applicability since it was originally developed for mono-sized particles. The main issue is that the effect of PSD is defined by a single parameter x, whereas intuitively it should be dependent on the "spread" of the distribution. Furthermore, there is no single way of choosing x either, although it is common to choose the size of 10% weight passing, d_{10} (Sheikhzadeh et al., 2005).

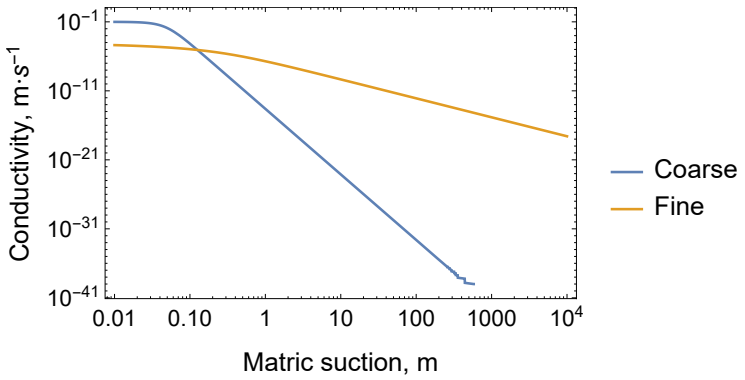

Figure I.2: Comparison of a hypothetical coarse and fine material hydraulic conductivity curve.

PSD has a further effect on relative conductivity $K_r(s)$. Following O'Kane Consultants Inc (2000), the effect of fine and coarse material can be illustrated by plotting the conductivity for each of the materials against matric suction h, i.e. $[K \circ s](h)$ from equations (I.2) and (I.3). Choosing, for example, $K_s = 0.1\,\mathrm{m}\cdot\mathrm{s}^{-1}$, $\alpha = 10\,\mathrm{m}^{-1}$ and $n = 2$ to represent the coarse material and $K_s = 10^{-4}\,\mathrm{m}\cdot\mathrm{s}^{-1}$, $\alpha = 2\,\mathrm{m}^{-1}$ and $n = 1.3$ to represent the fines, the corresponding curves are shown in Figure I.2. It is evident that a finer material at lower capillary pressure h may have higher hydraulic conductivity compared to a coarser material, but this trend reverses at the higher suction heads.

5. Boundary conditions (BC). For the top and side boundaries these conditions can be logically deduced: specified flow or no-flow, depending on the problem. There are, however, two possibilities at the bottom boundary. To enforce free drainage, no matric suction ($\boldsymbol{\nabla} h = 0$, equivalent to $\boldsymbol{\nabla} s = 0$) can be specified (Dixon and Afewu, 2010). However, the presence of the coarse drainage layer at the bottom of the pile results in the flow in this layer being driven primarily by gravity. Thus, matric suction there can be approximately put to zero. As a result, at the boundary between the main pile and the drainage layer matric suction can be assumed to be zero ($h_{\mathrm{bottom}} = 0$). It may seem like a small difference, however, the resulting phenomena are quite different:

- In the first case liquid is freely leaving the domain, whereas
- In the second case liquid will only leave the domain once gravity forces at the boundary overcome matric suction at the boundary layer. This potentially may lead to a higher saturation at the bottom of the pile.

The models that consider both liquid and air movement only specify a boundary condition for the air pressure, assuming it is equal to ambient pressure (Pantelis et al., 2002; Cariaga et al., 2005). In a simplified case of no air movement, this is equivalent to putting capillary pressure to zero at the bottom. However, there is no evidence that this BC was ever used in the context of heap leaching.

For completeness, it is worth mentioning work by Fala et al. (2005), which used small constant matric suction at the bottom of the dump pile to simulate the drainage. This condition, however, will not be appropriate for a heap that sits on an impermeable cover.

6. Solution of the Richards equation. Non-linearity of the Richards equation makes the task of solving it a challenge. While there exist some attempts at deriving analytical solutions (Tracy, 1995, 2007, 2011), they are not applicable for the conditions typical to heaps. Thus, the solution is usually approached numerically.

Finite differences (FD, Dixon and Afewu, 2010), finite volumes (FV, Eymard et al., 1999; Manzini and Ferraris, 2004; Lai and Ogden, 2015) and finite elements (FE, Molson et al., 2005; Cumming et al., 2011; Mostaghimi et al., 2013) are commonly used for spatial discretization. FD is attractive due to its simplicity when applied to a regular structured mesh on a rectangular or cubic domain or a domain that exhibits certain symmetries and can be mapped to a rectangle, such as an angular-symmetric cylinder (Smith, 1985). While FV requires a bit more work, such as transforming the equation into integral form, it offers a fundamentally mass-conservative scheme that is closer to a physical representation. Furthermore, it can applied to more general domain shapes using unstructured triangular or tetrahedral meshes (Moukalled et al., 2016). Lastly, application of FE (Galerkin method) requires a deeper understanding of the mathematics of partial differential equations (Reddy, 2007). In return, it offers a more flexible approach in obtaining a higher-order precision solution. In a one-dimensional case it was shown by Celia et al. (1990) that the straight forward application of FE (continuous Galerkin method) results in the development of unphysical oscillations. The issue was traced to the form of the mass matrix since in its exact form it is not simply diagonal in FE as compared to FD and FV (Celia et al., 1990). However, with a negligible second order error it can be approximated by the diagonal matrix eliminating the stability issues.

The Richards equation for low saturations is a parabolic type equation. Thus, despite non-linearities,

its solution is quite stable and does not allow the development of shock fronts[4]. A rapid change of relative conductivity K_r, however, may create numerical instabilities. Belfort et al. (2013) provided the analysis for choosing the approximation of K_r values on element boundaries for FV and FE methods. Alternatively, Kirchhoff's transformation can be used to transfer non-linearity from spatial derivative to time derivative (Haverkamp et al., 1977; Pop et al., 2004).

7. Extensions of the Richards equation. Macroscopic models are formulated for quantities, such as saturation and matric suction, that are averaged over a small volume (REV). The success of the averaging requires these quantities to vary approximately linear within the REV. This, however, may not be the case for the flow in heaps. For example, it was long-recognised that some liquid within the heaps behaves as if it is stagnant (the transport of the chemical compounds is primarily driven by the molecular diffusion) or at least slow moving, compared to the rest of the liquid (Bouffard and Dixon, 2001). Such a "bimodal" distribution of the fluid flow led researchers to formulate variants of the dual-porosity or dual-permeability models (Sheikhzadeh et al., 2005; Kartha and Srivastava, 2012; Robertson, 2017). McBride et al. (2017) offered a way to remove the liquid from the main matrix into preferential channels by introducing a source term into the Richards equation (I.1). However, the level of details presented in that article does not permit thorough examination of this extension.

8. Preferential flow. As it was stated earlier, formation of preferential flow channels during infiltration requires a comprehensive two-fluid model in which water displaces air (Orr and Vesselinov, 2002). The overall complexity of this kind of model, however, is prohibitive for heap hydrology investigation. Ilankoon and Neethling (2013, 2014) offered an alternative approach. The idea of their method is based on the assumption that the flow occurs only in rivulets. In rivulets some liquid stays stagnant and some flows. An original model was developed for non-porous spherical glass beads under extremely high flow rate. Later it was extended to include porous mono-sized ore. However, due to the way the model is formulated it requires non-trivial extension to include the effects of fines on the flow. Moreover, the model was only tested with high flow rates, that can only be found in close proximity to drip emitters in a heap leaching context.

[4]This not to be confused with oscillations that may occur as a result of a crude discretisation (for more details see Celia et al., 1990).

The theory of liquid flow does not fully capture the transport of solutes. Due to the macro-scale view, micro-scale details of the flow are omitted, such as liquid velocity variation in the flow through a pore and back-mixing effects due to mixing of liquid elements that took different paths through the solid matrix. In terms of leaching performance it is solute transport that it is of primary concern. Accordingly, its theory is reviewed next.

§ 4. Theory of solute transport

1. Advection-dispersion equation. Dissolved chemical compounds are transported in the liquid phase by a number of mechanisms: convection with the bulk fluid flow, mechanical dispersion due to different paths and velocities taken by different fluid "particles" and molecular diffusion. Solution of the Richards equation (I.1) provides the velocity field $\boldsymbol{V}$ for the convective transport. Since the field $\boldsymbol{V}$ is an average macroscopic velocity, local variations within it are modelled via a dispersion coefficient $\mathbf{D}$. Finally, the sources and sinks of the compounds due to chemical reactions are modelled using the source term S. Overall, the advection-dispersion equation for a dilute concentration c_j has the form:

$$\frac{\partial\left(\vartheta c_j\right)}{\partial t} + \boldsymbol{\nabla}\cdot\left(\vartheta \boldsymbol{V} c_j\right) - \mathbf{D}_j\cdot\left(\boldsymbol{\nabla} c_j\right) = S_j. \tag{I.4}$$

This equation is formulated for every dissolved compound j. If there is a chemical reaction involving multiple dissolved compounds, the corresponding advection-dispersion equations are coupled via source terms and need to be solved simultaneously. Since all the compounds j in equation (I.4) have a dilute concentration c_j it implies that a change in their concentration would not affect liquid transport, and thus the Richards equation (I.1) can be decoupled from advection-dispersion equations (I.4). It is worth pointing out, however, that there may be systems where this decoupling is not possible. For example, if the compound can significantly affect water surface tension or viscosity even at small concentrations, e.g. a surfactant.

2. On the dispersion coefficient. The dispersion coefficient $\mathbf{D}$ is usually assumed to be proportional to the absolute value of the specific discharge $|\boldsymbol{V}|$ (Cariaga et al., 2005). Due to a similarity in mechanisms, molecular diffusion is often included as a part of the dispersion tensor $\mathbf{D}$ (Dixon and Afewu, 2010). To reflect the fact that the extent of dispersion is different in different directions with

maximum reaching in the direction of the flow $\boldsymbol{V}$, the tensor $\mathbf{D}$ has three main components (in a three-dimensional domain): longitudinal

$$D_L = \alpha_L |\boldsymbol{V}| + \varepsilon_{\mathscr{D}} \mathscr{D}$$

and two equal transversal

$$D_T = \alpha_T |\boldsymbol{V}| + \varepsilon_{\mathscr{D}} \mathscr{D},$$

where α_i, $i = L, T$ are longitudinal and transversal dispersivity coefficients, $\varepsilon_{\mathscr{D}}$ is a coefficient that depends on water content and $\mathscr{D}$ is molecular diffusion. If the effect of diffusion can be neglected, $\varepsilon_{\mathscr{D}} \equiv 0$. Thus, in the coordinate system parallel to $\boldsymbol{V}$ dispersion has a form $\mathbf{D} = \operatorname{diag}\{D_L, D_T, D_T\}$, where operator "diag" constructs a diagonal matrix from the provided vector. In an arbitrary orthonormal basis components D_{ij} of the tensor $\mathbf{D}$ have the following form:

$$D_{ij} = \alpha_T |\boldsymbol{V}| \delta_{ij} + (\alpha_L - \alpha_T) \frac{V_i V_j}{|\boldsymbol{V}|} + \varepsilon_{\mathscr{D}} \mathscr{D} \delta_{ij},$$

where δ_{ij} is Kronecker's delta (Cariaga et al., 2005). Coefficients α_i are usually assumed constants. However, there is field data indicating that they depend on the scale of the experiment (Dixon and Afewu, 2010).

3. Advection-diffusion models. If dispersion effects are ignored, i.e. if they are insignificant compared to diffusion, dispersion coefficients D_{ij} can be approximated by diffusion, $D_{ij} \approx \varepsilon_{\mathscr{D}} \mathscr{D} \delta_{ij}$. This indeed is the case when the absolute value of the specific discharge $|\boldsymbol{V}|$ is small. If, for example, the liquid is split into mobile and stagnant, dispersion can be reduced to diffusion in the stagnant part of the liquid. Furthermore, intrinsic flow rate of the mobile liquid becomes high if a significant portion of the liquid is stagnant. Thus, in the mobile liquid dispersion and diffusion effects become insignificant compared to advective flow. As a result, the advection-dispersion equation (I.4) can be replaced by two equations for mobile and immobile solutions respectively (Ogbonna et al., 2005):

$$\begin{aligned} \frac{\partial c_{j,f}}{\partial t} + v \frac{\partial c_{j,f}}{\partial z} &= S_{j,fs} + S_{j,s}, \\ \frac{\partial c_{j,s}}{\partial t} &= \varepsilon_{\mathscr{D}} \mathscr{D} \nabla_x^2 c_{j,s} + S_{j,sf} + S_{j,s}, \end{aligned}$$

where a two-dimensional domain is assumed with the flow in a z-direction, with advective velocity v, and with the diffusion in an x-direction. Symbol ∇_x denotes a derivative in the x-direction that takes

into account that the coordinate line might not be Cartesian. For example, for a spherically symmetrical system with the axis x in the direction of radius, the second derivative becomes

$$\nabla_x^2 c = \frac{\partial^2 c}{\partial x^2} + \frac{2}{r}\frac{\partial c}{\partial r}.$$

Source terms $S_{j,fs}$ and $S_{j,sf}$ describe the mass exchange between flowing and stagnant solutions in units conforming to their respective equations, i.e. $S_{j,fs} = S_{j,sf}$ provided they are expressed in the correct units.

One important assumption of advection-diffusion models is the split of the liquid into flowing and stagnant. At the moment there is no way to predict such a split from fundamental principles and it is usually established directly from experiments. This approach, however, cannot be reliably scaled as the portion of stagnant solution may depend on the size of the packing and even on the method of packing (Bouffard and West-Sells, 2009).

4. Compartment models are simplified models that are used in chemical engineering as a diagnostic tool (Levenspiel, 1999). The idea of the method is to model non-ideal flow (ideal flow being either fully mixed or purely plug-flow) as a combination of ideal-flow reactors. The main advantage of this method is the simplicity of the flow description. However, this advantage comes with a price. In general it is not possible to extend the findings of this method from one reactor to another. Neither is it possible to predict the change in the flow pattern with a change of the flow rate. A compartment model combining a plug-flow reactor, a continuous stirred tank reactor (CSTR), dead volume and short-circuit flow was used by Bouffard and West-Sells (2009) to investigate the effect of the experimental scale on the flow patterns in packed rock beds. A larger scale of the experiment was found to correlate with the amount of the stagnant solution. Properties of the individual compartment models and their combinations are further examined in section § 8 on page 56 of Chapter II.

The theory underlying transport phenomena in packed rock beds is complex with many non-linear material relations. These relations introduce many parameters that must to be known *a priori* to apply the theory. Many of these parameters cannot be measured directly. Instead, their values need to be deduced by fitting model results to experimental data (Schaap et al., 2003). This results in a two-stage process of matching the theory and empirical data: model calibration to identify parameter values and model validation to verify model results. The next section examines the available empirical evidence supporting or opposing the theory.

§ 5. Experimental data

1. Model calibration. One of the aspects of developing a model is to do "inverse" modelling: finding unknown parameters for an experimentally known result (Schaap et al., 2003; Bear, 2018). This process is also known as model calibration. When applied to the Richards equation, hydraulic parameters, such as K_s, ℓ, α, n and m of the van Genuchten model (see equations (I.1)–(I.3)) are unknown *a priori*. In the field of soil hydrology a large body of research is dedicated to estimating these parameters from soil properties. Pedotransfer functions aim to empirically predict them from, for example, soil particle size distribution (Arya et al., 1999; Mbonimpa et al., 2002). Their precision, however, is rather poor. The ROSETTA program uses a neural-network approach to classify soil samples and uses hierarchical pedotransfer functions to estimate hydraulic parameters and uncertainties associated with them (Schaap et al., 1998, 2001). While such techniques exist for soils, there is no available method to infer hydraulic parameters for ores.

In the open literature, there are very few published studies that provide details on finding hydraulic parameter values from experimental data. Sheikhzadeh et al. (2005) conducted intermittent flow experiments with columns packed with ore and monitored the outflow to infer the parameters. Dixon and Afewu (2010) did a comprehensive study at multiple scales with fully instrumented columns to monitor matric suction and water content *in situ*. Table I.1 shows the values of some hydraulic parameters reported in these and a few other studies. Available data does not permit any inference of a correlation between ore properties and hydraulic parameters, with the exception of a general tendency for permeability k to decrease with decreasing effective particle size.

2. Model validation. Model calibration is only a fitting exercise. Considering the complexity of the Richards equation, it is conceivable that it can fit a wide range of data. However, the real value of the model comes from the ability to predict the effects once applied to a different set of data. Model validation does exactly this: it compares model outcomes applied to a dataset with experimental results. The key is that this dataset must be different from data used for calibration. This is akin to hypothesis testing. In the context of heap hydrology, validation requires model application to data from a larger experimental scale or different flow rate. Sadly, this step is often missing. In published research (in the context of heap leaching), it is only the work by Dixon and Afewu (2010) that shows a comprehensive validation of the Richards equation-based model. Therefore, it is prudent to treat the

Table I.1: Comparison of hydraulic parameters (van Genuchten model) reported for different ores. The value of van Genuchten parameter m for Mantoverde ore was fitted independently of n, instead of using $m = 1 - 1/n$.

Ore origin	α, m^{-1}	d_{10}, mm	n, -	k, m^2	Reference
Tranque Barahona	1.3	–	1.306	2×10^{-12}	Cariaga et al. (2015)
Unkown	12	–	1.62	–	Guzman et al. (2002)
Sarcheshmeh	3	0.2	1.39	1.0×10^{-9}	Sheikhzadeh et al. (2005)
Doyon (dump)	494	2	1.30	1.0×10^{-9}–2.5×10^{-9}	Lefebvre et al. (2001)
Nordhalde (dump)	3.53	0.02	1.34	8×10^{-12}–8×10^{-11}	Lefebvre et al. (2001)
Carlin	4.78	–	3.25	1.2033×10^{-12}	Kartha and Srivastava (2012)
Mantoverde	20	0.01	7.137 (m = 0.4213)	1.6×10^{-8}	Dixon and Afewu (2010)
Dexing	–	0.4	–	3.44×10^{-10}–2.25×10^{-8}	Bao-hua et al. (2008)

Richards equation as an untested hypothesis when it is applied to heap leaching at this point in time.

3. Experimental studies on preferential flow. The formation of preferential flow channels in field-scale experiments of an ore dump was observed by Nichol et al. (2005). It was concluded that preferential channels are rare, but have a considerable effect on the flow. O'Kane Consultants Inc (2000) and Wu et al. (2007) performed a study on the preferential flow in packed rock beds and noted that under unsaturated conditions most of the flow occurs through the finer part of the packing. Fagan et al. (2014) observed the formation of preferential flow right underneath the drip emitter with only a marginal part of the liquid flowing laterally. Van Staden and Petersen (2019) studied the effect of the stratified packing on the formation of the preferential flow and its subsequent effect on leaching. It was found that the stratified packing results in a wider spread of the flow (without any particular pattern), but has a marginal effect on leaching. With the exception of the work by Nichol et al. (2005) where an array of lysimeters was used, other studies on preferential flow used a grid of collection ports at the bottom of the ore bed. This, however, does not provide a direct observation of preferential flow but only shows its effect.

4. Direct flow observations: tomography techniques are becoming more widely used to provide direct observations of the flow phenomena in packed rock beds. Rucker et al. (2009) used electrical

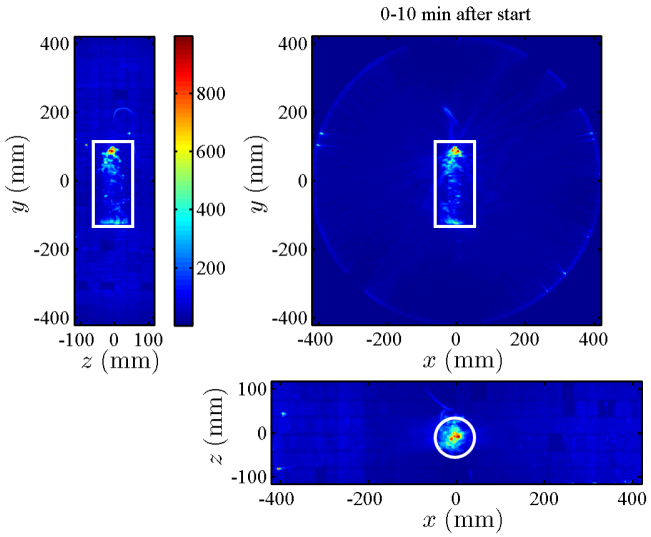

Figure I.3: PET image of the solution flow though a small column packed with ore obtained during preliminary studies by the author (published in Petersen, 2015). The white frame indicates the boundary of the column.

resistivity tomography (ERT) to measure saturation in heaps. Fagan et al. (2013) studied the liquid distribution in small size beds using magnetic resonance imaging (MRI). Ilankoon et al. (2013) used positron emission particle tracking (PEPT) to study liquid pathways in packed beds. Finally, positron emission tomography (PET) can show the areas in the packing directly accessible to moving liquid (Petersen, 2015).

Although some flow effects were observed using these techniques, such as saturation variation within the heap (Rucker et al., 2009) or the formation of small pools of moving liquid (Petersen, 2015), at present the main focus is on improving these techniques. For example, all three ERT, MRI and PET only offer low resolution images (Figure I.3). Furthermore, MRI, PEPT and PET only work with beds of small sizes. PEPT, in addition to this, is limited to tracking a small number of particles, which may not explore all the possible paths that liquid can take. Overall, although tomography techniques offer direct view on the flow, their correct application is coupled with numerous and still unresolved technical difficulties. As a result, currently their application to the study of the flow through packed rock beds is limited.

§ 6. Problem statement

To summarise, at present there is a lack of understanding of solution transport in packed rock beds, such as used in heap leaching, despite considerable advances in hydrology theory and application related to soils. Compared to soils, packed rock beds have coarser particle size distribution and, as a result, larger pore sizes. As a result, their wetting and drying patterns are different compared to agricultural soils. The kind of questions that are asked about the transport process are also different.

Due to the lack of systematic experimental data for hydrodynamics of packed rock beds, the research field is wide open. This thesis aims to lay a piece of the foundation for future research and to help state the questions that are relevant for applications. There are two main goals:

1. Examine the applicability of the solution transport models with different simplifications to a typical heap leaching scenario. In particular, examine how sensitive these models are to various parameters and establish what effects can be observable with models of various complexity.

2. Establish useful correlations that can relate intrinsic, easily measurable properties of the ore (e.g. PSD), operation conditions (inlet flow rate), and hydraulic properties and hydrodynamic response.

The following effects are deliberately excluded form this study:

- The effect of clay in ores is not considered. Clay response to wetting and drying is quite complicated due to water absorption and swelling and requires a separate study of its own. To exclude this effect, a material with low clay content was chosen for experimental studies.

- The effect of different mineralogy is also not considered. All the experiments are conducted on the ore of a single type. Some of the results, however, are compared with the literature results obtained on different ores.

- The effect of scale is not studied. All the experiments are conducted at a single scale. Similarly to effect of clay, the extension of the results of this study to different scales requires a separate study.

The next chapter examines solution transport and solute transfer models deriving some important properties that would provide the motivation for the experimental work described in Chapter III. Model results will be compared with experimental data in Chapter IV.

Chapter II

Hydraulic models for heap leaching

Entire fields of knowledge, such as physics and engineering, have already lost almost all touch with the spoken human language, and maintained solely by mathematical script.

— Yuval Noah Harari, Sapiens

§ 1. The Richards equation model in 2D: problem statement

This section is a starting point for various techniques to find the solution of the Richards equation. Due to the computational complexity of solving a full 3D model, a simplified two-dimensional model is formulated, as this is a common practice in literature (Cariaga et al., 2005; McBride et al., 2017).

1. Domain $\Omega = (0, W) \times (0, H) \subset \mathbb{R}^2$ is a rectangle with the first coordinate $x \in (0, W)$ directed horizontally and the second coordinate $z \in (0, H)$ directed vertically downwards. By "vertical" and "downwards" we mean that this direction coincides with the direction of gravity. The origin is located at the upper left corner. Coordinate x represents a horizontal direction in a Cartesian coordinate system Oxz. It also can represent a radial direction in cylindrical coordinates Orz. Furthermore, while the domain Ω in coordinates Oxz is a rectangle, potentially any two-dimensional domain can be mapped into these coordinates. For example, let domain Ω' be any two-dimensional simply connected closed area and $O\xi\zeta$ be Cartesian coordinates on the plane. If Oxz are chosen to be local curved coordinates

of Ω' with

$$\xi = \xi(x, z),$$
$$\zeta = \zeta(x, z)$$

and a non-singular Jacobian

$$\begin{pmatrix} \frac{\partial \xi}{\partial x} & \frac{\partial \xi}{\partial z} \\ \frac{\partial \zeta}{\partial x} & \frac{\partial \zeta}{\partial z} \end{pmatrix},$$

this transformation will map Ω' to a rectangle Ω. Figure II.1 visually demonstrates this transformation. The domain boundaries are assigned the following meanings:

- The top boundary $\partial\Omega_{\text{top}} = \{(x, 0), x \in (0, W)\}$ is the boundary of the inlet flow application.
- The bottom boundary $\partial\Omega_{\text{bottom}} = \{(x, H), x \in (0, W)\}$ is the boundary of the solution drainage.
- No special meaning is assigned to the sides

  $$\partial\Omega_{\text{left}} = \{(0, z), z \in (0, H)\} \quad \text{and} \quad \partial\Omega_{\text{right}} = \{(W, z), z \in (0, H)\},$$

  but it will be assumed that no flow occurs through these boundaries.

2. The Richards equation (I.1) written in terms of effective saturation s for an isotropic medium and in Cartesian coordinates Oxz is as follows:

$$\Delta\vartheta \frac{\partial s}{\partial t} - \frac{\partial}{\partial x}\left[K(s)\frac{\partial h(s)}{\partial x}\right] - \frac{\partial}{\partial z}\left[K(s)\left(\frac{\partial h(s)}{\partial z} - 1\right)\right] = 0, \tag{II.1}$$

where $\Delta\vartheta = \vartheta_s - \vartheta_r$ is the total water content variance. Note, this equation is only valid in the unsaturated region $s < 1$. A one-dimensional form can be obtained by dropping the derivative in the x-direction:

$$\Delta\vartheta \frac{\partial s}{\partial t} - \frac{\partial}{\partial z}\left[K(s)\left(\frac{\partial h(s)}{\partial z} - 1\right)\right] = 0. \tag{II.2}$$

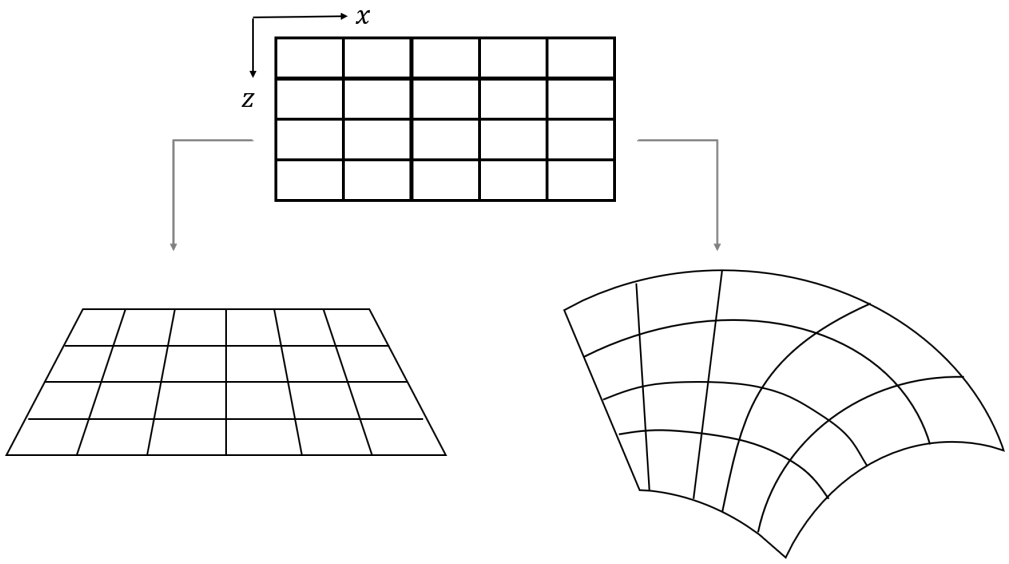

Figure II.1: Rectangular 2D domain can be mapped to trapezoid or even curve-shaped domain by the coordinate transformation.

3. Boundary conditions, representing the known irrigation flow rate at the top, free flow out of the domain at the bottom (the flow driven by gravity only), and no flow through side boundaries, are:

$$V_z|_{\partial\Omega_{\text{top}}} = -K(s)\left(\frac{\partial h(s)}{\partial z} - 1\right)\Big|_{\partial\Omega_{\text{top}}} = q_{\text{in}}, \tag{II.3}$$

$$\frac{\partial h(s)}{\partial z}\Big|_{\partial\Omega_{\text{bottom}}} = 0, \tag{II.4}$$

$$\frac{\partial h(s)}{\partial x}\Big|_{\partial\Omega_{\text{left}}} = \frac{\partial h(s)}{\partial x}\Big|_{\partial\Omega_{\text{right}}} = 0. \tag{II.5}$$

For one-dimensional equation (II.2), the last two conditions (II.5) are omitted.

4. Initial saturation is specified as a function of coordinates x and z

$$s(0, x, z) = s^*(x, z) \tag{II.6}$$

or of just coordinate z in case of a one-dimensional problem.

5. Effects that are investigated. The purpose of this chapter is to examine what effects the Richards equation model predicts and under what conditions (relevant to the heap leaching context of course). The following effects are examined:

Packing non-uniformity. What saturation and what kind of flow will be achieved? What differences are there between two-dimensional and one-dimensional flows with non-uniform hydraulic parameters? How stable is the saturation distribution to perturbations of the hydraulic parameters?

Effects of irrigation. What changes in the flow pattern can be observed depending on the inlet flow irrigation rate? What are the effects of irregular inlet flow? How much difference is there between distributed and concentrated inlet flows, i.e. the difference between sprinklers and single drop emitters?

Due to the non-linearity of the Richards equation (II.1) and non-trivial boundary conditions, the only feasible way to solve this equation is to use a numerical approximation. However, it is worth examining a simplified form of this equation to understand the behaviour of the solution. The following sections deal with two kinds of simplifications — one approach assumes steady-state, while the second looks at a transient model with uniform distribution of the water content. Sections §5 and §6 show numerical solutions to 1D and 2D problems respectively.

§ 2. Two-dimensional steady-state Richards' equation

A steady-state condition is achieved when the all the flow functions, such as $s(t, x, z)$, $h(t, x, z)$, and $\boldsymbol{V}(t, x, z)$, become independent of time. First, there is the question of the existence of the steady-state and if it indeed can be achieved. If it does exist, it still must satisfy the Richards equation (II.1) but with $\partial s/\partial t \equiv 0$:

$$\frac{\partial}{\partial x}\left[K(h)\frac{\partial h}{\partial x}\right] + \frac{\partial}{\partial z}\left[K(h)\left(\frac{\partial h}{\partial z} - 1\right)\right] = 0. \tag{II.7}$$

It is convenient to formulate this equation in terms of capillary pressure alone, so here $K(h) = K\left[h(s)\right]$. The common way to solve such an equation is to assume some form of $K(h)$ and try to find the solution. However, general complexity of hydraulic models would only leave the numerical route for solution. There is an opposite way: assuming some solution form $h(x, z)$ and finding the corresponding form of $K(h)$.

Let's find the forms of hydraulic conductivity $K(h)$ that would support constant capillary pressure throughout the domain, $h = h_0 \equiv \text{const}$. It is obvious the only boundary condition that can satisfy this solution is uniform pressure distribution at the top boundary. This, however, does not mean uniform

inlet flow rate as will be illustrated below. Secondly, constant pressure results in partial derivatives to be equal to zero. Thus, equation (II.7) simplifies to

$$-\frac{\partial K}{\partial z} = 0.$$

If hydraulic parameters are not uniform throughout the domain, the correct way to express this is to write $K = K(h, x, z)$. Since capillary pressure is constant,

$$\frac{\partial K}{\partial z} = \left(\frac{\partial K}{\partial h}\right)_{x,z} \frac{\partial h}{\partial z} + \left(\frac{\partial K}{\partial z}\right)_{h,x} = \left(\frac{\partial K}{\partial z}\right)_{h,x}.$$

Therefore, K must be independent of z. This proves the following:

Theorem 1. *If $h(x, z) = h_0 \equiv$ const is the solution of the steady-state equation (II.7) satisfying boundary conditions (II.3)–(II.5), hydraulic (material) parameters either must be uniformly distributed or may only vary in lateral direction x. The steady-state flow under constant capillary pressure is directed strictly downwards.*

Let's assume uniform hydraulic parameters distribution but possibly non-uniform inlet flow distribution at the top. In this case the solution of equation (II.7) is some function $h(x, z)$. Let point $M = (x_0, z_0) \in \Omega$ and consider the variation of $h(x, z)$ around this point. In the close vicinity of M

$$h(x, z) \approx h_M + \left.\frac{\partial h}{\partial x}\right|_M (x - x_0) + \left.\frac{\partial h}{\partial z}\right|_M (z - z_0) = h_M + A\Delta x + B\Delta z$$

and

$$K(h) \approx K_M + \left.\frac{\partial K}{\partial h}\right|_M \left.\frac{\partial h}{\partial x}\right|_M \Delta x + \left.\frac{\partial K}{\partial h}\right|_M \left.\frac{\partial h}{\partial z}\right|_M \Delta z = K_M + \varkappa \left(A\Delta x + B\Delta z\right),$$

where $\varkappa = \partial K/\partial h(M)$. Substitution of these approximations into equation (II.7) results in

$$\frac{\partial}{\partial x}\left[\{K_M + \varkappa(A\Delta x + B\Delta z\}\, A\right] + \frac{\partial}{\partial z}\left[\{K_M + \varkappa(A\Delta x + B\Delta z\}\, (B - 1)\right] = 0.$$

Since K_M, A, B and $\varkappa$ are constants, it simplifies to

$$\varkappa\left(A^2 + B^2 - B\right) = 0.$$

Physically, $\varkappa = \partial K/\partial h$ is strictly positive in an unsaturated region, since conductivity grows with the growth of capillary pressure. It follows that

$$A^2 + B^2 - B = A^2 + \left(B - \frac{1}{2}\right)^2 - \left(\frac{1}{2}\right)^2 = 0.$$

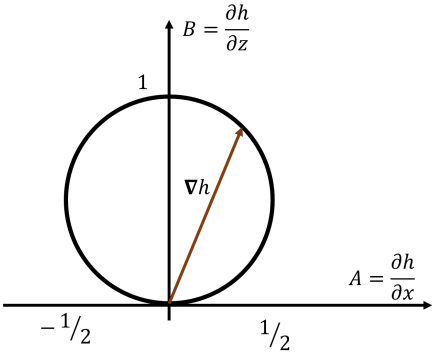

Figure II.2: Graphical representation of the constraint on the capillary pressure gradient for the steady-state problem II.7.

This is the restriction on the gradient of the capillary pressure in each point of the domain. In the AB-plane, this equation is a circle with a radius of $1/2$ and a centre at $(0, 1/2)$. $A = \partial h/\partial x$ varies between $-1/2$ and $1/2$ (see Figure II.2). $B = \partial h/\partial z$ varies between 0 and 1. Since $B_{\max} = (\partial h/\partial z)_{\max} = 1$, it follows that

$$\frac{\partial h}{\partial z} - 1 \leq 0.$$

This means that the z-component of the specific discharge $V_z = -K(\partial h/\partial z - 1) \geq 0$. This conclusion can be formulated as the following two theorems:

Theorem 2. *If hydraulic parameters are distributed uniformly, steady-state flow governed by equation (II.7) cannot be directed upwards.*

Theorem 3. *At steady-state conditions the flow according to the Richards equation (II.7) is governed either by the gravity alone or by both gravity and the capillary pressure.*

Proof. The vertical component of the specific discharge is

$$V_z = -K\left(\frac{\partial h}{\partial z} - 1\right),$$

where "-1" denotes the pull due to gravity. Since $|\partial h/\partial z| \leq |\boldsymbol{\nabla} h| \leq 1$ (Figure II.2), the magnitude of the specific discharge is either dominated by gravity or by the combination of gravity and capillary pressure. □

The results from analytical examination of the two-dimensional Richards equation only allow qualitative judgement of the flow due to the complexity of the hydraulic model. More information can be extracted if the model is restricted to one dimension.

§ 3. The steady-state uniform model (SSUM)

1. Solution. The steady-state Richards equation (II.7) can be re-written in the following form

$$\boldsymbol{\nabla} \cdot \boldsymbol{V} = 0,$$

where (in two-dimensional domain Ω)

$$\boldsymbol{V} = -K(h)\left(\frac{\partial h}{\partial x}\boldsymbol{e}_x + \left(\frac{\partial h}{\partial z} - 1\right)\boldsymbol{e}_z\right)$$

is specific discharge. If variation in the x-direction can be neglected, it simplifies to

$$\frac{\mathrm{d}V}{\mathrm{d}z} = 0, \qquad V = -K(h)\left(\frac{\mathrm{d}h}{\mathrm{d}z} - 1\right).$$

Therefore, at steady-state the mass conservation principle dictates that

$$V(z) = -K\left(h(z)\right)\left[\frac{\mathrm{d}h}{\mathrm{d}z} - 1\right] = V(0) = q_{\text{in}} \equiv \text{const}, \tag{II.8}$$

Rewriting this equation in terms of capillary pressure h, results in the following equation:

$$\frac{\mathrm{d}h}{\mathrm{d}z} = 1 - \frac{q_{\text{in}}}{K(h)} \tag{II.9}$$

or, written in terms of saturation,

$$\frac{\mathrm{d}s}{\mathrm{d}z} = \frac{1}{h'(s)}\left(1 - \frac{q_{\text{in}}}{K(s)}\right) \tag{II.10}$$

with $h'(s) = \mathrm{d}h/\mathrm{d}s$. The boundary value for this equation is obtained by considering equation (II.8) near the bottom, $z = H$. As $z \to H$, according to the free surface BC (II.4), $dh/dz \to 0$ (assuming the continuity of the derivative). This results in the following condition at the bottom:

$$V(H) = K\left(h(H)\right) = q_{\text{in}}, \tag{II.11}$$

Therefore, $h(H)$ (or $s(H)$ since $s = s(h)$) is obtained as the solution of this algebraic equation. If the packing is uniform, i.e. if $K(h)$ does not explicitly depend on z, it is easy to show by direct substitution that $h(z) = \text{const} = h(H)$ is the solution. And, thus, saturation is also uniform,

$$s(z) = s\left(h(z)\right) = s\left(h(H)\right). \tag{II.12}$$

Algorithm 1 Bisection algorithm used to solve (II.11).

```
Function FindSaturation(Ks As Double, l As Double, _
        m As Double, qin As Double) As Double
    Dim a As Double, b As Double, fa As Double, fb As Double
    Dim c As Double, fc As Double
    Dim eps As Double

    eps = 0.0000001
    a = 0.001
    b = 0.999
    fa = Cond(Ks, l, m, a) - qin
    fb = Cond(Ks, l, m, b) - qin

    Do While Abs(a - b) >= eps
        c = (a + b) / 2
        fc = Cond(Ks, l, m, c) - qin
        If fa * fc <= 0 Then
            b = c
            fb = fc
        End If

        If fc * fb <= 0 Then
            a = c
            fa = fc
        End If
    Loop
    FindSaturation = (a + b) / 2
End Function
```

The above procedure also provides a simple meaning to the unsaturated conductivity $K(s)$: it is the flow rate (specific discharge) that will be achieved at steady-state at a particular saturation s if capillary pull is neglected. Although this conclusion is hardly new (see, for example, Philip, 1957b), it is never emphasised.

SSUM is implemented as a simple Visual Basic macro-function `FindSaturation` in a MS Excel spreadsheet. The function receives hydraulic parameters and inlet flow rate as inputs and produces saturation as a result of the solution of the equation $K(s) = q_{\text{in}}$. Solution is obtained by a simple bisection method starting from $[0.001, 0.999]$ bounds of saturation (Algorithm 1).

2. Stability of the steady-state solution. Solution dependence on model parameters. Applicability of the solution (II.12) of the steady-state problem (II.9) and (II.11) relies on the stability of this solution since in practice some perturbations in hydraulic parameters are unavoidable. To be more concrete, consider the widely used van Genuchten unsaturated model (I.2) and (I.3), restated here for convenience (van Genuchten, 1980)[1]:

$$K(s) = K_s K_r(s) = K_s s^{\ell} \left(1 - \left[1 - s^{1/m}\right]^m\right)^2, \tag{II.13}$$

$$s(h) = \left(\frac{1}{1 + |\alpha h|^n}\right)^m, \tag{II.14}$$

where K_s $[\mathrm{m} \cdot \mathrm{s}^{-1}]$ is the saturated conductivity, parameter ℓ is commonly assumed to be $1/2$, n and $m = 1 - 1/n$ are fitting model parameters, but can also be regarded as a measure of pore-size distribution (Brooks and Corey, 1964; van Genuchten, 1980), and α $[\mathrm{m}^{-1}]$ is the reciprocal of the bubbling pressure: the maximum capillary pressure at which the air movement is still possible (Brooks and Corey, 1964). Solution (II.12) depends on the parameters $\{\ell, n, \alpha, q_{\text{in}}, K_s\}$. The number of parameters can be reduced if equation (II.11) is re-written in terms of saturation and a fraction of the flooding flow rate is introduced $\Bbbk = q_{\text{in}}/K_s$:

$$K_r(s) = \Bbbk \tag{II.15}$$

with $s \equiv \text{const}$ and $h(s) \equiv \text{const}$ being the solution of equation (II.9). In these terms, two questions arise:

Question 1. *How will the solution s of equation (II.15) change with the change of parameters $\{\ell, n, \Bbbk\}$? I.e., how sensitive is the saturation towards hydraulic parameters?*

Question 2. *How stable is the solution of the differential equation (II.9) to perturbations of parameters $\{\ell, n, \Bbbk, \alpha\}$?*

The first question requires investigation of the sensitivity of the solution of the algebraic equation (II.15) towards parameters $\{\ell, n, \Bbbk\}$. From a practical perspective we need relative sensitivity, e.g. we want to be able to answer by how many percentage points the saturation will change if say, parameter n is changed by 10%. The following proposition provides a mathematical framework for relative sensitivities:

[1] Van Genuchten model is used in this study as opposed to another widely used Brooks-Corey model (Dixon and Afewu, 2010) since: (a) it was shown that both models are effectively equivalent (van Genuchten, 1980; Lenhard et al., 1989) and (b) Brooks-Corey model was shown to be less stable when hydraulic parameters are inferred from the solution of the Richards equation (Schaap et al., 2003).

Proposition 1. *Relative perturbance multiplier matrix* $\mathbf{\Gamma} \in \mathrm{Mat}\,(k \times m)$ *for the function* $\boldsymbol{g}\,(\boldsymbol{\xi};\boldsymbol{\eta})$*:*

$$\boldsymbol{g}\colon \mathbb{R}^n \times \mathbb{R}^m \to \mathbb{R}^k$$

of the solution $\boldsymbol{\xi} \in \mathbb{R}^n$ *for parameters* $\boldsymbol{\eta} \in \mathbb{R}^k$ *of the algebraic equation* $\boldsymbol{f}\,(\boldsymbol{x};\boldsymbol{p}) = 0$ *with*

$$\boldsymbol{f}\colon \mathbb{R}^n \times \mathbb{R}^m \to \mathbb{R}^n$$

has the form

$$\mathbf{\Gamma} = \left[\left(\frac{\partial \boldsymbol{g}}{\partial \boldsymbol{p}}\right)_{\boldsymbol{x}}(\boldsymbol{\xi};\boldsymbol{\eta}) - \mathbf{\Lambda}^T \cdot \left(\frac{\partial \boldsymbol{f}}{\partial \boldsymbol{p}}\right)_{\boldsymbol{p}}(\boldsymbol{\xi};\boldsymbol{\eta})\right] \overset{c}{\oslash}\, \boldsymbol{g}\,(\boldsymbol{\xi};\boldsymbol{\eta}) \overset{r}{\odot} |\boldsymbol{\eta}|^T, \tag{II.16}$$

where matrix $\mathbf{\Lambda}$ *is the solution of the following set of linear equations:*

$$\left[\left(\frac{\partial \boldsymbol{f}}{\partial \boldsymbol{x}}\right)_{\boldsymbol{p}}(\boldsymbol{\xi};\boldsymbol{\eta})\right]^T \cdot \mathbf{\Lambda} = \left[\left(\frac{\partial \boldsymbol{g}}{\partial \boldsymbol{x}}\right)_{\boldsymbol{p}}(\boldsymbol{\xi};\boldsymbol{\eta})\right]^T \tag{II.17}$$

and symbols $\overset{c}{\oslash}$ *and* $\overset{r}{\odot}$ *denote column-wise division and row-wise multiplication respectively.*

Each entry Γ_{ij} *of the matrix* $\mathbf{\Gamma}$ *has the following meaning: it shows by how much* i*-th component of* $\boldsymbol{g}\,(\boldsymbol{\xi};\boldsymbol{\eta})$ *will vary relative to the variance of* j*-th component of the parameter vector* $\boldsymbol{\eta}$*.*

Proof. The proof begins with the application of the standard sensitivity analysis. If $\boldsymbol{x} = \boldsymbol{\xi}$ and $\boldsymbol{x} = \boldsymbol{\xi}'$ are the solution of $\boldsymbol{f}\,(\boldsymbol{x};\boldsymbol{p}) = 0$ with parameters $\boldsymbol{p} = \boldsymbol{\eta}$ and $\boldsymbol{p} = \boldsymbol{\eta}'$ respectively, considering the solution as a function of parameters leads to the following Taylor expansion:

$$\boldsymbol{\xi}' = \boldsymbol{\xi}\,(\boldsymbol{\eta}') = \boldsymbol{\xi} + \frac{\partial \boldsymbol{\xi}}{\partial \boldsymbol{\eta}} \cdot (\boldsymbol{\eta}' - \boldsymbol{\eta}) + \mathcal{O}\,(\boldsymbol{\eta}' - \boldsymbol{\eta})^2, \tag{II.18}$$

where the Jacobian $\partial\boldsymbol{\xi}/\partial\boldsymbol{\eta}$ is evaluated at $\boldsymbol{\eta}$. If the parameter values $\boldsymbol{\eta}$ and $\boldsymbol{\eta}'$ are taken close to each other, their difference $\boldsymbol{\eta}' - \boldsymbol{\eta} = \boldsymbol{\Delta}$ can be considered small. The sensitivity of $\boldsymbol{g}\,(\boldsymbol{x};\boldsymbol{p})$ is obtained by the following expansion

$$\boldsymbol{g}\,(\boldsymbol{\xi}';\boldsymbol{\eta}') = \boldsymbol{g}\left(\boldsymbol{\xi} + \frac{\partial \boldsymbol{\xi}}{\partial \boldsymbol{\eta}} \cdot \boldsymbol{\Delta} + \mathcal{O}\,(\boldsymbol{\Delta})^2; \boldsymbol{\eta} + \boldsymbol{\Delta}\right) = \boldsymbol{g}\,(\boldsymbol{\xi};\boldsymbol{\eta}) + \left(\frac{\partial \boldsymbol{g}}{\partial \boldsymbol{x}} \cdot \frac{\partial \boldsymbol{\xi}}{\partial \boldsymbol{\eta}} + \frac{\partial \boldsymbol{g}}{\partial \boldsymbol{p}}\right) \cdot \boldsymbol{\Delta} + \mathcal{O}\,(\boldsymbol{\Delta})^2.$$

The expression of interest is the term in the parenthesis:

$$\frac{\partial \boldsymbol{g}}{\partial \boldsymbol{x}} \cdot \frac{\partial \boldsymbol{\xi}}{\partial \boldsymbol{\eta}} + \frac{\partial \boldsymbol{g}}{\partial \boldsymbol{p}} = \frac{\partial \boldsymbol{g}}{\partial \boldsymbol{\eta}}.$$

Since the form of function $\boldsymbol{g}(\boldsymbol{x};\boldsymbol{p})$ is known, there is no difficulty in finding partial derivatives $\partial\boldsymbol{g}/\partial\boldsymbol{x}$ and $\partial\boldsymbol{g}/\partial\boldsymbol{p}$. The only unknown term is $\partial\boldsymbol{\xi}/\partial\boldsymbol{\eta}$, which is obtained by the following procedure. Substitution of the expansion (II.18) into the equality $\boldsymbol{f}(\boldsymbol{\xi}';\boldsymbol{\eta}') \equiv 0$ followed by the expansion of this equality results in

$$\boldsymbol{f}\left(\boldsymbol{\xi}+\frac{\partial\boldsymbol{\xi}}{\partial\boldsymbol{\eta}}\cdot\boldsymbol{\Delta}+\mathcal{O}\left(\boldsymbol{\Delta}\right)^2;\boldsymbol{\eta}+\boldsymbol{\Delta}\right)=\boldsymbol{f}\left(\boldsymbol{\xi};\boldsymbol{\eta}\right)+\left(\frac{\partial\boldsymbol{f}}{\partial\boldsymbol{x}}\cdot\frac{\partial\boldsymbol{\xi}}{\partial\boldsymbol{\eta}}+\frac{\partial\boldsymbol{f}}{\partial\boldsymbol{p}}\right)\cdot\boldsymbol{\Delta}+\mathcal{O}\left(\boldsymbol{\Delta}\right)^2\equiv 0.$$

The first term on RHS is zero since $\boldsymbol{\xi}$ is the solution of $\boldsymbol{f}(\boldsymbol{x};\boldsymbol{p}) = 0$ with parameters $\boldsymbol{p} = \boldsymbol{\eta}$. Therefore, it follows

$$\frac{\partial\boldsymbol{\xi}}{\partial\boldsymbol{\eta}}=-\left(\frac{\partial\boldsymbol{f}}{\partial\boldsymbol{x}}\right)^{-1}\cdot\frac{\partial\boldsymbol{f}}{\partial\boldsymbol{p}}.$$

Thus,

$$\frac{\partial\boldsymbol{g}}{\partial\boldsymbol{\eta}}=\frac{\partial\boldsymbol{g}}{\partial\boldsymbol{p}}-\frac{\partial\boldsymbol{g}}{\partial\boldsymbol{x}}\cdot\left(\frac{\partial\boldsymbol{f}}{\partial\boldsymbol{x}}\right)^{-1}\cdot\frac{\partial\boldsymbol{f}}{\partial\boldsymbol{p}}.$$

This equation expresses the sensitivity of $\boldsymbol{g}(\boldsymbol{x};\boldsymbol{p})$ towards the parameters in absolute terms. The relative perturbance matrix $\boldsymbol{\Gamma}$ is obtained by element-wise division and multiplication of absolute values of $\boldsymbol{g}(\boldsymbol{\xi};\boldsymbol{\eta})$ and $\boldsymbol{\eta}$ respectively:

$$\boldsymbol{\Gamma}=\left(\frac{\partial\boldsymbol{g}}{\partial\boldsymbol{p}}-\frac{\partial\boldsymbol{g}}{\partial\boldsymbol{x}}\cdot\left(\frac{\partial\boldsymbol{f}}{\partial\boldsymbol{x}}\right)^{-1}\cdot\frac{\partial\boldsymbol{f}}{\partial\boldsymbol{p}}\right)\overset{c}{\oslash}\left|\boldsymbol{g}\left(\boldsymbol{\xi};\boldsymbol{\eta}\right)\right|\overset{r}{\odot}\left|\boldsymbol{\eta}\right|^T.$$

The final form of $\boldsymbol{\Gamma}$ is obtained by denoting

$$\boldsymbol{\Lambda}^T=\frac{\partial\boldsymbol{g}}{\partial\boldsymbol{x}}\cdot\left(\frac{\partial\boldsymbol{f}}{\partial\boldsymbol{x}}\right)^{-1}.$$

□

A similar technique helps to find the variance of the solution of differential equation (II.9).

Proposition 2. *Let* $\boldsymbol{\xi}=\boldsymbol{\xi}(t;\boldsymbol{\eta})$ *be the solution of the set of ODEs*

$$\frac{\mathrm{d}\boldsymbol{x}}{\mathrm{d}t}=\boldsymbol{f}\left(t,\boldsymbol{x};\boldsymbol{p}\right),\quad \boldsymbol{f}\colon\mathbb{R}\times\mathbb{R}^n\times\mathbb{R}^m\to\mathbb{R}^n$$

with parameters $\boldsymbol{p}$ *set to* $\boldsymbol{\eta}\in\mathbb{R}^m$ *and some initial value* $\boldsymbol{x}(0)=\boldsymbol{x}_0\in\mathbb{R}^n$. *The relative perturbance multiplier matrix* $\boldsymbol{\Sigma}(t;\boldsymbol{\eta})\in\mathrm{Mat}\left(n\times m\right)$ *has the form*

$$\boldsymbol{\Sigma}(t;\boldsymbol{\eta})=\boldsymbol{\sigma}(t;\boldsymbol{\eta})\overset{c}{\oslash}\boldsymbol{\xi}(t;\boldsymbol{\eta})\overset{r}{\odot}\left|\boldsymbol{\eta}\right|^T \tag{II.19}$$

where $\boldsymbol{\sigma}(t;\boldsymbol{\eta})$ *is obtained as the solution of the variance equations*

$$\frac{\mathrm{d}\boldsymbol{\sigma}}{\mathrm{d}t} = \mathbf{A}(t)\cdot\boldsymbol{\sigma} + \mathbf{B}(t),$$
$$\boldsymbol{\sigma}(0) = 0,$$

where

$$\mathbf{A}(t) = \left(\frac{\partial \boldsymbol{f}}{\partial \boldsymbol{x}}\right)_{\boldsymbol{p}} (t,\boldsymbol{\xi};\boldsymbol{\eta}),$$
$$\mathbf{B}(t) = \left(\frac{\partial \boldsymbol{f}}{\partial \boldsymbol{p}}\right)_{\boldsymbol{x}} (t,\boldsymbol{\xi};\boldsymbol{\eta}).$$

Note. Perturbance multiplier (II.19) is only valid for practical purposes for small variations in the set of parameters and only for a small increment of time. As time passes, the perturbed solution deviates from the initial solution far enough to produce a new solution line. To study the perturbance further, coefficients $\mathbf{A}(t)$ and $\mathbf{B}(t)$ must be recalculated and the initial point $\boldsymbol{x}_0$ must shifted for the new solution.

Note. There is no advantage in this case to consider a more general function $\boldsymbol{g}(t,\boldsymbol{x};\boldsymbol{p})$ as its variance requires variances of the dependent variables $\boldsymbol{\sigma}(t;\boldsymbol{\eta})$, which are obtained by solving ODEs. In contrast to algebraic equations, it is not possible to integrate them directly into the equation for $\boldsymbol{g}(t,\boldsymbol{x};\boldsymbol{p})$ variance.

To illustrate the application of the perturbance matrix multiplier $\boldsymbol{\Gamma}$, consider the dependence of saturation s on hydraulic parameters in SSUM. Let's choose $K_s = 5.51\ \mathrm{m\cdot s^{-1}}$and $q_{\text{in}} = 10\ \mathrm{L\cdot m^{-2}\cdot h}$ and the van Genuchten model with $\ell = 1/2$ and $n = 1.3$. Solution of (II.11) yields $s = 0.283$. Since we are interested in the sensitivity of s, $g(s,\{\ell,n,\Bbbk\}) \equiv s$ and $\partial g/\partial \boldsymbol{p} = 0$, where $\boldsymbol{p} = \{\ell,n,\Bbbk\}$ is a parameter list. As it will become apparent below, the dependence on $\Bbbk$ is very low. Thus, it is more informative to use its order of magnitude by introducing another parameter $x = \lg\Bbbk$, resulting in $\boldsymbol{p} = \{\ell,n,x\}$. Matrix $\boldsymbol{\Gamma}$ in this case is a 1×3 row matrix with the following expression

$$\boldsymbol{\Gamma} = \frac{-\Lambda\cdot\left(\frac{\partial f}{\partial \boldsymbol{p}}\right)_s (s;\{\ell,n,x\})}{s} \overset{r}{\odot} \{\ell,n,x\},$$

where Λ is a scalar obtained from

$$\left(\frac{\partial f}{\partial s}\right)_{\boldsymbol{p}} (s;\{\ell,n,x\})\cdot\Lambda = 1$$

and $f = K_r(s; \{\ell, n, x\}) - 10^x$. Substitution of parameter values and the solution $s = 0.283$ results in

$$\mathbf{\Gamma} = \begin{bmatrix} 0.0687 & -4.70 & 1.58 \end{bmatrix}.$$

If there is 5% perturbation of ℓ, this will result in only $0.0687 \times 5\% = 0.344\%$ change in s. However, if n is increased by 5%, saturation will drop by $4.7 \times 5\% = 23.5\%$. Notice that the change in $x = \lg \hbar$ will cause a comparable change in s. Thus, large changes in the flow rate $\hbar$ will only have marginal effects on saturation.

Up to this point, the flow in packed rock beds was considered at steady state. However, it is unclear if the steady state is even achievable in this system in a reasonable time. The only way to investigate it is to start looking at transient equation (II.1). The solution of this equation is gradually built up by first considering a one-element model, extending it to a full one-dimensional model and finally formulating a numerical method for a two-dimensional model.

§ 4. Transient one-element model (TOEM)

The simplest way to introduce transient effects is to ignore spatial variances. The mass balance over this system in an unsaturated regime leads to the equation

$$\frac{\mathrm{d}s}{\mathrm{d}t} = \frac{q_{\text{in}} - K(s)}{\Delta\vartheta\, H},$$

where q_{in} is inlet flow rate, $\Delta\vartheta = \vartheta_s - \vartheta_r$ is total water content variance and H is the height of the domain. As there are a few interlinked parameters, a more informative form of the equation is obtained by introducing dimensionless time. First, the conductivity term can be split into saturated and unsaturated parts: $K(s) = K_s K_r(s)$. Dimensionless time τ is introduced as follows

$$t = \frac{H}{K_s}\tau = T\tau.$$

Then the above equation takes the form

$$\frac{\mathrm{d}s}{\mathrm{d}\tau} = \frac{\hbar - K_r(s)}{\Delta\vartheta}, \tag{II.20}$$

where, as before, $\Bbbk = q_{\text{in}}/K_s$. Equation (II.20) can be solved by separating the variables:

$$\frac{\Delta\vartheta \, \mathrm{d}s}{\Bbbk - K_r(s)} = \mathrm{d}\tau$$
$$\int_{s_0}^{s} \frac{\Delta\vartheta \, \mathrm{d}s}{\Bbbk - K_r(s)} = \int_0^{\tau} \mathrm{d}\tau$$

The expression on the left-hand side (LHS), however, cannot be integrated analytically. Furthermore, the function of interest $s(\tau)$ can only be obtained by further inverting the integral of the expression on the LHS. Therefore, the solution is more easily obtained by direct numerical integration of equation (II.20).

TOEM is implemented as a Fortran program with an MS Excel spreadsheet interface. The input data $\{\Delta\vartheta, n, K_s, q_{\text{in}}, Z\}$ is passed to a driver function `run_toem` of the dynamically linked library `TOEM.dll` with time points (Appendix A, TOEM source code, module `TOEM`). Differential equation equation (II.20) is solved in `run_toem` using the `LSODA` routine of the `ODEPACK` library (Hindmarsh, 1983). The solution is obtained as a vector of saturation values at provided time points.

Typical infiltration and drainage curves for simulations run with parameters listed in Table II.1 are shown in Figure II.3. Time-scales for infiltration and drainage differ by an order of magnitude since the latter is much slower. Furthermore, even with this vastly extended time-scale the drainage process is still far away from being steady-state ($s = 0$). This result is in direct contradiction to the practice of estimating ϑ_r from drainage experiments (used by, e.g. Dixon and Afewu, 2010) as it would be difficult to obtain accurate estimates of ϑ_r given the long time-scale of drainage. The effect of the extended time scale for the drainage is also noticeable if the flow rate is increased and then brought back to the original value. Figure II.4 demonstrates this effect in case of $\Bbbk$ being quadrupled for $\tau = 3 \times 10^4$ and than brought back to $\Bbbk = 10^{-6}$. The drainage time-to-steady-state is three times longer compared to infiltration in this case. This asymmetry is caused by the strong dependence of hydraulic conductivity on saturation, $K = K(s)$. As a result, a small increase in saturation during infiltration leads to much higher conductivity leading to faster liquid spread and further increase in saturation. Conversely, a small drop in saturation during drainage results in much lower conductivity that slows further liquid expulsion from the solid matrix. The extent of the asymmetry depends on hydraulic parameters. This feature of the solution may be used in explaining the hysteresis in packed rock beds as will be discussed in subsection 1.2 of Chapter IV.

Table II.1: Typical parameters for the simple transient model.

Parameter	Value	Units	Comment
$\hbar$	10^{-6}	–	
n	1.3	–	Hydraulic parameter (van Genuchten model)
m	0.231	–	$m = 1 - 1/n$
ϑ_r	0.02	–	Residual water content, assumed as 5% of saturated water content
ϑ_s	0.4	–	Saturated water content
$\tau_{\max,1}$	2×10^5	–	Maximum time of infiltration simulation
$s_{0,1}$	0.01	–	Initial saturation for infiltration curve
$\tau_{\max,2}$	2×10^6	–	Maximum time for drainage simulation
$s_{0,2}$	0.3	–	Initial saturation for drainage curve

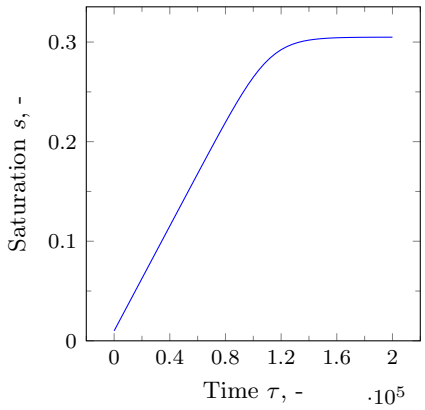

(a) Infiltration

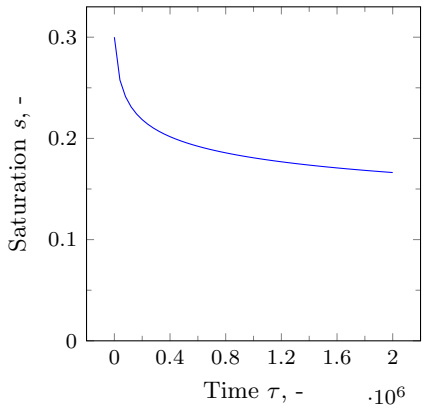

(b) Drainage

Figure II.3: Infiltration and drainage curves of the transient one-element model run with parameters listed in Table II.1.

Stability of the solution is confirmed by the derivative

$$\frac{\partial}{\partial s}\left(\frac{\hbar - K_r(s)}{\Delta\vartheta}\right) = -\frac{1}{\Delta\vartheta}K_r'(s)$$

being negative along the solution line since $K_r(s)$ is strictly a growing function and thus $K_r'(s) > 0$ (Hairer et al., 2008).

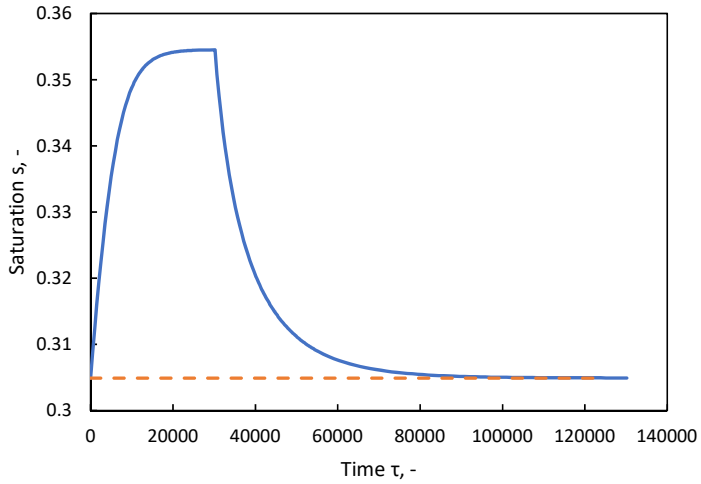

Figure II.4: The results of TOEM with increased and decreased inlet flow rate. The dashed line shows a steady-state saturation at the original (and final) flow rate.

§ 5. Numerical solution of the one-dimensional Richards equation

1. Formulation. Finite volumes scheme. It is common in soil sciences to formulate equation (II.2) in terms of pressure h as it results in a form more convenient for fully saturated regimes (Philip, 1957a; Haverkamp et al., 1977; Celia et al., 1990). However, this study uses a saturation-based formulation since full saturation in the context of heap leaching would result in the heap's mechanical instability and thus, the flow in this regime is of no interest. Furthermore, a saturation-based equation is easier to formulate in a mass conservative way. Although some simplification can be gained by using the Kirchhoff transformation, it requires repeated solution of equations of the form

$$\int_{h_0}^{h} K(h)\,dh - U = 0$$

for h with a fixed U that is non-trivial for the van Genuchten hydraulic model. Moreover, Haverkamp et al. (1977) found no benefits of using the Kirchhoff transformation in terms of solution stability. Thus, equation (II.2) is solved directly for saturation. The finite volumes method (FVM) was used for spatial discretisation. Compared to the finite differences (FDM) and finite elements (FEM) methods, it offers local mass conservation and simple treatment of fluxes. Furthermore, the FEM was shown to be unstable for the Richards equation without a special form of the mass matrix (Celia et al., 1990).

The domain of the problem (II.2) is the closed interval $[0, H]$ where $z = 0$ refers to the top of the packing (a heap or a column) and $z = H$ refers to its bottom. The domain is split into N volumes with boundaries $\ell_0, \ell_1, \ldots, \ell_N$. The centroid of each volume is given as follows

$$c_i = \frac{\ell_i + \ell_{i+1}}{2}.$$

The mass balance over the volume i between faces ℓ_i and ℓ_{i+1} is given as

$$\Delta\vartheta \frac{\mathrm{d}s_i}{\mathrm{d}t} = \frac{J_{i,\text{in}} - J_{i,\text{out}}}{\Delta z_i}, \tag{II.21}$$

where s_i is the average value of saturation on the volume i and also the approximation of $s(c_i)$, $J_{i,\text{in}} = J_{i-1,\text{out}} = J_{i-\frac{1}{2}}$ and $J_{i,\text{out}} = J_{i+1,\text{in}} = J_{i+\frac{1}{2}}$ are fluxes in and out the volume respectively, and $\Delta z_i = \ell_{i+1} - \ell_i$ is the size of the volume. Equality $J_{i,\text{in}} = J_{i-1,\text{out}}$ provides the conservation of the liquid mass between the volumes. Fluxes are defined on the boundaries of the volume according to Darcy's law:

$$J_{i-\frac{1}{2}} = -K_{i-\frac{1}{2}} \left[(\nabla h)_{i-\frac{1}{2}} - 1 \right], \tag{II.22}$$

where $K_{i-\frac{1}{2}}$ is the value of hydraulic conductivity on the boundary ℓ_i and $(\nabla h)_{i-\frac{1}{2}}$ is the gradient of the capillary pressure on that boundary.

Since conductivity is a function of saturation and saturation is defined on centroids, conductivities on volume's faces need to be somehow approximated. There are two possible ways of doing this: conductivity either can be approximated using the harmonic average of its centroid values (assuming all volumes are equal, otherwise weighing coefficients must be applied, Manzini and Ferraris, 2004):

$$\frac{1}{K_{i-\frac{1}{2}}} = \frac{1}{2}\left(\frac{1}{K_{i-1}} + \frac{1}{K_i}\right)$$

or the boundary saturation $s_{i-\frac{1}{2}}$ is found as a linear average (arithmetic average for equal volumes) between s_{i-1} and s_i with conductivity calculated directly for $s_{i-\frac{1}{2}}$. The latter method results in a higher number of calculations in two- and three-dimensional domains due to the higher number of faces there. However, in one-dimensional problems there is no such penalty. Furthermore, the trials with harmonic averages showed a loss of stability due to the extremely rapid change of conductivity with saturation (a similar effect was observed by Dixon and Afewu (2010), prompting them to use a (strictly speaking) unphysical arithmetic average of conductivity).The loss of stability can be illustrated as follows. Consider volumes 1 and 2, with volume 1 above volume 2. Saturations in each of the

volume are s_1 and s_2 respectively and corresponding conductivities are K_1 and K_2. If $s_1 > s_2$, it follows that $K_1 \gg K_2$. Their harmonic average is then

$$K = \frac{2}{\frac{1}{K_1} + \frac{1}{K_2}} \approx 2K_2 \ll K_1,$$

i.e. it is dominated by the lower conductivity. As a result, conductivity between the volumes is extremely small and does not allow the liquid to flow from volume 1 to volume 2, eventually leading to the flooding of volume 1. In contrast, the second approach assumes linear distribution of saturation between the centroids, resulting in a boundary saturation higher than $\frac{1}{2}s_1$producing boundary conductivity $K \gg K_2$.

Capillary pressure gradient $(\nabla h)_{i-\frac{1}{2}}$ is approximated using pressure values on the centroids:

$$(\nabla h)_{i-\frac{1}{2}} = \frac{h(s_i) - h(s_{i-1})}{\boldsymbol{c}_i - \boldsymbol{c}_{i-1}}. \tag{II.23}$$

Since the inlet flow rate is usually known, the top boundary condition is specified by prescribing the flux through the top boundary of the first volume:

$$J_{-\frac{1}{2}} = J_{0,\text{in}} = q_{\text{in}}.$$

At the bottom, the liquid flows out purely due to gravity, thus $(\nabla h)_{N+\frac{1}{2}} = 0$. It follows that

$$J_{N+\frac{1}{2}} = J_{N,\text{out}} = K_{N+\frac{1}{2}}.$$

Finally, the value $K_{N+\frac{1}{2}}$ is approximated by $K_N = K(s_N)$.

Spatial discretisation results in the set of ODEs (II.21). As with TOEM, this set of ODEs is solved using the LSODA procedure of the ODEPACK library (Hindmarsh, 1983). A Fortran program with a MS Excel interface was developed implementing the method (the program listing is attached in the appendix A, Richards1D source code).

2. Infiltration curve. The model was run with the parameters of Table II.2, and the results are shown in Figure II.5. The results show a gradual increase in saturation at the top of the column and the development of a percolation front that reaches the bottom of the 1 m column after approximately 5 hours. As soon as the percolation front reaches the bottom, saturation at all depths of the column equalises and rises to a steady-state value.

Table II.2: Parameters used for infiltration simulation.

Parameter	Value	Units	Comment
K_s	5.51	$\mathrm{m} \cdot \mathrm{s}^{-1}$	Saturated conductivity
α	3.0	m^{-1}	Hydraulic parameter: inverse of bubbling pressure
n	1.30	–	Hydraulic parameter
$m = 1 - 1/n$	0.230	–	Hydraulic parameter
ϑ_r	0.0185	–	Residual water content, taken 5% of ϑ_s
ϑ_s	0.370	–	Saturated water content
q_{in}	2.78×10^{-6}	$\mathrm{m} \cdot \mathrm{s}^{-1}$	Inlet flow rate of $10\ \mathrm{L} \cdot \mathrm{m}^{-2} \cdot \mathrm{h}^{-1}$
H	1.0	m	Height of the bed
N	40	–	Number of elements
s_0	0.01	–	Initial saturation
t_{max}	12.0	h	Time span of simulation
M	48	–	Number of output time points

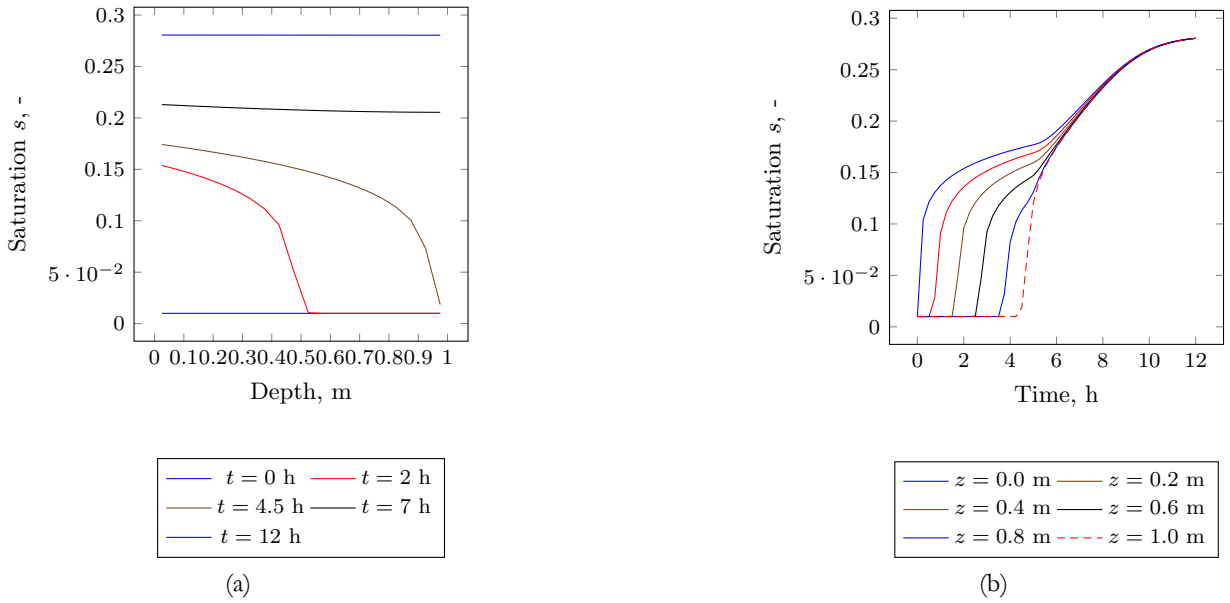

Figure II.5: Example of the model run with parameters shown in Table II.2: (a) variation of saturation with depth at different time points and (b) variation of saturation with time for different depths.

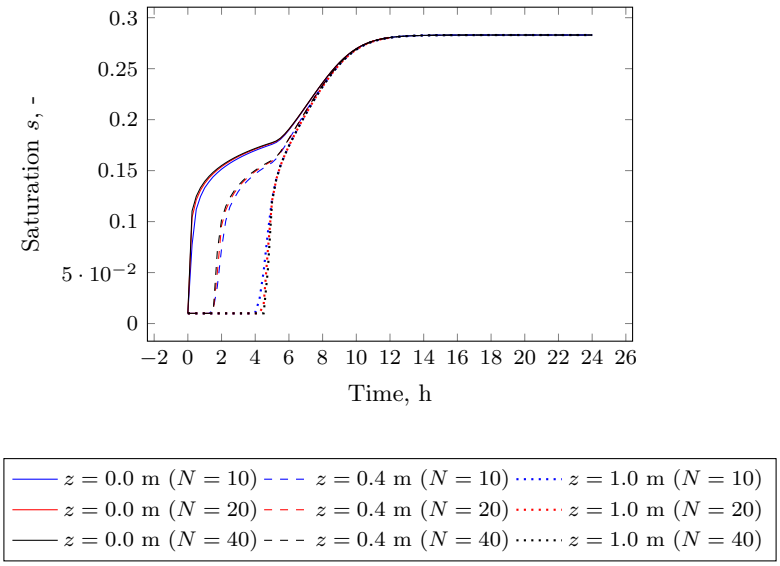

Figure II.6: Model results on different mesh sizes showing independence of the model from the mesh size.

3. Independence from the mesh. A standard check of the numerical scheme correctness is the results' independence from the mesh size. Figure II.6 demonstrates saturation variation with time for the model with the same parameters as in Table II.2 except for the number of elements N that was chosen to be 10, 20 and 40. It shows little difference between the results of different mesh size with results for $N = 20$ and $N = 40$ being almost indistinguishable.

4. Drainage. The drainage curve is obtained by setting the inlet flow rate to zero and starting from a larger value of saturation. In keeping with the previous example, where a saturation value of about 0.28 was achieved, the model was run with the same parameters as in Table II.2, but with $q_{\text{in}} = 0$ and $s_0 = 0.28$ (uniform throughout the domain) over 48 hours. The results of the simulation are shown in Figure II.7.

It is evident that during drainage there is very little variation in saturation with depth. Furthermore, in contrast to infiltration, the process is very slow. In Figure II.7b the tail of the curve becomes flatter but the drainage process still continues even after 48 hours. This effect is due to non-linearity of conductivity function $K_r(s)$: as saturation falls, conductivity at the bottom boundary falls (exponentially) and, thus, slows down the drainage.

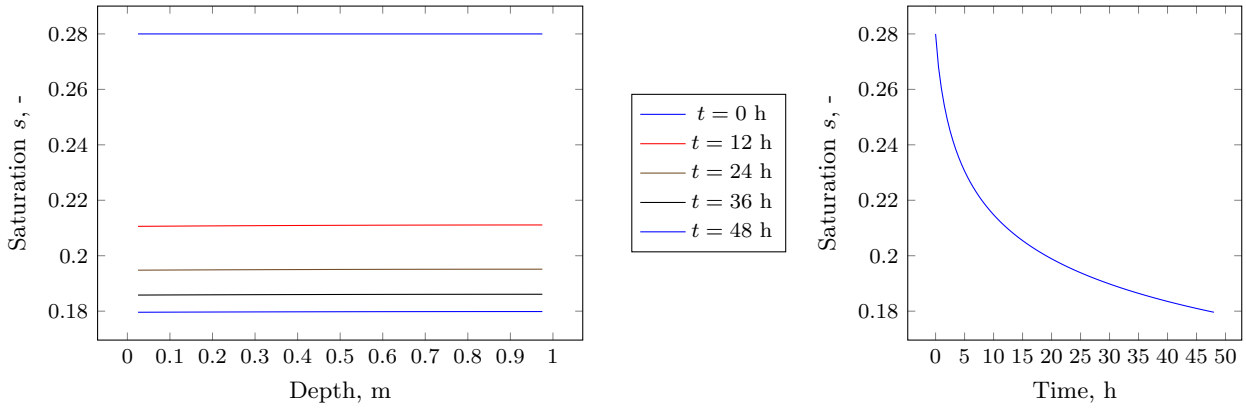

(a) (b)

Figure II.7: Variance of saturation (a) with depth at different time points and (b) with time for the top element for the drainage simulation with parameters of Table II.2 with exception of $q_{\text{in}} = 0$, $s_0 = 0.28$ and $t_{\max} = 48$ hours.

5. Intermittent flow. Combining infiltration and drainage simulation, one naturally arrives at intermittent flow. To emphasise important features of the simulation results it is necessary to transform the Richards equation (II.2) into a dimensionless form. There are only two scales present in this equation, length and time. Using the height of the bed H, the dimensionless length and, thus, spatial coordinate becomes

$$\zeta = \frac{z}{H}.$$

Dimensionless time is introduced using saturated conductivity ($\text{m} \cdot \text{s}^{-1}$ in SI units):

$$\tau = \frac{K_s}{H} t.$$

It is important to note, this relation only makes sense if it can be assumed that the saturated conductivity K_s is uniform throughout the bed. Substitution of these expressions for coordinate z and time t into equation (II.2) results in the following equation:

$$\Delta\vartheta \frac{\partial s}{\partial \tau} - \frac{\partial}{\partial \zeta}\left[K_r(s)\left(\frac{\partial \psi}{\partial \zeta} - 1\right)\right] = 0. \tag{II.24}$$

where $\psi = h/H$ is the dimensionless capillary pressure.

Let's examine properties of the dimensionless equation (II.24). First, recall that capillary pressure is a non-linear function of saturation described as the inverse of the equation (II.14). This equation can be re-written in terms of ψ as follows:

$$s = \left(\frac{1}{1 + |\alpha H \psi|^n}\right)^m$$

Therefore, to describe this relation a dimensionless inverse of the bubbling pressure $\alpha' = \alpha H$ must be introduced.

Dimensionless time scale $\tau = 1$ has the following meaning: it is the time required for the liquid at full saturation (with liquid flow equal to K_s) to go through a 1 m packed bed. Considering the scale of permeability k being in the range of 10^{-12}–10^{-8} m^2 (see Table I.1) and the fact that

$$K_s = \frac{\rho g}{\mu} k \approx 10^7 k,$$

it follows that $10^{-5} \leq K_s \leq 10^{-1}$. Thus, $\tau = 1$ in an absolute scale is 10–10^5 s for different packings. Therefore, in modelling a typical heap leaching unsaturated flow it is expected to have values of τ in the order of magnitude of 10^0–10^4 for hours and 10^1–10^5 for days.

The dimensionless form (II.24) highlights important features: time and the height of the bed are inversely proportional. Thus, if the model is correct, experiments with short beds must predict the results of tall beds with the time proportionally scaled. Application of this principle to intermittent flow shows that we do not need to concern ourselves with the effect of varying height of the bed but only with periods of on and off time of the flow. More specifically, if the effect of changing height from H_1 to H_2 is considered (time periods t_{on} and t_{off} are the same), it is equivalent to changing the dimensionless on and off time periods as follows:

$$\tau_{\kappa,2} = \frac{H_1}{H_2} \tau_{\kappa.1},$$

where $\tau_{\kappa,i}$ is "on" and "off" (index κ) time period for the case of $i = 1, 2$. For example, if $H_2 = 2H_1$, the dimensionless time periods will be twice shorter. Qualitatively there are two important results regarding intermittent flow. First, consider model parameters in Table II.3, which are roughly equivalent to the parameters in Table II.2. Time intervals for which the flow is on and off are quite short (roughly, 15 min equivalent). The results show that the intermittent nature of the flow is absorbed by the bed, with volumes lying deeper in the bed almost not showing the fluctuation (Figure II.8). The saturation behaves almost as under constant flow, with the rate half of the $q_{\text{in, on}}$ (inlet flow rate when flow is on) and the results shown in Figure II.8 are comparable to the constant flow results in Figure II.5. In contrast, when "on" and "off" time intervals are long, saturation does show the fluctuation. Its distribution, however, remains uniform once the percolation front reached the bottom (see Figure II.9). The flow out of the column reaches the inlet flow at the end of the "on" period, Figure II.10.

Table II.3: Dimensionless model parameters, roughly equivalent to parameters listed in Table II.2, for intermittent flow with short "on" and "off" intervals.

Parameter	Value	Comment
α'	3.0	Inverse of bubbling pressure
n	1.30	Hydraulic parameter
$m = 1 - 1/n$	0.230	Hydraulic parameter
ϑ_r	0.0185	Residual water content, taken 5% of ϑ_s
ϑ_s	0.370	Saturated water content
$q_{\text{in, on}}$	1.01×10^{-6}	Inlet flow rate when flow is on, equivalent to $20\ \text{L} \cdot \text{m}^{-2} \cdot \text{h}^{-1}$
τ_{on}	5×10^3	Time interval during which the inlet flow is on, roughly equivalent to 15 min
τ_{off}	5×10^3	Time interval during which the inlet flow is off
N	20	Number of elements
s_0	0.01	Initial saturation
τ_{max}	2.5×10^5	Time span of simulation, roughly half a day
M	1001	Number of output time points

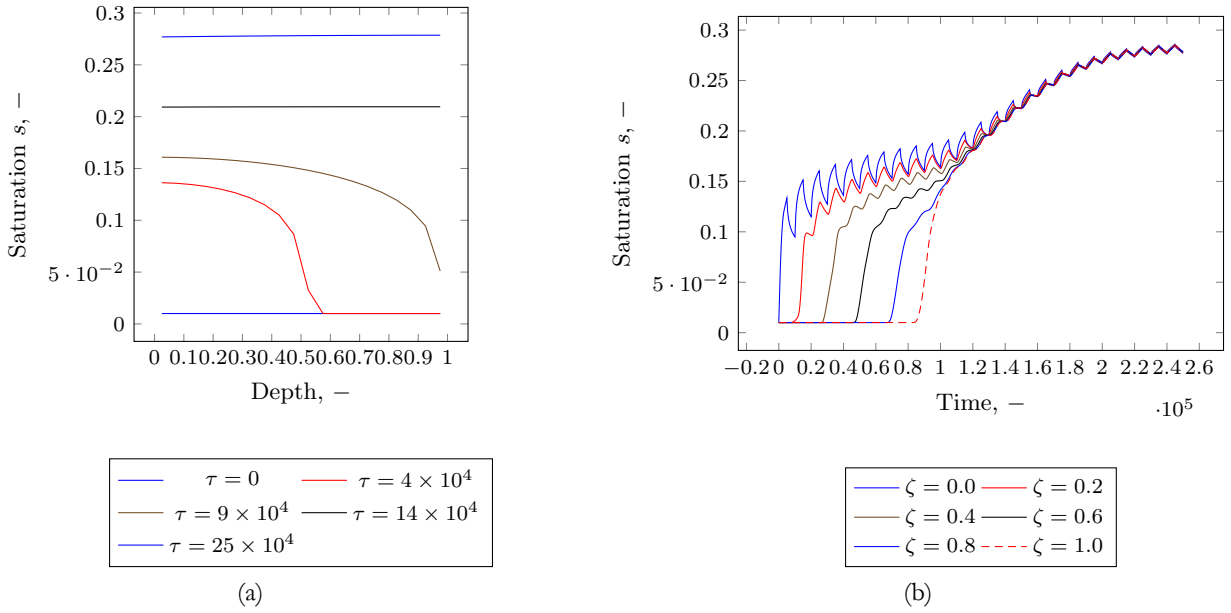

Figure II.8: Infiltration curve of the dimensionless model with parameters listed in Table II.3 for intermittent flow with short "on" and "off" intervals.

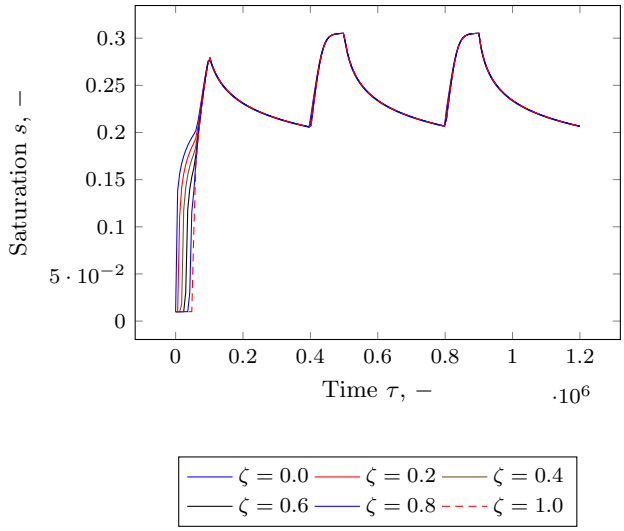

Figure II.9: Infiltration curve of the dimensionless model for intermittent flow with the parameters listed in Table II.3 except for $\tau_{\text{on}} = 10^5$ and $\tau_{\text{off}} = 3 \times 10^5$, approximately equivalent to 5 hours "on" and 15 hours "off" for the parameters of Table II.2, and longer simulation time.

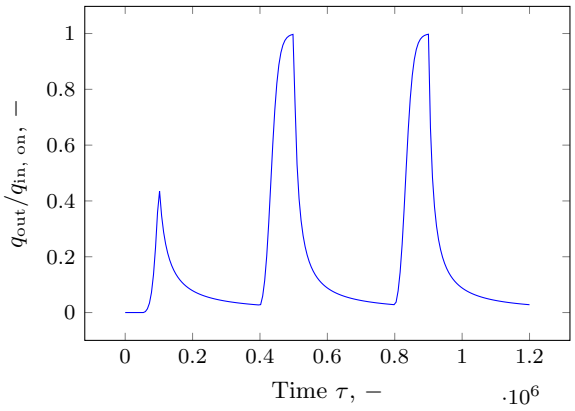

Figure II.10: Predicted relative flow rate out of the column for the intermittent inlet flow with long "on" and "off" periods of irrigation ($\tau_{\text{on}} = 10^5$ and $\tau_{\text{off}} = 3 \times 10^5$ respectively).

6. Hydraulic parameter perturbation. Sensitivity analysis of the steady-state Richards equation has shown that the solution is quite stable with regards to perturbation of hydraulic parameters (as far as the perturbation can be considered small). Parameter n of the van Genuchten unsaturated model is an exception. Numerical solution provides a way to test these results.

Discretisation of the model with the perturbed parameters requires some clarification. Hydraulic parameters for $K = K(s)$ in flux expression (II.22) need to be defined on element boundaries, whereas parameters in the expression for the gradient of the capillary pressure (II.23) need to be defined on the centroids. While all parameters were uniform throughout the volume, it was not necessary to

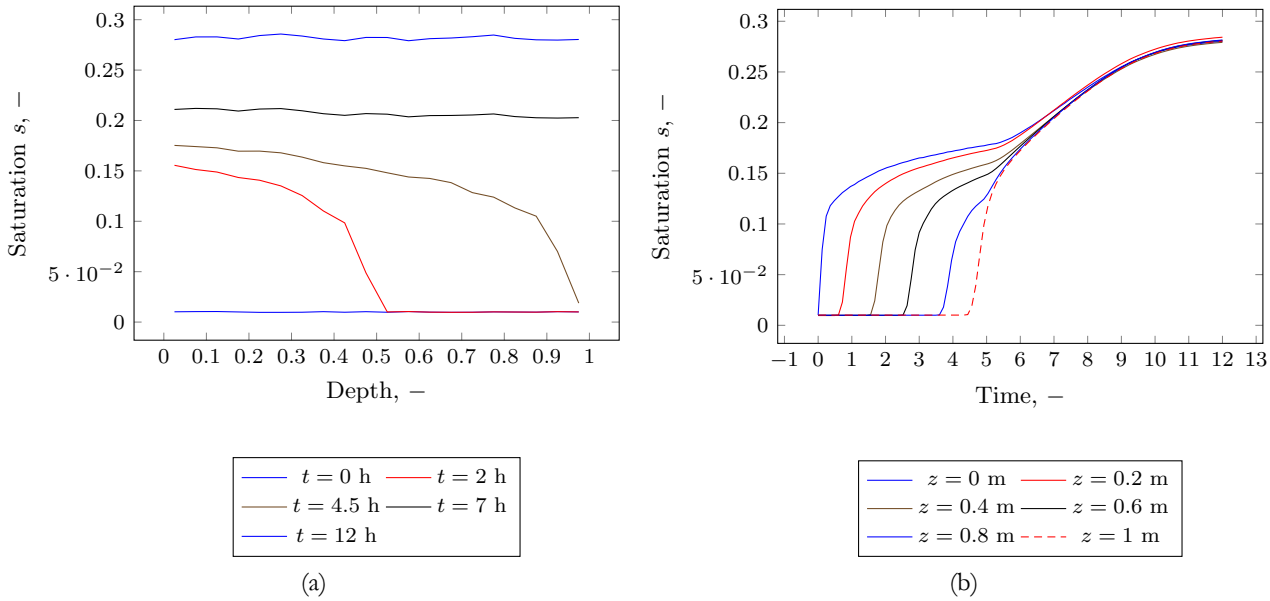

Figure II.11: An example of the results of the perturbed model with the base parameters listed in Table II.2 with each of $\lg(q_{\text{in}}/K_s)$, α and s_0 randomly perturbed by maximum of $\pm 5\%$ (compare with the results of unperturbed model in Figure II.5).

distinguish between them. Now, however, perturbations are defined on the boundaries as follows:

$$\tilde{P} = P(1 + r),$$

where P is the base value of the parameter, r is a randomness defined as a uniformly distributed random value between some boundaries $-r_{\max} < r < r_{\max}$, and $\tilde{P}$ is the perturbed value of the parameter. To provide continuity, parameter values on the centroids are defined as linear averages of their boundary values.

To confirm the stability of the model with respect to $\lg(q_{\text{in}}/K_s)$, α and s_0, the simulation was run with base parameters listed in Table II.2 where the mentioned parameters were randomly perturbed by a maximum of $\pm 5\%$. An example of the results of the model simulation are shown in Figure II.11a and Figure II.11b. While Figure II.11a demonstrates just a slightly distortion compared to Figure II.5a, Figures II.5b and II.11b are virtually indistinguishable.

In contrast, if parameter n is randomly perturbed by maximum of $\pm 5\%$ around the base value of 1.3, saturation distribution sees more significant changes (Figure II.12). Steady-state saturation ranges from 0.25 to just above 0.35, or $s \approx 0.3 \pm 0.05 = 0.3 \pm 17\%$. Steady-state sensitivity analysis (subsection 3.2) can be applied to individual volumes of the perturbed model once it reaches a steady

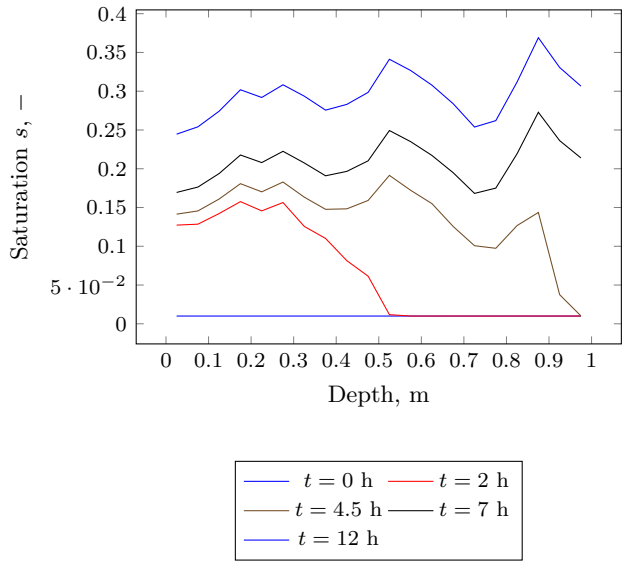

Figure II.12: Saturation distribution with increased depth for the model with the base parameters listed in Table II.2 and with parameter n (and, as a result, $m = 1 - 1/n$ as well) perturbed by 5% at each element boundary.

state, since each volume will be governed by equation (II.11) of the SSUM. Choosing the base value $n = 1.3$, it was shown that if n is varied $\pm 5\%$, the saturation will vary $\pm 23.5\%$ around $s \approx 0.3$. Since in the perturbed model n was varied randomly, but not exceeding the $\pm 5\%$ of its base value, it is expected that the saturation in each volume will fall within $0.3 \pm 23.5\%$. Numerical results confirm the analytical deduction.

Note, the saturation distribution shown in Figure II.12 is just an example with one particular set of randomly distributed values of n. However, the analytical results dictate that all the runs will produce the distributions falling in the band of $s = 0.3 \pm 23.5\%$. Since a comprehensive quantitative analysis of this result is not a focus of this study, it was not pursued further.

§ 6. Numerical solution of the two-dimensional Richards equation: Richards2D model

There are a couple of phenomena that the one-dimensional Richards equation cannot capture. Firstly, if the flow is not administered uniformly at the top, but for example, via a single drip emitter, there is lateral water movement. This effect was investigated by Dixon and Afewu (2011) for a cylindrical

column with a single drip emitter located at its centre. The next extension is to investigate the effect of changing the drip emitter location. Secondly, a lower-conductivity barrier in the one-dimensional model results in increased saturation at the barrier, which would push up the conductivity value as the mass balance dictates "what comes in — must come out". In contrast, in two-dimensional geometry it is possible for the flow to go around the barrier, leaving saturation levels there low. This section formulates a two-dimensional flow model based on the Richards equation and presents possible effects that can be captured by such a model.

1. Finite volumes scheme. Finite volumes discretisation uses a structured rectangular mesh. The mesh boundaries were drawn at equal distances $\Delta x = W/N_x$ and $\Delta z = H/N_z$, where N_x and N_z are the number of elements in the x and z direction respectively. The position of each element is defined by a pair of indices (i, j), $i = 1, \ldots, N_z$, $j = 1, \ldots, N_x$. Element (i, j) has:

- its left face (boundary) at $\Delta x(j-1)$ and its right boundary at $\Delta x\, j$ in the x-direction;
- its top face at $\Delta z(i-1)$ and its bottom face at $\Delta z\, i$ in the y-direction;
- its centroid at $(\Delta x(i-1/2), \Delta z(i-1/2))$;
- the distance Δx and Δz between the faces in the x and z direction respectively.

The mass balance over the element (i, j) has the form:

$$\Delta\vartheta^c_{ij}\frac{\mathrm{d}s^c_{ij}}{\mathrm{d}t} = -\frac{1}{\mathscr{V}^c_{ij}}\left(\mathscr{A}^f_{x,i\,j+1}V^f_{x,i\,j+1} - \mathscr{A}_{x,i\,j}V^f_{x,i\,j}\right) - \frac{1}{\mathscr{V}^c_{ij}}\left(\mathscr{A}^f_{z,i+1\,j}V^f_{z,i+1\,j} - \mathscr{A}^f_{z,i\,j}V^f_{z,i\,j}\right), \quad \text{(II.25)}$$

where $V^f_{x,ij}$ is the specific discharge (flux) through the left face of the element (i, j) and $V^f_{z,i\,j}$ is the flux through the top face of the element (i, j). Superscripts c and f indicate whether the quantity is defined on the centroid or the face of the element. The fluxes (on the faces) are approximated using Darcy's law:

$$V^f_{x,i\,j} \approx -K^f_{x,i\,j}\frac{h\left(s^c_{i\,j+1}\right) - h\left(s^c_{i\,j}\right)}{dx^c_{i\,j}},$$
$$V^f_{z,i\,j} \approx -K^f_{z,i\,j}\frac{h\left(s^c_{i+1\,j}\right) - h\left(s^c_{i\,j}\right)}{dz^c_{i\,j}},$$

where $dx^c_{i\,j}$ and $dz^c_{i\,j}$ are the distances between the centroids of the elements (i, j)–$(i, j+1)$ and (i, j)–$(i+1, j)$ respectively. $K^f_{x,i\,j}$ and $K^f_{z,i\,j}$ denote hydraulic conductivities on the vertical (with the

Table II.4: Base parameter values of Richards2D model

Parameter	Value	Units	Comment
W	1	m	Width of the domain
H	1	m	Height of the domain
ℓ	$1/2$	–	Mualem hydraulic parameter
α	3.0	m^{-1}	Inverse of bubbling pressure
n	1.30	–	Van Genuchten hydraulic parameter
$m = 1 - 1/n$	0.230	–	Van Genuchten hydraulic parameter
K_s	0.01	$\mathrm{m} \cdot \mathrm{s}^{-1}$	Saturated conductivity
$\Delta\vartheta$	0.350		Range of water content
$q_{\text{in, average}}$	10	$\mathrm{L} \cdot \mathrm{m}^{-2} \cdot \mathrm{h}$	Average inlet flow rate. In case of single drip emitter, actual flow is increased proportionally
N_x	40	–	Number of elements in the (lateral) x-direction
N_z	40	–	Number if elements in the (vertical) z-direction
N_t	100	–	Number of time steps
s_0	0.01	–	Initial saturation
t_{final}	8	h	Overall time of simulation

normal in x-direction) and horizontal faces respectively. These conductivities need to be calculated using interpolated values for saturations. For example, for $K^f_{x,i\,j} = K\left(s^f_{x,i\,j}\right)$ the interpolated saturation value is calculated as a linear average:

$$s^f_{x,i\,j} = \left(s^c_{i\,j+1} - s^c_{i\,j}\right) \frac{dx^{cf+}_{i\,j}}{dx^{cf+}_{i\,j} + dx^{cf-}_{i\,j+1}} + s^c_{i\,j},$$

where $dx^{cf\pm}_{i\,j}$ denotes the distance from the centroid of the element (i, j) to its left face (with "$-$" in superscript) or to its right face (with "$+$" in superscript). These distances do not coincide if $\mathcal{A}^f_{x,i\,j} \neq \mathcal{A}^f_{x,i\,j+1}$ as the centroid is the centre of mass of the element and will be positioned closer to the face with the larger area. The ordinary differential equations (II.25) are solved using the LSODA ODE solver from the ODEPACK Fortran library (Hindmarsh, 1983). The full source code is attached in Appendix A, Richards2D source code. To investigate the two-dimensional phenomena predicted by this model, the base parameters listed in Table II.4 were used.

2. Single drip emitter position. The uniform inlet flow model results are identical to the one-dimensional model since the capillary pressure gradient in the lateral direction is zero. Thus, a single-point inlet flow was investigated. Placing a single-drip emitter at the centre of the domain,[2] produces

[2]Strictly speaking slightly closer to the left boundary with $j = 20$ since there are even number of elements along x-direction.

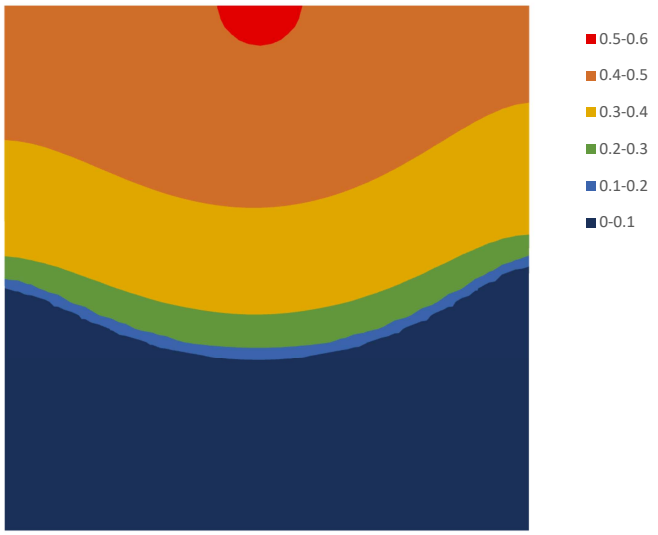

Figure II.13: Saturation profile according to the Richards2D model with base parameters at time $t = 8$ h.

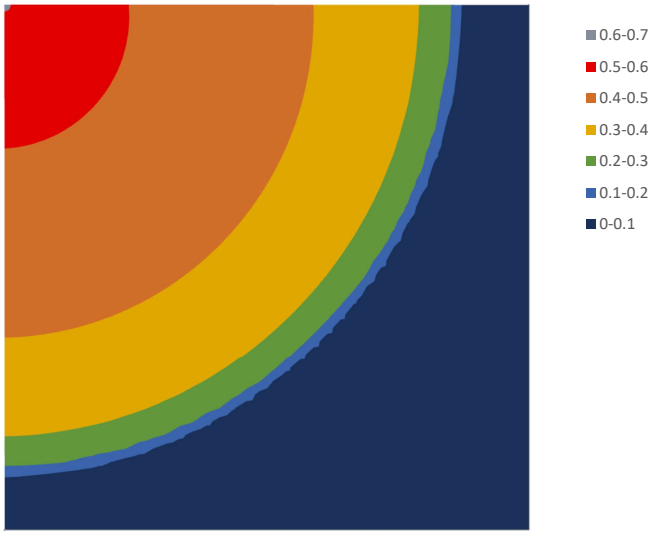

Figure II.14: Saturation profile according to the Richards2D model with base parameters at time $t = 8$ h and single drip emitter placed on the left.

the results shown in Figure II.13. This result corroborates the results of Dixon and Afewu (2011). Figure II.14 shows the results after $t = 8$ h of simulation where the single drip emitter was placed at the top left corner of the domain. Notice the higher saturation levels in elements near the emitter, since there is no force pulling the extra moisture to the left.

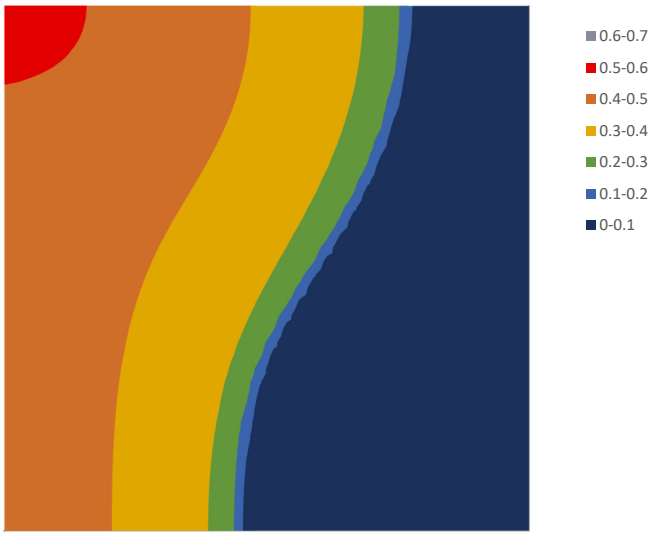

Figure II.15: The effect of a highly conductive channel on the saturation profile.

3. Channelling effect. A non-uniform packing can be modelled as with the one-dimensional case by varying saturated conductivity. In particular, a draining channel can be simulated as a stack of elements with high conductivities on vertical boundaries. Figure II.15 shows the result with a channel of highly conductive (with $K_s = 1\ \mathrm{m} \cdot \mathrm{s}^{-1}$) vertical boundaries for elements $(4, 10)$–$(4, 40)$. This channel draws the liquid straight down, preventing water spread in a lateral direction (compare with Figure II.14).

4. Barrier. Consider placing a horizontal barrier in the packing, but providing space on either side of the barrier. Figure II.16 shows the saturation distribution where the barrier was put at $z = 0.25$ m and from $x = 0.2$ m to $x = 0.8$ m with hydraulic conductivity $K_s = 10^{-7}\ \mathrm{m} \cdot \mathrm{s}^{-1}$. After 8 hours the lateral moisture spread below the barrier is hindered. A similar effect is seen if the barrier has a narrow hole. In this case the domain under the hole behaves as if there was a single drip emitter in this position (Figure II.17).

5. Modelling of the experiment by Wu et al. (2007). Wu et al. (2007) observed that a column packed with fine and coarse material had preferential liquid flow in the fine part of the packing under low flow rates. The domain was partitioned vertically in half. The left half represented fine packing and the right half — coarse packing. The model was run with the parameters listed in Table II.5 and with

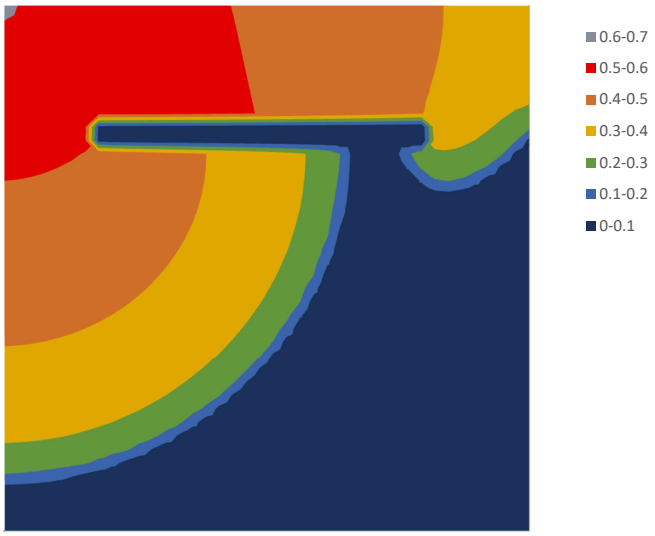

Figure II.16: The effect of an impermeable barrier in the domain on the saturation profile.

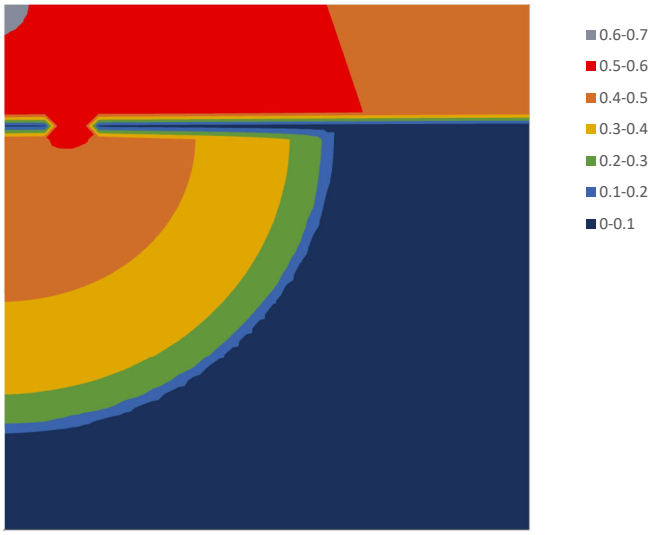

Figure II.17: Richards2D model results with impermeable barrier with a single narrow opening in it.

Table II.5

Parameter	Values	Units	Comment
General parameters			
Height	1	m	
Width	1	m	
Inlet flow rate	5	$\mathrm{L \cdot m^2 \cdot h^{-1}}$	Average flow rate
Initial saturation	0.01	–	
Water content range	0.35	–	$\Delta\vartheta = \vartheta_s - \vartheta_r$
Coarse side			
α	3	$\mathrm{m^{-1}}$	
n	1.3	–	
m	0.231	–	$m = 1 - 1/n$
K_s	0.1	$\mathrm{m \cdot s^{-1}}$	
Fine side			
α	1.5	$\mathrm{m^{-1}}$	
n	1.2	–	
m	0.167	–	$m = 1 - 1/n$
K_s	0.05	$\mathrm{m \cdot s^{-1}}$	

a single drip emitter located on the coarse die of the ore close to the centre (horizontal index 25 out of 40). The progression of saturation distribution for 48 hours is shown in Figure II.18. It is evident that the fine side accumulates more moisture. Furthermore, after 48 hours the outflow on the fine side was about three times higher compared to the coarse side: $7.8\ \mathrm{L \cdot m^{-2} \cdot h^{-1}}$ versus $2.5\ \mathrm{L \cdot m^{-2} \cdot h^{-1}}$, qualitatively confirming the observations by Wu et al. (2007).

The hydraulic parameters that would deliver this result were chosen carefully. Due to the form of the relative hydraulic conductivity function $K_r(s)$, the only way to provide a higher flow in a part of the domain is to have a higher saturation. One extra consideration helped to choose the hydraulic parameters: if there are two small volumes of media (cells) in contact, it is likely that capillary pressure does not vary dramatically between them. Indeed, if there was a high gradient of pressure, it would cause the pull of liquid from one cell to another, equalising the pressure. Thus, for ball-park calculations their pressures can be assumed equal. Let cells 1 and 2 represent a coarse and fine ore with fixed hydraulic parameters respectively. Hydraulic parameters in cell 2 must be such that: $s_2 > s_1$, $h_2 = h_1$ and $K_2 > K_1$. The van Genuchten model leads to the following expression for the saturation in cell

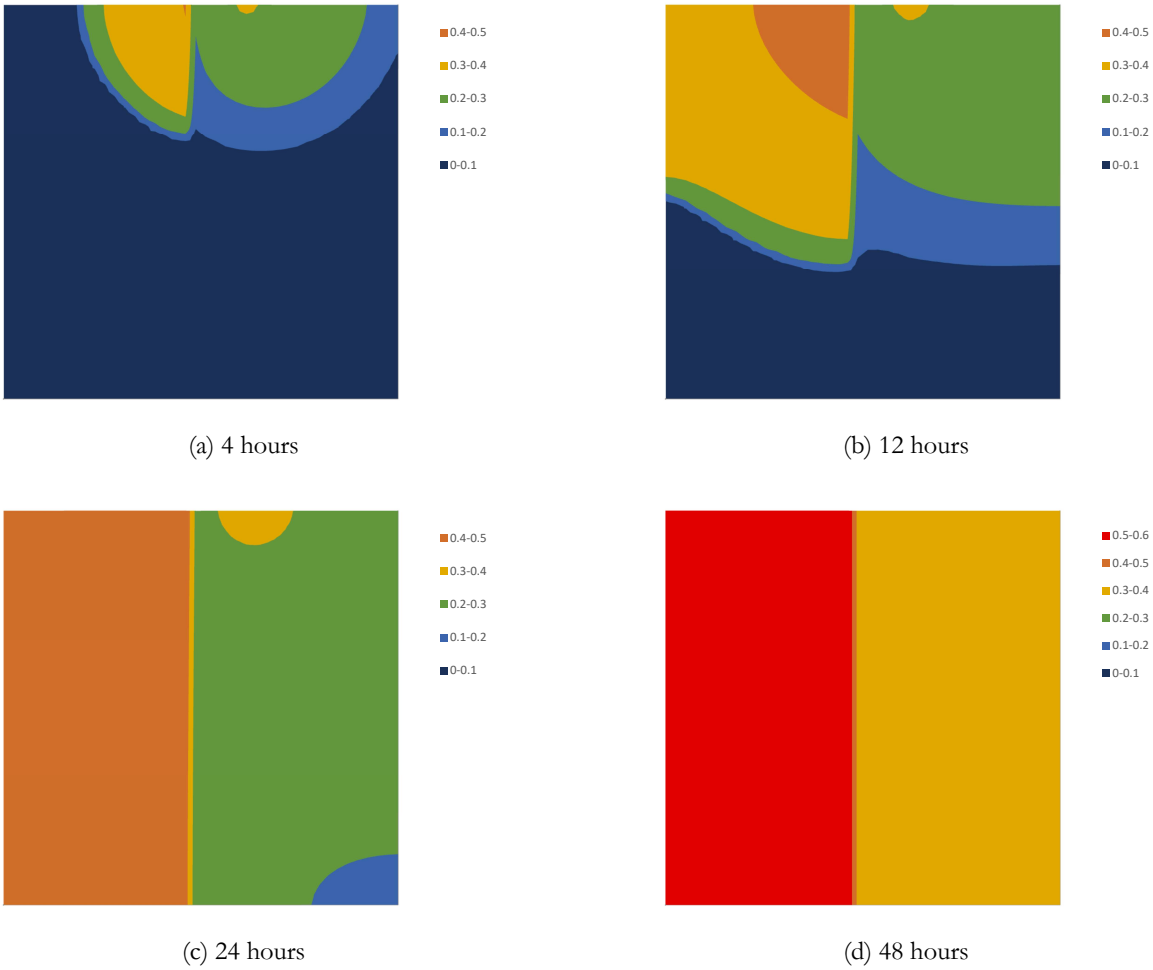

(a) 4 hours

(b) 12 hours

(c) 24 hours

(d) 48 hours

Figure II.18: Saturation distribution in a model following Wu et al. (2007) experiment.

2:

$$s_2 = \left[1 + \left(\frac{\alpha_2}{\alpha_1}\right)\left(s_1^{-1/m_1} - 1\right)^{n_2/n_1}\right]^{-m_2}.$$

Since $0 < m = 1 - 1/n < 1$, $n > 1$ and $\alpha > 0$ the following conditions must apply for $s_2 > s_1$: $\alpha_2 < \alpha_1$ and possibly $n_2 < n_1$. The first condition makes general sense since $\alpha_2 < \alpha_1$ implies that the air movement in cell 2 would occur at a lower partial pressure (or higher in absolute terms), i.e. only when the material is relatively drier. Due to smaller capillary channels in fine media, this is expected. The second result is non-intuitive as parameter n does not represent any particular physical property. Parameter n, however, cannot be too low: a smaller value of n leads to a lower hydraulic conductivity at a given saturation and thus may not achieve $K_2 > K_1$. Parameters in Table II.5 were chosen based on these considerations. However, there is no general consensus in the literature regarding the variance

of hydraulic parameters with coarser or finer ore.

§ 7. Advection-dispersion model of the solute transport

Dissolved solute is transported by moving liquid. However, it also participates in some mixing caused either by molecular diffusion or by mixing different elemental liquid "parcels" that take different paths in a porous medium. The mass balance equation describing this phenomena in a one-dimensional case for constant and uniform water content has the form:

$$\frac{\partial c}{\partial t} + v\frac{\partial c}{\partial z} - \frac{\partial}{\partial z}\left[D\frac{\partial c}{\partial z}\right] = 0,$$

where $v = V/\vartheta$ is advective velocity and D is a dispersion coefficient. In general, a dispersion coefficient is a function of flow rate v and the scale of domain (Dixon and Afewu, 2010). For the purpose of this work it will suffice to discuss the case when $D \equiv$ const.

The advection-dispersion equation can be simplified by introducing dimensionless time τ. There are two choices of time scale, either advection time with the scale parameter H/v or dispersion time with the scale parameter H^2/D, where H is the domain height. Choosing the former and introducing the Péclet number

$$\mathrm{Pe} = \frac{Hv}{D},$$

the advection-dispersion equation becomes

$$\frac{\partial c}{\partial \tau} + \frac{\partial c}{\partial \zeta} - \frac{1}{\mathrm{Pe}}\frac{\partial^2 c}{\partial \zeta^2} = 0,$$

where $\tau = (v/H)\ t$ and $\zeta = z/H$ are unitless time and length. Boundary conditions for this equation are:

$$c(\tau, 0) = 1,$$
$$\left.\frac{\partial c}{\partial \zeta}\right|_{\zeta=1} = 0,$$

stating known inlet concentration and free outflow. The analytical solution of the advection-dispersion equation requires the use of the Fourier series. However, since it is expected that $c(\tau, 0) \neq c(\tau, 1)$, the series convergence is slow. Thus, the use of this analytical solution is not practical. A simpler form of

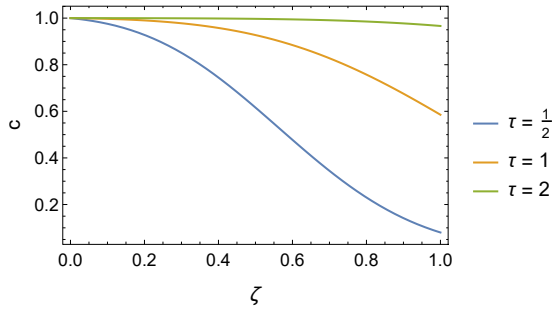

Figure II.19: Result from the approximated solution of the advection-dispersion equation.

the solution is possible on a semi-infinite domain. In this case the condition on the flux $\partial c/\partial\zeta|_{\zeta=1} = 0$ is replaced by the condition on the value $c(\tau, \zeta \to \infty) = 0$. The solution

$$\hat{c}(\tau,\zeta) = \frac{1}{2}\left(\operatorname{erfc}\left[\frac{\zeta-\tau}{2\sqrt{\frac{\tau}{\mathrm{Pe}}}}\right] + \exp\left[\mathrm{Pe}\,\zeta\right]\,\operatorname{erfc}\left[\frac{\zeta+\tau}{2\sqrt{\frac{\tau}{\mathrm{Pe}}}}\right]\right)$$

is close to the solution of the original problem if the free flow-boundary were further removed or, the same, if the Péclet number were very large (Ogata and Banks, 1961). However, in the case of typical flow rates and sizes for heap leaching, the Péclet number is actually closer to one. The result of the approximated solution with $\mathrm{Pe} = 1$ on the domain $\zeta \in [0, 1]$ at different time points is shown in Figure II.19. It is evident that $\partial c/\partial\zeta|_{\zeta=1} \neq 0$. The only possible alternative is to examine a numerical solution.

Numerical solution results for $\zeta = 1$ (outlet) and different Péclet numbers are shown in Figure II.20. Note the transition from a small Péclet number (instant mixing) to a large number. The time delay is due to plug-flow-type flow and the reduced effect of mixing. Systems with low flow rates are expected to have a Péclet number close to one, thus, showing a combination of some delay due to plug-flow and back mixing. $\mathrm{Pe} = 0.01$ refers to the mass transport governed almost exclusively by diffusion. The curve for this case looks almost as a unit step since the dimensionless time was introduced as an advection time: $\tau = 1$ refers to the time when the advection front reaches the end of the domain. In this case, however, the rate of dispersion is so much higher, that it causes the concentration to rise at the end of the domain way before the front reaches it. At another end of the spectrum lie high Péclet numbers, for which the transport is dominated by the advective flow, and at the limit $\mathrm{Pe} \to \infty$, the function $c(\tau)$ becomes a unit step at $\tau = 1$. It must be noted that the solute normalised concentration approaches unity in under two plug-flow times (τ) in all cases.

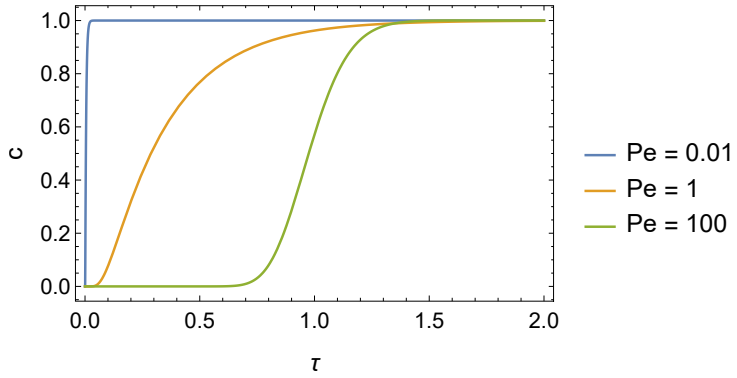

Figure II.20: Results of the numerical solution of the advection-dispersion equation at $\zeta = 1$ and different Péclet numbers.

§ 8. Simple compartment models

Compartment models are important tools in reactor design; they help to understand the modes of non-ideal flows in a reactor (Levenspiel, 1999). One serious drawback of these models is that they are not predictive and can only act as a diagnostic tool. In this section properties of some of compartment models that potentially can be applied to the heap leaching context are investigated (see section 6 of Chapter IV on how they are applied in the current study). But before compartment models are introduced it is worthwhile to have a quick review of their main building blocks: plug-flow and continuous stirred-tank reactors.

Plug-flow reactor. This reactor represents an ideal flow in the absence of mixing. Mathematically it is represented as a solution of a hyperbolic equation (in non-dimensional form):

$$\frac{\partial u}{\partial \tau} - \frac{\partial u}{\partial \zeta} = 0,$$

where u is a dimensionless reagent concentration, $\tau = (v/H)t$ is dimensionless time and $\zeta = z/H$ is a dimensionless position along the flow. One particular property of a hyperbolic equation is propagation of discontinuities. Thus, if the initial condition is

$$u_0(\zeta) = u(\tau = 0, \zeta) = \Theta(Z - \zeta),$$

where $\Theta(x)$ is the Heaviside step function and $0 < Z < 1$, the solution of the hyperbolic equation will be the moving discontinuity "front":

$$u(\tau, \zeta) = \Theta\left(Z + \tau - \zeta\right).$$

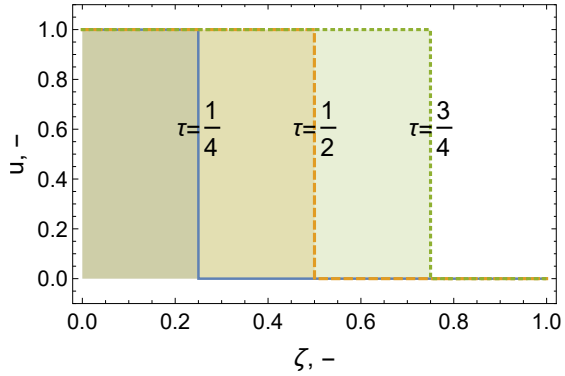

Figure II.21: Ideal plug-flow reactor concentration profile.

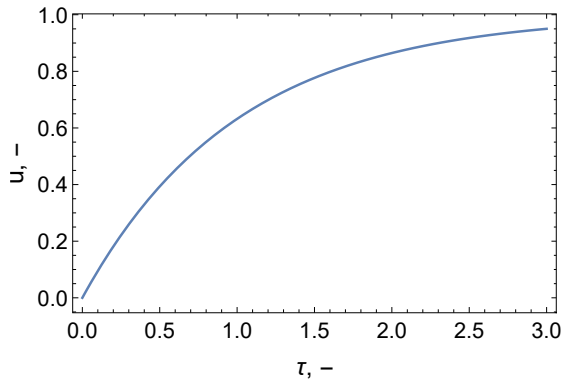

Figure II.22: Concentration over time from an ideal CSTR.

In residence time distribution (RTD) experiments with step change $Z = 0$. Notice, there are no parameters that this model depends on.

Continuous stirred-tank reactor (CSTR). Similar to a plug-flow reactor, CSTR represents an idealised flow but instead of assuming no back-mixing it assumes instantaneous mixing. A mathematical model representing the reactor with the step-change RTD exeriment is

$$\frac{\mathrm{d}u}{\mathrm{d}\tau} = 1 - u, \quad u(0) = 0$$

with the solution

$$u(\tau) = 1 - e^{-\tau}.$$

The time scale for a CSTR, however, is different from the time scale for a plug-flow reactor: here $\tau = (Q/\mathcal{V})t$, where Q is the volumetric flow rate and $\mathcal{V}$ is the reactor volume. Notice, as in the plug-flow reactor case, there are no parameters that this model depends on.

1. Two CSTRs in parallel (2-CTSR-P). This is a simple model representing input flow split between two CSTRs. Denote Q as total volumetric flow rate, Q_1 and Q_2as flow rates into each of the CSTRs ($Q_1+Q_2 = Q$), $\mathcal{V}$ as total reactor volume, and $\mathcal{V}_1$ and $\mathcal{V}_2$ as volumes of each of the CSTRs ($\mathcal{V}_1+\mathcal{V}_2 = \mathcal{V}$). The mass balance equations are

$$\mathcal{V}_1 \frac{\mathrm{d}u_1}{\mathrm{d}t} = Q_1 \left(u^* - u_1(t)\right),$$
$$\mathcal{V}_2 \frac{\mathrm{d}u_2}{\mathrm{d}t} = Q_2 \left(u^* - u_2(t)\right),$$

where u^* is inlet concentration. When non-dimensionalising u^* can be equated to one. However, keeping its value arbitrary will help to formulate a stacked 2CSTR-P model (Stacked-2CSTR-P). Using overall flow and volume to introduce dimensionless time

$$\tau = \frac{Q}{\mathcal{V}} t$$

and introducing parameters $q_1 = Q_1/Q$ and $\nu_1 = \mathcal{V}_1/\mathcal{V}$, the mass balance equations becomes:

$$\frac{\mathrm{d}u_1}{\mathrm{d}\tau} = \frac{q_1}{\nu_1} \left(u^* - u_1(\tau)\right),$$
$$\frac{\mathrm{d}u_2}{\mathrm{d}\tau} = \frac{1-q_1}{1-\nu_1} \left(u^* - u_2(\tau)\right).$$

Solutions of these equations with initial values $u_1(0) = u_2(0) = 0$ are

$$u_1(\tau) = u^* \left(1 - e^{-q_1\tau/\nu_1}\right),$$
$$u_2(\tau) = u^* \left(1 - e^{-(1-q_1)\tau/(1-\nu_1)}\right).$$

The measurable quantity is the combined outflow from both reactors:

$$u(\tau) = u^* \left(1 - q_1 e^{-\frac{q_1}{\nu_1}\tau} - (1-q_1)\, e^{-\frac{1-q_1}{1-\nu_1}\tau}\right). \tag{II.26}$$

A comparison of the CSTR and 2-CSTR-P models is shown in Figure II.23. Note, a single CSTR can be modelled as 2-CSTR-P with $q_1 = \nu_1 = 1/2$.

2. CSTR-dead volume reactor. A variation of a 2-CSTR-P reactor is the reactor where the flow goes through the first volume exclusively, but it is connected to the second well-mixed volume with mass transfer between the two. The governing equations are as follows:

$$\frac{\mathrm{d}u_1}{\mathrm{d}\tau} = \frac{1}{\nu_1} \left(1 - u_1(\tau)\right) - \frac{\kappa}{\nu_1} \left(u_1(\tau) - u_2(\tau)\right),$$
$$\frac{\mathrm{d}u_2}{\mathrm{d}\tau} = \frac{\kappa}{1-\nu_1} \left(u_1(\tau) - u_2(\tau)\right),$$

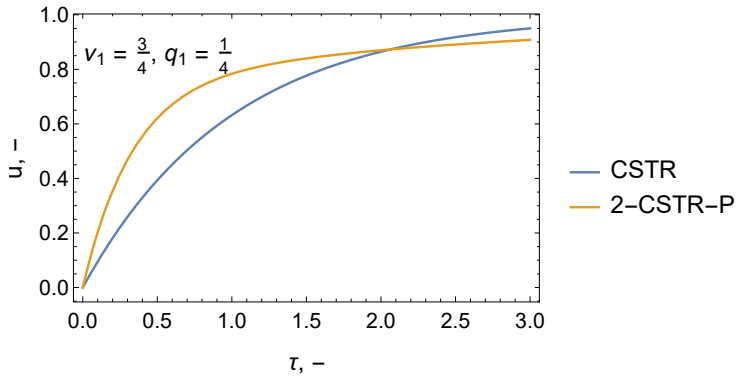

Figure II.23: Comparison of a single CSTR model and 2-CSTR-P.

where $\nu_1 = \mathcal{V}_1/\mathcal{V}$ as before and $\kappa = k/Q$ and k is a mass transfer coefficient of mass exchange between the volumes. An analytical solution of these equations is quite complex due to their coupling. However, it has the same structure as the solution of 2-CSTR-P: the output concentration (in this case just u_1 as there is no outflow from the second volume) has the following form:

$$u_1(\tau) = 1 - A\exp(-\alpha\tau) - (1 - A)\exp(-\beta\tau),$$

where A, α and β are functions of ν_1 and κ (not shown here for simplicity). Therefore, with the right choice of constants ν_1 and κ, A, α and β can be made to take the same values as the corresponding coefficients in (II.26). Thus, this model is mathematically indistinguishable from 2-CSTR-P and, besides demonstrating the equivalence with 2-CSTR-P, it will not considered any further.

3. Multiple CSTR in series (N-CSTR-S). This reactor can be viewed as a discretisation of a plug-flow reactor: when the number of reactors tends to infinity, this model converges to a plug-flow reactor. However, it is interesting on its own as it combines advective flow with some local back-mixing, yet its results are different compared to ADM with a small Péclet number (Figure II.24). The reason for this that in each CSTR back-mixing is contained by the boundaries of this CSTR, whereas in ADM with Pe $<<$ 1 dispersion causes back-mixing that can span over the whole domain. The only model parameter for N-CSTR-S is the number of the reactors. The concentration after N reactors is defined by the following expression (Levenspiel, 1999):

$$u(\tau) = 1 - \left(\sum_{n=0}^{N-1} \frac{(N\tau)^n}{n!}\right) e^{-N\tau}.$$

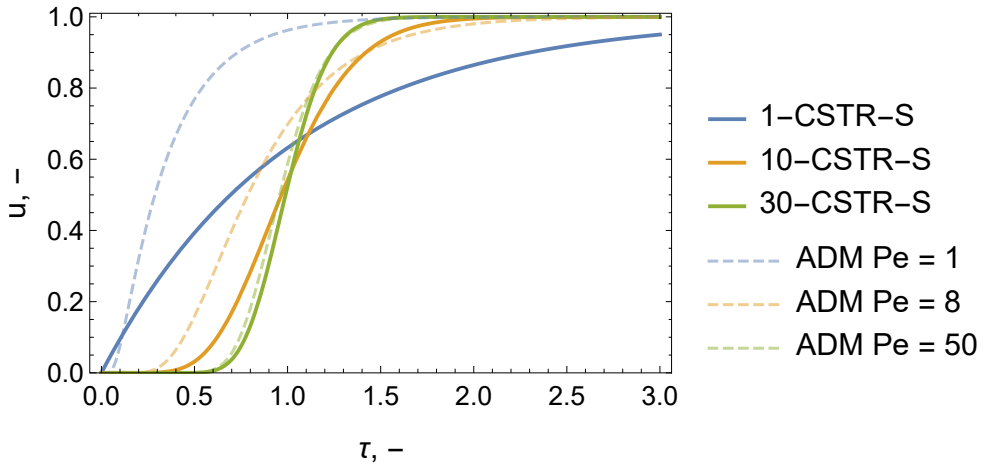

Figure II.24: Comparison of N-CSTR-S and ADM for various number of CSTRs and Péclet numbers respectively.

4. Stacked two CSTR in parallel (Stacked-2CSTR-P). N-CSTR-S can be viewed as an extension of a single CSTR representing a taller column. Similarly, 2-CSTR-P can be extended by stacking one 2-CSTR-P on the top of another. The flows after one 2-CSTR-P are merged before the flow splits again, thus, providing some mixing between different levels of the stack. Mathematically this model is represented by a set of differential equations

$$
\begin{aligned}
\frac{\mathrm{d}u_{1,1}}{\mathrm{d}\tau} &= \frac{q_1}{\nu_1}\left(u^* - u_{1,1}(\tau)\right), \\
\frac{\mathrm{d}u_{1,2}}{\mathrm{d}\tau} &= \frac{1-q_1}{1-\nu_1}\left(u^* - u_{1,2}(\tau)\right), \\
\frac{\mathrm{d}u_{2,1}}{\mathrm{d}\tau} &= \frac{q_1}{\nu_1}\left(u_1(\tau) - u_{2,1}(\tau)\right), \\
\frac{\mathrm{d}u_{2,2}}{\mathrm{d}\tau} &= \frac{1-q_1}{1-\nu_1}\left(u_1(\tau) - u_{1,2}(\tau)\right), \\
&\vdots \\
\frac{\mathrm{d}u_{N,1}}{\mathrm{d}\tau} &= \frac{q_1}{\nu_1}\left(u_{N-1}(\tau) - u_{N,1}(\tau)\right), \\
\frac{\mathrm{d}u_{N,2}}{\mathrm{d}\tau} &= \frac{1-q_1}{1-\nu_1}\left(u_{N-1}(\tau) - u_{1,2}(\tau)\right),
\end{aligned}
$$

where $u_{i,j}$ is the concentration at $i = 1, \ldots, N$ level in $j = 1, 2$ volume and $u_i(\tau)$ is the combined concentration after level i:

$$u_i(\tau) = q_1 u_{i,1}(\tau) + (1 - q_1)\, u_{i,2}(\tau).$$

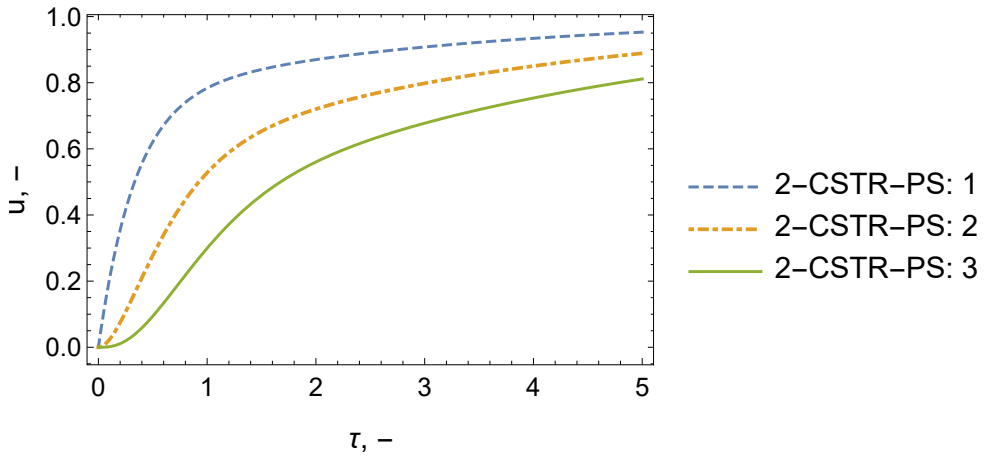

Figure II.25: Concentration outputs from levels 1 to 3 of the Stacked-2CSTR-P model with $\nu_1 = 3/4$ and $q_1 = 1/4$.

While a fully analytical solution of these equations is possible, the resulting form is too complicated for any meaningful analysis. Thus, the analytical solution is obtained using *Mathematica* but the result is treated as a black-box function. The results for $i = 1, 2, 3$ are shown in Figure II.25. With the increase of i (a) the slope of the curve becomes shallower and (b) initial delay to the concentration rise starts forming. The latter signifies the appearance of plug-flow component in the flow.

§ 9. Plug-flow reactors in parallel (PFRP)

1. Rationale and description. Let's assume there is a reactor of volume $\mathcal{V}$ which operates at the steady-state flow rate Q. Residence time distribution (RTD) studies on this reactor resulted in $E(t)$ and $F(t)$ curves (Levenspiel, 1999) with the following relations

$$F(t) = \int_0^t E(p)\,\mathrm{d}p \quad \text{and} \quad \int_0^\infty E(p)\,\mathrm{d}p = 1.$$

As infinite time is not realisable in practice, $E(t)$ can be assumed to be finite, i.e. $E(t) \equiv 0$ for $t > T$. The time interval $[0, T]$ can be partitioned to N equal subintervals of size $\Delta t = T/N$: $0 = t_0 < t_1 < \cdots < t_N = T$. Denote

$$q_i = \int_{t_{i-1}}^{t_i} E(p)\,\mathrm{d}p,\ i = 1, \ldots, N \tag{II.27}$$

a portion of the flow with residence time between t_{i-1} and t_i. Since

$$1 = \int_0^T E(p)\,\mathrm{d}p = \sum_{i=1}^{N} \int_{t_{i-1}}^{t_i} E(p)\,\mathrm{d}p$$

it follows that

$$\sum_{i=1}^{N} q_i = 1.$$

The mean-value theorem applied to the expression of q_i results in

$$q_i = E_i \Delta t,$$

where $E_i = E\left(\hat{t}_i\right)$ and $\hat{t}_i \in [t_{i-1}, t_i]$. Instead of $E(t)$ let's consider function

$$\tilde{E}(t) = \sum_{i=1}^{N} q_i \delta\left(t - \hat{t}_i\right).$$

It follows that

$$\tilde{F}(t) = \int_0^t E(p)\, \mathrm{d}p = \sum_{i=1}^{N} q_i \Theta\left(t - \hat{t}_i\right).$$

Functions $F(t)$ and $\tilde{F}(t)$ are connected: $F(t_i) = \tilde{F}(t_i)$, i.e. $\tilde{F}(t)$ is a step-wise approximation of $F(t)$. The exact position of $\hat{t}_i$ depends on the shape of $E(t)$, but it can be approximated by the midpoint of the interval $[t_{i-1}, t_i]$:

$$\hat{t}_i \approx t_i^c = \frac{t_{i-1} + t_i}{2}.$$

With this approximation

$$\tilde{F}(t) = \sum_{i=1}^{N} q_i \Theta\left(t - t_i^c\right)$$

and $F(t_i) = \tilde{F}(t_i)$ still holds.

Each contribution $\delta\left(t - t_i^c\right)$ in $\tilde{E}(t)$ and corresponding $\Theta\left(t - t_i^c\right)$ to $\tilde{F}(t)$ represents a single plug-flow reactor. Thus, the overall $\tilde{E}(t)$ is a combination of plug-flow reactors. More precisely, it is N plug-flow reactors with the i-th reactor having residence time t_i^c, all of them connected in parallel and the i-th reactor receiving q_i portion of the flow. While this statement seems self-evident, it is worth proving it. Namely, it is necessary to prove that the reactor of such configuration will have a $\tilde{E}(t)$ (or $\tilde{F}(t)$) curve close to the $E(t)$ ($F(t)$) curve of the original reactor. Furthermore, it must be established that the volume of all plug-flow reactors is the same as the volume of the original reactor. To establish both of these facts, we will require the convective velocity in all reactors to be the same $v \equiv$ const. If v is fixed, the i-th reactor has length

$$\mathscr{L}_i = v t_i^c = v \Delta t \left(i - \frac{1}{2}\right).$$

The equation describing the stepwise RTD experiment for the i-th reactor becomes

$$\frac{\partial c}{\partial t} + v\frac{\partial c}{\partial z} = 0$$
$$c(0, z) = \Theta(-z)$$

where the exit concentration is $c(t, \mathscr{L}_i)$. As the convective velocity is not known, non-dimensionalising the equation can help to express it via known quantities. Choose T and vT as constants to non-dimensionalise time and space variables:

$$t = T\tau,$$
$$z = vT\zeta.$$

With the new variables the equation becomes

$$\frac{\partial c}{\partial \tau} + \frac{\partial c}{\partial \zeta} = 0,$$
$$c(0, \zeta) = \Theta(-\zeta)$$

with exit concentration $c(\tau, \zeta_i)$ where ζ_i is found from

$$\mathscr{L}_i = v\frac{T}{N}\left(i - \frac{1}{2}\right) = vT\zeta_i,$$

i.e.

$$\zeta_i = \frac{i - \frac{1}{2}}{N}.$$

The solution of this kind of equation is well known:

$$c(\tau, \zeta) = \Theta\left(\tau - \zeta\right).$$

Thus, the exit concentration is

$$c(\tau, \zeta_i) = \Theta\left(\tau - \frac{i - \frac{1}{2}}{N}\right).$$

In other words, it jumps from zero to one once the time reaches

$$\tau = \frac{i - \frac{1}{2}}{N} = \frac{t_i^c}{T},$$

i.e. the residence time of the plug-flow reactor. The combination of these solutions

$$c_{\text{overall}}(\tau) = \sum_{i=1}^{N} q_i c\left(\tau, \zeta_i\right) = \sum_{i=1}^{N} q_i \Theta\left(\tau - \frac{i - \frac{1}{2}}{N}\right)$$

provides the expression for the $\tilde{F}(\tau)$ curve of this reactor. It is trivial to check that it is identical to $\tilde{F}(t)$ derived above.

Note 1. The solution must be considered as a generalised solution since it contains a discontinuity. It should be noted that certain discontinuities are not permissible in generalised solutions (Strauss, 2008), but it can easily be shown that the discontinuity in the present case is of the allowed type.

Note 2. The same differential equation is used for all plug-flow reactors. The only difference is where the exit concentration is located, ζ_i. This property will be referred to the *upstream property*: it denotes the fact that at any point ζ in the plug-flow reactor the solution only depends on points $\tilde{\zeta} < \zeta$. This is in contrast to a diffusion problem where the dependency is on both sides. This fact will be used later for the case of this reactor with heterogeneous reaction.

The difference between the curves $\tilde{F}(t)$ and $F(t)$ can be made negligibly small by choosing large enough value of N. Formally, this means that L^2-norm of the difference $F - \tilde{F}$ tends to zero as $N \to \infty$:

$$\lim_{N\to\infty} \left\| F - \tilde{F} \right\|_2 = \lim_{N\to\infty} \sqrt{\int_0^T \left(F(p) - \tilde{F}(p) \right)^2 \mathrm{d}p} = 0.$$

The integral expression in this equation can represented as the following summation

$$\int_0^T \left(F(p) - \tilde{F}(p) \right)^2 \mathrm{d}p = \sum_{i=1}^{N} \int_{t_{i-1}}^{t_i} \left(F(p) - \sum_{j=1}^{i} q_j \Theta\left(p - t_j^c\right) \right)^2 \mathrm{d}p.$$

The integral on each subinterval (t_{i-1}, t_i) is split into two parts by the step function $\Theta(p - t_i^c)$:

$$\int_{t_{i-1}}^{t_i} \left(F(p) - \sum_{j=1}^{i} q_j \Theta\left(p - t_j^c\right) \right)^2 \mathrm{d}p = \int_{t_{i-1}}^{t_i^c} \left(F(p) - \sum_{j=1}^{i-1} q_j \right)^2 \mathrm{d}p + \int_{t_i^c}^{t_i} \left(F(p) - \sum_{j=1}^{i} q_j \right)^2 \mathrm{d}p.$$

Note, that by definition

$$\sum_{j=1}^{i} q_j \equiv F\left(t_i\right).$$

Furthermore, by requiring $F(t)$ to be Lipschitz continuous

$$\forall p, q\colon \ |F(p) - F(q)| < A\,|p - q|\,,$$

the integrals on subintervals (t_{i-1}, t_i^c) and (t_i^c, t_i) are bound above as follows:

$$\int_{t_{i-1}}^{t_i^c} \left(F(p) - \sum_{j=1}^{i-1} q_j \right)^2 \mathrm{d}p = \int_{t_{i-1}}^{t_i^c} \left(F(p) - F\left(t_{i-1}\right) \right)^2 \mathrm{d}p \qquad < \left(A\frac{\Delta t}{2} \right)^2 \frac{\Delta t}{2},$$

$$\int_{t_{i-1}}^{t_i^c} \left(F(p) - \sum_{j=1}^{i-1} q_j \right)^2 \mathrm{d}p = \int_{t_i^c}^{t_i} \left(F(p) - F\left(t_i\right) \right)^2 \mathrm{d}p \qquad < \left(A\frac{\Delta t}{2} \right)^2 \frac{\Delta t}{2}.$$

Thus,

$$\int_{t_{i-1}}^{t_i} \left(F(p) - \sum_{j=1}^{i} q_j \Theta\left(p - t_j^c\right) \right)^2 \mathrm{d}p < \frac{A^2}{4} \Delta t^3.$$

Finally, summing up these expressions over all the intervals and recalling that $\Delta t = T/N$, results in the following estimate:

$$\sqrt{\int_0^T \left(F(p) - \tilde{F}(p) \right)^2 \mathrm{d}p} < \frac{A}{2N} T^{3/2}.$$

Therefore, as $N \to \infty$ the difference becomes zero. The measure of difference between $F(t)$ and $\tilde{F}(t)$ can be introduced

$$\varepsilon_F = \left\| F - \tilde{F} \right\|_2 < \tilde{\varepsilon}_F = \frac{A}{2N} T^{3/2}, \tag{II.28}$$

where $\tilde{\varepsilon}_F$ is the estimate of this error.

Let's examine the reactor volume. The volume of the i-th plug-flow reactor can be found from its residence time

$$t_i^c = \Delta t \left(i - \frac{1}{2} \right) = \frac{\mathscr{V}_i}{Q_i} = \frac{\mathscr{V}_i}{q_i Q}.$$

Thus,

$$\mathscr{V}_i = q_i t_i^c Q.$$

On the other hand, the sum of all these volumes must add up to $\mathscr{V}$:

$$\sum_{i=1}^{N} \mathscr{V}_i = \sum_{i=1}^{N} q_i t_i^c Q = Q \left[\sum_{i=1}^{N} \hat{t}_i q_i + \sum_{i=1}^{N} \varepsilon_i q_i \right] = Q \left[\int_0^t pE(p)\, \mathrm{d}p + \sum_{i=1}^{N} \varepsilon_i q_i \right], \tag{II.29}$$

where $\varepsilon_i = t_i^c - \hat{t}_i$ and $\hat{t}_i \in [t_{i-1}, t_i]$ are the points for the mean-value theorem expression:

$$\hat{t}_i \int_{t_{i-1}}^{t_i} E(p)\, \mathrm{d}p = \int_{t_{i-1}}^{t_i} pE(p)\, \mathrm{d}p.$$

The integral expression on the RHS of (II.29) is the mean residence time of the reactor and, thus, equal to $\mathscr{V}/Q$. It follows

$$\sum_{i=1}^{N} \mathscr{V}_i = \mathscr{V} + Q \sum_{i=1}^{N} \varepsilon_i q_i.$$

The last term on the RHS is bounded by $Q\Delta t$ since $|\varepsilon_i| \leq \Delta t/2$ and $\sum_i q_i = 1$. Therefore,

$$\mathcal{V} = \sum_{i=1}^{N} \mathcal{V}_i + \mathcal{O}(\Delta t).$$

To summarise, it was shown that (a) plug-flow reactors in parallel indeed model the $\tilde{F}(t)$ curve described above and (b) their total volume differs from the volume of the original reactor only by $\mathcal{O}(\Delta t)$ and becomes insignificant as $\Delta t \to 0$.

The importance of this model can be illustrated by the following example. Let $F(t)$ to represent a single CSTR

$$F(t) = 1 - \exp\left[-\frac{Q}{\mathcal{V}}t\right].$$

$F(t)$ becomes insignificantly different from 1 for some large time T. For example, when $(Q/\mathcal{V})t = 10$, $F(t)$ differs from one only by 4.540×10^{-5}. As shown above, using a time discretisation procedure, $F(t)$ can be approximated very closely by $\tilde{F}(t)$ with N plug-flow reactors in parallel. The difference between $F(t)$ and $\tilde{F}(t)$ can be made below any chosen threshold ε by choosing N as follows (see equation (II.28)):

$$N = \left\lceil \frac{A}{2\varepsilon} T^{3/2} \right\rceil,$$

where the brackets "$\lceil\,\rceil$" denote the smallest integer larger than the value inside them. Thus, there can be two reactor configurations that correspond to essentially one $F(t)$ curve. However, the difference between the two configurations becomes significant once a reaction is added.

Let's assume the reagent c undergoes some chemical reaction with the mineral present in the reactor. The reaction rate, in units compatible with c, is described by a non-linear function $f(c, X)$ where X is mineral conversion. In the case of a single CSTR, the process is described by the equations

$$\frac{\mathrm{d}c}{\mathrm{d}t} = \frac{Q}{\mathcal{V}}(c_0 - c) - f(c, X),$$
$$\frac{\mathrm{d}X}{\mathrm{d}t} = \alpha f(c, X),$$

where c_0 is reagent inlet concentration, which is assumed $c_0 = 1$ further below, and α is the coefficient taking care of rectifying units between c and X and taking care of stoichiometry. The non-dimensionalisation of time using top-time T results in

$$\frac{\mathrm{d}c}{\mathrm{d}t} = \frac{QT}{\mathcal{V}}(c_0 - c) - Tf(c, X), \tag{II.30}$$
$$\frac{\mathrm{d}X}{\mathrm{d}t} = \alpha T f(c, X). \tag{II.31}$$

In the case of plug-flow reactors in parallel, the equations for the i-th reactor are

$$\frac{\partial c_i}{\partial \tau} + \frac{\partial c_i}{\partial \zeta} = -Tf(c_i, X_i), \tag{II.32}$$

$$\frac{\partial X_i}{\partial \tau} = \alpha T f(c, X_i) \tag{II.33}$$

with initial condition $c_i(0, \zeta) = X_i(0, \zeta) = 0$ and boundary condition $c_i(\tau, 0) = 1$. Exit concentration, as before, is taken at $\zeta = \zeta_i$. If parameter α is independent of i, i.e. it is the same for all plug-flow reactors, meaning that it is assumed that the ratio of liquid to solids is the same between all of them, the above equations are the same for all reactors and the only difference is where to "sample" the exit concentration.

A usual way to solve first order partial differential equations is to use the method of characteristics (Strauss, 2008). However, in this case it would lead to the set of delayed ODEs since there is no convective flow for X_i. Thus, a direct finite-differences scheme is proposed to solve these equations.

2. Numerical scheme. Equation II.32 is of the hyperbolic type, i.e. it admits discontinuous solutions (Strauss, 2008). Capturing the discontinuity in a numerical method is not an easy task. However, the main focus of the numerical method is to produce an accurate solution for the combined problem II.32 and II.33. In this case, consumption due to reaction smooths discontinuity introduced by the step-wise change in concentration. Considering this is just a one-dimensional problem the following method was used to solve the equations:

- The spatial coordinate was discretised using the Finite-Differences (FD) method: for $\zeta \in [0, Z]$, a uniform mesh $\zeta_0 = 0 < \zeta_1 < \cdots < \zeta_N = Z$ is introduced.
- The convective derivative was stabilised using upstream finite-difference. To minimise numerical diffusivity introduced by the discretisation, three upstream points were used to achieve a second-order approximation (except for the first point ζ_1 where there is not enough information for the second order approximation, in which case a simple linear two-point approximation was used).
- The time derivative was discretised using the Crank-Nicolson method.
- The resulting algebraic equations for each time-step were iteratively solved using a linear approximation (Newton-Raphson method).

- Finally, the linear equations from the Newton-Raphson method were solved using the Gauss-Seidel stationary iterative solver. No multi-grid method was necessary at this point as previous time-step values provided a good initial approximation for the Newton-Raphson method, which in turn provided its own approximation as a starting point for the Gauss-Seidel solver.

The rest of this section describes the method in more detail.

Denoting the spatial step as h, the second order approximation of the first derivative using three upstream points has the form:

$$f'(x_n) = f'_n = \frac{1}{2h}\left(f_{n-2} - 4f_{n-1} + 3f_n\right),$$

which can be easily checked using Taylor expansion. Using k as a time step, $r = k/h$ and $c(t_j, \zeta_i) = c_{i,j}$, where counter i refers to spatial resolution and counter j to temporal resolution, the discretised equations II.32 and II.33 have the form:

$$\begin{aligned}
c_{o,j+1} &= 1,\\
X_{0,j+1} - X_{0,j} &= \frac{\alpha k f_{0,j+1}}{2} + \frac{\alpha k f_{0,j}}{2},\\
c_{1,j+1} - c_{1,j} + \frac{r}{2}\left(c_{1,j+1} - c_{0,j+1}\right) + \frac{r}{2}\left(c_{1,j} - c_{0,j}\right) &= -\frac{k f_{1,j+1}}{2} - \frac{k f_{1,j}}{2},\\
X_{1,j+1} - X_{1,j} &= \frac{\alpha k f_{1,j+1}}{2} + \frac{\alpha k f_{1,j}}{2},\\
i &= 2, \ldots, N:\\
c_{i,j+1} - c_{i,j} + \frac{r}{4}\left(c_{i-2,j+1} - 4c_{i-1,j+1} + 3c_{i,j+1}\right)&\\
+ \frac{r}{4}\left(c_{i-2,j} - 4c_{i-1,j} + 3c_{i,j}\right) &= -\frac{k f_{i,j+1}}{2} - \frac{k f_{i,j}}{2},\\
X_{i,j+1} - X_{i,j} &= \frac{\alpha k f_{i,j+1}}{2} + \frac{\alpha k f_{i,j}}{2}.
\end{aligned}$$

These are the equations on $[c_{0,j+1}, X_{0,j+1}, \ldots, c_{N,j+1}, X_{N,j+1}]$ with values at time-step t_j being considered as known. To simplify further notation, which will require two additional indices for the Newtion-Raphson and Gauss-Seidel iterations, denote all values at the time-step t_j with a hat: $c_{i,j} = \hat{c}_i$,$X_{i,j} = \hat{X}_i$ and $f_{i,j} = \hat{f}_i$ and move them to the RHS. Furthermore, denote $\hat{b}_{c,i}$ and $\hat{b}_{X,i}$ parts of the RHS that are completely defined by known values from time-step t_j for c_i and for X_i equations

respectively. In this simplified notation, equations take the following form:

$$\begin{aligned}
c_0 &= 1 \\
X_0 - \frac{\alpha k f_0}{2} &= \hat{b}_{X,0} \\
c_1 + \frac{r}{2}\left(c_1 - c_0\right) + \frac{k f_1}{2} &= \hat{b}_{c,1} \\
X_1 - \frac{\alpha k f_1}{2} &= \hat{b}_{X,1} \\
& i = 2, \ldots N \\
c_i + \frac{r}{4}\left(c_{i-2} - 4c_{i-1} + 3c_i\right) + \frac{k f_i}{2} &= \hat{b}_{c,i} \\
X_i - \frac{\alpha k f_i}{2} &= \hat{b}_{X,i}
\end{aligned}$$

These equations are solved by iteratively improving approximations c_i^m and X_i^m, $m = 1, 2, \ldots$, starting from the known values $c_i^0 = \hat{c}_i$ and $X_i^0 = \hat{X}_i$. Consecutive approximations c_i^m and X_i^m are obtained as the solutions of the linear equations resulting from the linearisation of $f(c, X)$:

$$f_i^{m+1} = f\left(c_i^{m+1}, X_i^{m+1}\right) \approx f_i^m + \left(\frac{\partial f}{\partial c}\right)_i^m \left(c_i^{m+1} - c_i^m\right) + \left(\frac{\partial f}{\partial X}\right)_i^m \left(X_i^{m+1} - X_i^m\right).$$

Denoting $f_c = \partial f / \partial c$, $f_X = \partial f / \partial X$ and

$$\Phi_i^m = f_i^m + f_{c,i}^m c_i^m + f_{X,i}^m X_i^m,$$

the resulting linear equations on c_i^{m+1} and X_i^{m+1} are

$$\begin{aligned}
c_0^{m+1} &= 1 \\
\left(1 - \frac{\alpha k f_{X,0}^m}{2}\right) X_0^{m+1} - \frac{\alpha k f_{c,0}^m}{2} c_0^{m+1} &= \hat{b}_{X,0} + \frac{\alpha k}{2}\Phi_0^m \\
-\frac{r}{2} c_0^{m+1} + \left(1 + \frac{r}{2} + \frac{k f_{c,1}^m}{2}\right) c_1^{m+1} + \frac{k f_{X,1}^m}{2} X_1^{m+1} &= \hat{b}_{c,1} - \frac{k}{2}\Phi_1^m \\
\left(1 - \frac{\alpha k f_{X,1}^m}{2}\right) X_1^{m+1} - \frac{\alpha k f_{c,1}^m}{2} c_1^{m+1} &= \hat{b}_{X,1} + \frac{\alpha k}{2}\Phi_1^m \\
& i = 2, \ldots, N \\
\frac{r}{4} c_{i-2}^{m+1} - r c_{i-1}^{m+1} + \left(1 + \frac{3r}{4} + \frac{k f_{c,i}^m}{2}\right) c_i^{m+1} + \frac{k f_{X,i}^m}{2} X_i^{m+1} &= \hat{b}_{c,i} - \frac{k}{2}\Phi_i^m \\
\left(1 - \frac{\alpha k f_{X,i}^m}{2}\right) X_i^{m+1} - \frac{\alpha k f_{c,i}^m}{2} c_i^{m+1} &= \hat{b}_{X,i} + \frac{\alpha k}{2}\Phi_i^m
\end{aligned}$$

These linear equations have a banded sparse coefficient matrix. Iterative methods, such as Jacobi or Gauss-Seidel, are known to be effective for such matrices (Smith, 1985). According to these methods, solutions c_i^{m+1} and X_i^{m+1} are constructed iteratively starting from initial approximations $c_i^{m+1,0}$ and $X_i^{m+1,0}$. Then, given the approximations $c_i^{m+1,k}$ and $X_i^{m+1,k}$ and using the Gauss-Seidel method, the improved approximations $c_i^{m+1,k+1}$ and $X_i^{m+1,k+1}$ are obtained as follows:

$$
\begin{aligned}
c_0^{m+1,k+1} &= 1 \\
X_0^{m+1,k+1} &= \frac{1}{1-\frac{\alpha k f_{X,0}^m}{2}}\left(\hat{b}_{X,0} + \frac{\alpha k}{2}\Phi_0^m + \frac{\alpha k f_{c,0}^m}{2} c_0^{m+1,k+1}\right) \\
c_1^{m+1,k+1} &= \frac{1}{1+\frac{r}{2}+\frac{k f_{c,1}^m}{2}}\left(\hat{b}_{c,1} - \frac{k}{2}\Phi_1^m + \frac{r}{2} c_0^{m+1,k+1} - \frac{k f_{X,1}^m}{2} X_1^{m+1,k}\right) \\
X_1^{m+1,k+1} &= \frac{1}{1-\frac{\alpha k f_{X,1}^m}{2}}\left(\hat{b}_{X,1} + \frac{\alpha k}{2}\Phi_1^m + \frac{\alpha k f_{c,1}^m}{2} c_1^{m+1,k+1}\right)
\end{aligned}
$$

$i = 2, \ldots, N$:

$$
\begin{aligned}
c_i^{m+1,k+1} &= \frac{1}{1+\frac{3r}{4}+\frac{k f_{c,i}^m}{2}}\left(\hat{b}_{c,i} - \frac{k}{2}\Phi_i^m - \frac{r}{4} c_{i-2}^{m+1,k+1} + r c_{i-1}^{m+1,k+1} - \frac{k f_{X,i}^m}{2} X_i^{m+1,k}\right) \\
X_i^{m+1,k+1} &= \frac{1}{1-\frac{\alpha k f_{X,i}^m}{2}}\left(\hat{b}_{X,i} + \frac{\alpha k}{2}\Phi_i^m + \frac{\alpha k f_{c,i}^m}{2} c_i^{m+1,k+1}\right)
\end{aligned}
$$

Notice, the Gauss-Seidel method solves these equations nearly directly — the only unknown part is $X_i^{m+1,k}$ in the expression for $c_i^{m+1,k+1}$, $i = 1, \ldots, N$.

Second order approximation of the $\partial c/\partial\zeta$ term introduces some spurious oscillations near sharp changes in c. A common way to deal with them in case of FEM or FVM is to switch the convective flux term to a first order upstream approximation using flux limiters (Moukalled et al., 2016). Something similar is possible with FD as well. However, there is an easier way for this particular problem. The oscillations only occur near the wave-front. In case of a zero reaction rate, this means that for some i there are $c_{i-2} = 1$ and $c_{i-1} = c_i = 0$ (in reality, c_{i-2} will be a bit less than one and c_{i-1} will be slightly larger than zero due to numerical diffusion). Second order approximation of $\partial c_i/\partial\zeta$ becomes positive, indicating the flux from node i to $i-1$ (the upstream derivative is negative, indicating the flow from $i-1$ node to i). This, in turn, results in a negative c_i at the next time step as the corresponding equation becomes:

$$
c_i = \frac{1}{1+\frac{3r}{4}}\left(-\frac{r}{4} - \frac{r}{4}\right) < 0.
$$

Table II.6: Parameters for PFRP model simulation.

Parameter	Value	Comment
T	10	Time for which $F(T) \approx 1$ in numbers of residence times
$\Delta\tau$	0.02	F-curve discretisation time step as portion of T
h	1.25×10^{-3}	Plug-flow reactor spatial discretisation step
N	792	Number of spatial discretization points (and number of parallel reactors)
α	0.5	Reaction rate rectifying coefficient
β	2	Reaction order with respect to the reagent
ϕ	1.5	Reaction order with respect to the mineral
k_0	1	Base reaction rate; set to zero for non-reaction simulations
Tolerance	10^{-7}	Solver's error tolerance

The easiest way to correct this is to assign $c_i \leftarrow 0$ as it is obvious that the wave-front has not reached node i and the corresponding concentration must stay zero. Such an assignment, however, may cause mass balance discrepancy. It must be noted, that the FD scheme is fundamentally not locally mass conservative (compared to FVM). However, it guarantees the convergence of its solution to the solution of the original PDE (Smith, 1985). Furthermore, the issue with $c_i < 0$ only occurs if there is a discontinuity or a very sharp change in concentration, such as in an ideal plug-flow reactor without a reaction. This does not happen if there is a reaction that consumes the reagent as it makes the concentration gradient shallower at any given time. The interesting consequence of using FD is that the upstream property of the solution is completely preserved. In contrast, any approximation to the fluxes with an order higher than one would have involved values from downstream.

3. Model results For demonstration purposes, the PFRP model was compared to a single CSTR model (II.30) and (II.31): the F-curve of the latter acted as an input to assemble multiple plug-flow reactors by providing q_i values (see equation (II.27)). Two models were compared without and with heterogeneous reaction present. The no-reaction case demonstrated that PFRP is practically indistinguishable from true CSTR by means of RTD studies (Figure II.26). The reaction case demonstrated that despite similarities in reagent flow, these two models predict different kinds of leaching behaviour (Figure II.28). The model was run with the parameters listed in Table II.6. The ability of the model to control numerical diffusion and maintain stability is demonstrated by the concentration distribution plot through the plug-flow reactor at different times in absence of a reaction, Figure II.27.

The main idea behind the PFRP model is to show that a reactor that may look similar (or even

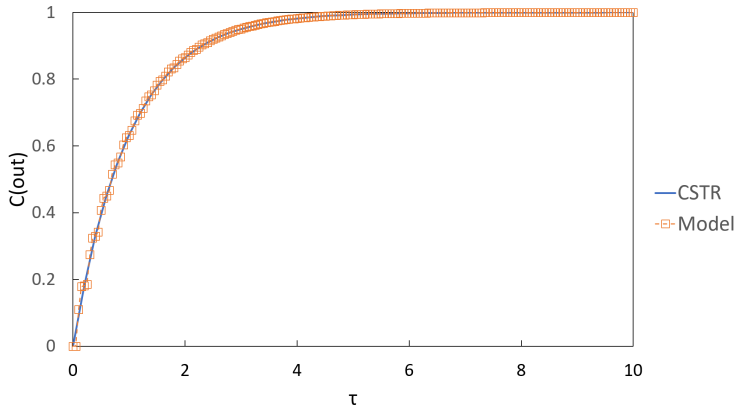

Figure II.26: CSTR and PFRP model comparison: no reaction.

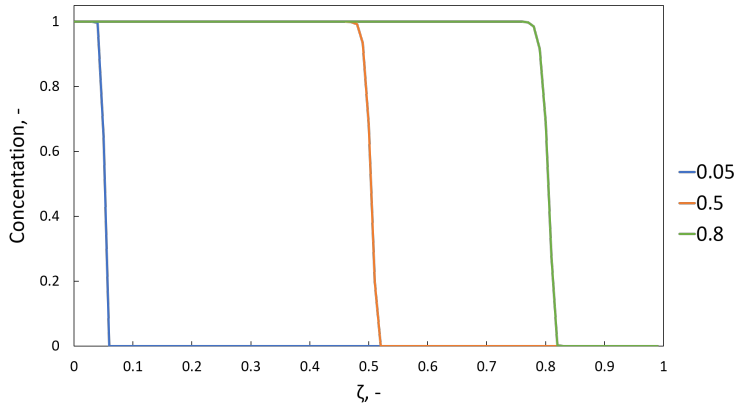

Figure II.27: Concentration inside the plug-flow reactor in absence of a reaction at different time points. The second order approximation together with fine mesh help to keep numerical diffusion to a minimum.

identical) to a CSTR in RTD studies may, in fact, exhibit very different behaviour if a heterogeneous reaction is considered with an unmovable solid matrix. Thus, it shows that one must be cautious when interpreting RTD curves.

§ 10. Summary

In the context of heap leaching, the central question is how to increase the operation efficiency. Due to the compound nature of heap leaching phenomena, they need to be decomposed into questions on the effects of:

- heap structure parameters,

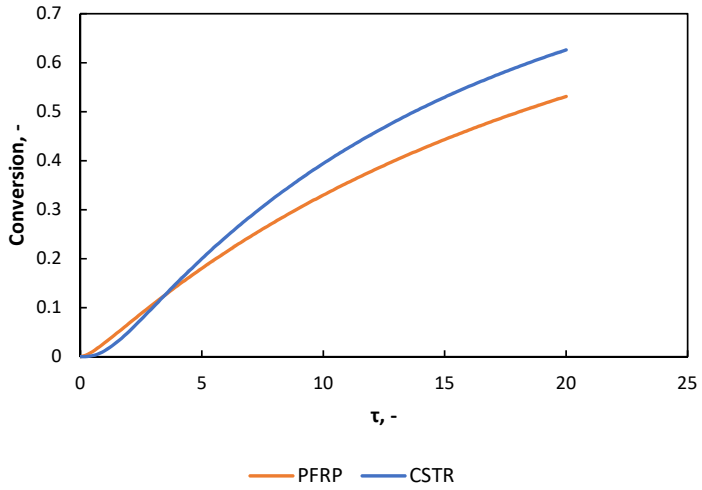

Figure II.28: Mineral conversion differences between CSTR and PFRP model run with the same parameters.

- solution composition, and
- inlet flow rate

on the distribution of saturation, flow, dispersion, etc. inside the heap. The current theory of the solution flow and the solute transport is expressed via models based on the Richards equation (I.1) and advection-dispersion equation (I.4). This chapter examined these models from various angles, simplifying or extending them where appropriate. Model formulation was done to set the scene for exploring the applicability of the models to heap leaching operations and experiments. Due to the overall lack of model validation in the literature, this project examines the effects of particle size distribution of the bed and the inlet flow rate on the saturation and solute transport. The experimental work was designed to provide the empirical base of such examination which is described in the next chapter.

Chapter III

Experimental materials and methods

Models alone cannot tell the full story. Experimental work performed for this project aimed to validate the models' conclusions, to find the relation between particle size distribution (PSD) and hydraulic material properties, and to advance the overall understanding of the flow through packed rock beds.

To study of the effect of PSD necessitated the use of artificial blends. The use of glass beads, sand or gravel was discarded as the particles comprising these materials tend to have shapes very different compared to ore. A discard ore from a gold mining operation was procured and artificial PSD blends were made using this ore. The flow was studied using packed columns. Steady-state liquid hold-up under various irrigation flow rates, liquid loss due to drainage, and flow dynamics through the bed were studied. This chapter provides a detailed description of the materials, apparatus and methods used.

§ 1. Materials

1. Ore. All the experimental work was conducted on an ore from the Witwatersrand area in South Africa. Since no leaching experiment was conducted, no mineralogy analysis was performed. About 2 t of run-of-mine ore sample was received and crushed to -26.5 mm size using a jaw crusher and screened into particle size fractions in the series: -1.4 mm, -5–$+1.4$ mm, -8–$+5$ mm, -13.2–$+8$ mm, -16–$+13.2$ mm, -19–$+16$ mm, and -26.5–$+19$ mm (Figure III.1). Although -1.4 mm fraction contains quite coarse, sand-size particles, it has a large portion of -0.1 mm particles (see the particle size distribution of this fraction in subsection 3.2 further below) and, thus, is referred to as fines.

Figure III.1: Cataloguing the weight fractions of the ore sample. Photo is courtesy of Bernard Oostendorp.

2. Solution composition. Tracer. Residence time distribution (RTD) studies were performed using potassium nitrate as a tracer. Tracer concentration in the outflow solution was established by a conductivity meter. Tap water was used as a base for the solution. A background (low) concentration of 0.03 $\text{mol} \cdot \text{L}^{-1}$ of potassium nitrate was added to the tap water to reduce the interference of any dissolved salts with tracer concentration measurements. For the RTD studies a 0.3 $\text{mol} \cdot \text{L}^{-1}$ (high) concentration of potassium nitrate was used. Since the potassium nitrate provides a favourable environment for algae growth, BIOCIDE was added to the solution in the proportion of 10 g per 20 L of the solution to prevent algae growth which might potentially clog pore channels in the bed.

§ 2. Apparatus

1. Columns. The experiments were conducted in four cylindrical PVC columns with the height of 30 cm and internal diameter of 20 cm, Figure III.2. A relatively large column diameter was chosen to reduce wall effects on the flow. The height of the column was restricted by the packed ore weight, since the columns were handled manually. The bottom of the column had a shallow conical shape with a single opening in the middle to draw the outflow solution. The columns were suspended on load cells. To reduce the interference of the feed and outflow tubing to the weight measurements, these

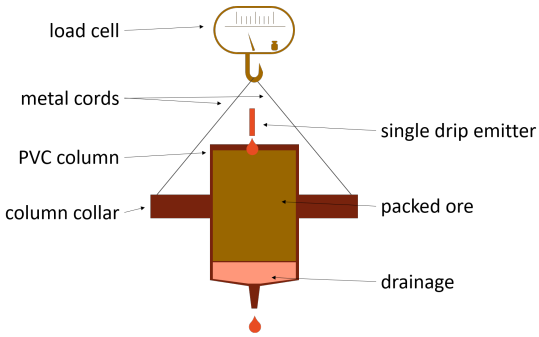

(a)

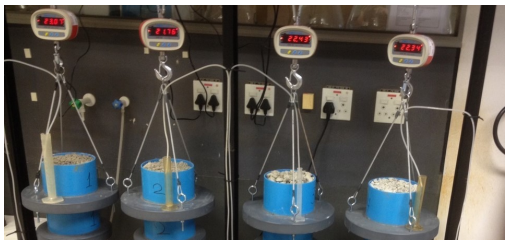

(b)

Figure III.2: Schematic drawing of the column and the picture of the reactor with four columns.

tubes were suspended independently from the column. The feeding solution was administered from the single port placed at the centre of the column. The top of the column was covered with plastic film (cling-film) to reduced evaporation. A single layer of glass beads was placed at the bottom of the column as a drainage layer. A circular metal mesh was placed above the outflow port to prevent its blockage.

2. Load cell. Each column weight was measured by a Adam Equipment SHS 50 load cell. This cell provides a weight resolution of ± 10 g and a maximum load of 50 kg. The packed column weight was in the range of 20–24 kg.

3. Pump. A peristaltic pump (MasterFlex L/S Cole-Parmer 7528-10) was used to provide the feed solution to the columns. Since four experiments ran in parallel, four channels of the pump were used. Prior to each experiment, the pump was calibrated. Each of the four channels may have had a slightly different flow rate due to different tubing placement or individual channel settings. After the calibration, actual flow rate for each channel was recorded and this value was used in the subsequent analysis (see Table III.1 for the actual values of flow rates).

4. Conductivity cell. Tracer concentration for the RTD studies was monitored using solution conductivity. To provide online measurements and to cope with low flow rates, a special conductivity cell was designed (Figures III.3 and III.4). Outflow solution was collected using a funnel-shaped opening A. From there the solution entered the main chamber B of cylindrical shape (25 mm diameter and 25 mm height). Two stainless steel electrodes mounted on a cap D were placed inside the chamber.

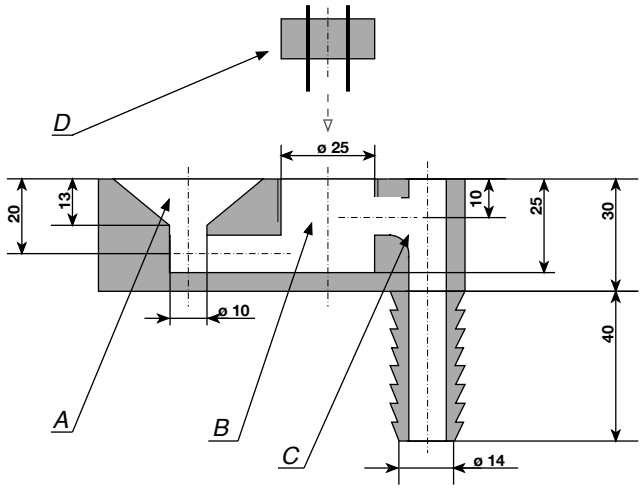

Figure III.3: Schematic of the conductivity cell: A is the funnel collecting the outflow solution from the column, B is a working chamber with electrodes, C is the outflow opening, and D is the cap with the electrodes that fits tightly into the chamber B with two electrodes mounted on to it.

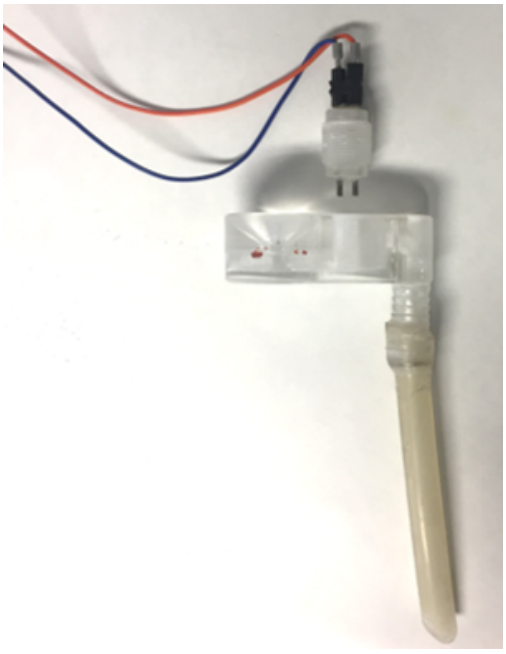

Figure III.4: The photographic picture of the conductivity cell.

The excess solution left the cell through outflow opening C. This design ensures that the main chamber is always filled with the solution.

5. Conductivity meter. An in-house conductivity meter was designed to work with the conductivity cells. The meter induces a sine-wave current between the electrodes and measures the voltage between

them. The voltage signal is digitised using a National Instruments board and sent to a computer where it is recorded.

§ 3. Methods

1. Particle size distributions. To investigate the effect of PSD on liquid flow, the ore fractions were used to create artificial blends with a predetermined PSD. Gates-Gaudin-Schumann (GGS) distribution was used to represent the PSD due to its simplicity (Dixon, 1992). The cumulative distribution function (CDF) for GGS distribution has the following form

$$\mathscr{P}(x) = \left(\frac{x}{\Xi}\right)^{\lambda},$$

where Ξ is the top size of the particles, λ is the distribution parameter and $\mathscr{P}(x)$ denotes the weight portion of particles with size less or equal to x. Since the ore was crushed to -26.5 mm, $\Xi = 26.5$ mm. This leaves a single parameter λ to provide the variation in PSD. Smaller values of λ correspond to distributions with a larger number of fines. Examples of CDF curves for GGS distributions with various values of λ are shown in Figure III.5. To cover the range of PSDs, the following values of λ were used to create the blends: 0.25, 0.4, 0.5, 0.6, 0.75, 0.97*, and 1.5. $\lambda = 0.25$ corresponds to about 48 wt% of -1.4 mm particles, whereas $\lambda = 1.5$ has virtually zero -1.4 mm particles. The blend with $\lambda = 0.97^*$ was constructed by using the weight fractions of $\lambda = 0.75$ but removing the fines fraction and subsequently re-scaling other fractions. The value of $\lambda = 0.97^*$ was found as the best fit to this PSD (Figure III.6).

To prepare the blend corresponding to each value of λ, the weight portion for each size fraction was determined using GGS CDF. For example for the fraction of -13.2–$+8$ mm particles, the weight portion is calculated as $\mathscr{P}(13.2) - \mathscr{P}(8)$. A 15 kg sample was prepared for each blend. The weight of the fraction is obtained by multiplication of 15 kg by the corresponding weight portion. Continuing the previous example, the weight of -13.2–$+8$ mm fraction is $15 \times (\mathscr{P}(13.2) - \mathscr{P}(8))$ kg.

2. Fines distribution. Since it was impractical to split -1.4 mm particles, the distribution of the fines was the same across the blends and only the quantity of the fines was varied. To properly account for the effect of the fines, a sample of -1.4 mm fraction was taken and subjected to sieve analysis to produce the distribution shown in Figure III.7.

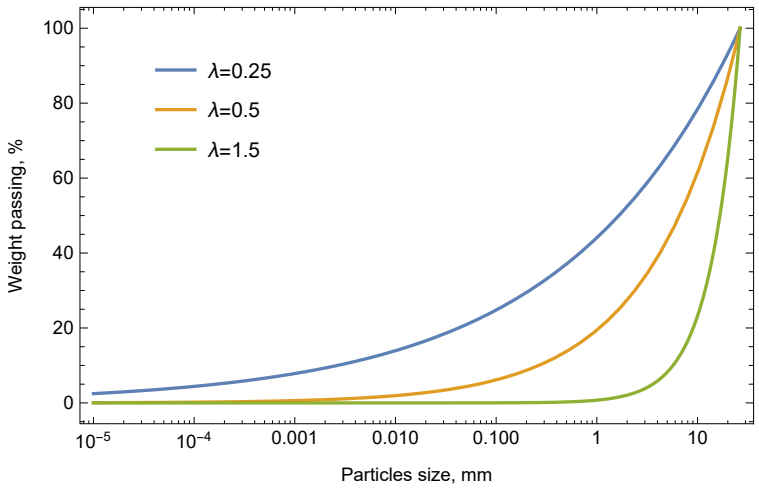

Figure III.5: Example of CDF curves of GGS distribution with various values of the parameter λ.

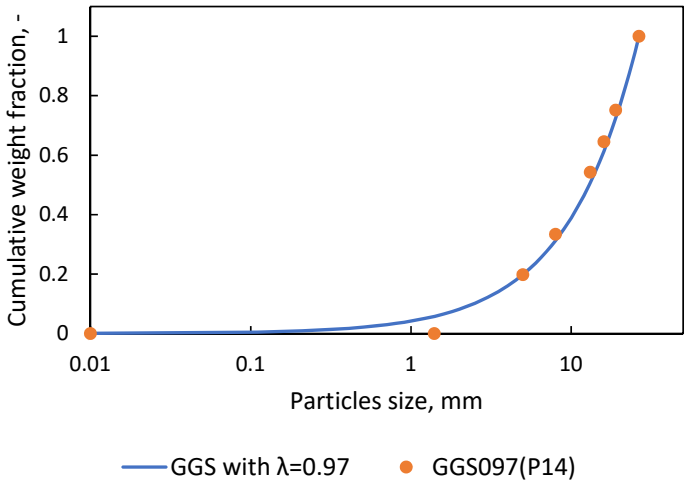

Figure III.6: CDF curves for true GGS distribution with $\lambda = 0.97$ and for GGS097(P14).

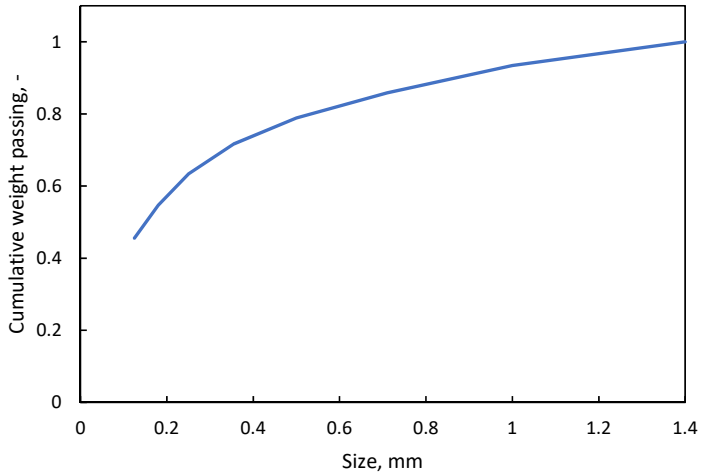

Figure III.7: PSD of -1.4 mm fraction of the sample.

3. Agglomeration. Packing of particles of various sizes into the column tend to result in their segregation throughout the column. To avoid this segregation, ore particles were agglomerated with either a strong acidic solution (2 g of sulphuric acid per 1 kg of ore, Tupikina et al., 2014) or tap water. As no advantage was found in using the acid, tap water was a preferred medium of agglomeration. The amount of liquid used depended on the amount of fines in the blend: the liquid was added incrementally until the lumps started forming. Blends with $\alpha = 0.97$ and $\alpha = 1.5$ were not agglomerated since they contained almost no fines.

4. Packing. After agglomeration the ore was transferred into the columns using a trowel. The ore loaded onto the trowel was placed into the column slightly off its centre in random directions to provide as uniform packing as possible.

5. Flooding and drainage. Preliminary work showed that performing the infiltration process on dry packed ore was impractical due to extremely long experiment duration. Therefore, it was decided to flood the columns before the start of the experiment to wet the surface of all the solids. Although flooding had possibly altered the packing (e.g. it may have caused the agglomerates to disintegrate), it was necessary for practical reasons.

Before the start of the experiments, the columns packed with ore were flooded by feeding the

solution at a 20 $L \cdot m^{-2} \cdot h^{-1}$ flow rate and blocking the outflow opening. The flooding was stopped once the solution covered the ore in the column. The flooded column weight was recorded. Significant slumping was observed for blends with a high fines content. Thus, the flooding was closely monitored to stop it at the right time to record the fully flooded weight. After flooding, the columns were gently drained by slightly opening the outflow port. The columns were allowed to drain for two days before the start of irrigation for gravimetric and RTD studies. The amount of slumping was recorded.

6. Infiltration studies. The dynamics of the infiltration after initial drainage was studied using the first set of columns (GGS075(P11)–GGS097(P14), see Table III.1 further below). The irrigation flow rate was set to 40 $L \cdot m^{-2} \cdot h^{-1}$ and the weight gain was monitored in short time intervals.

7. Steady-state gravimetric studies were set up to measure the liquid hold-up of the ore with different PSDs under various irrigation rates. A range of rates from 3 $L \cdot m^{-2} \cdot h^{-1}$ to 40 $L \cdot m^{-2} \cdot h^{-1}$ were used. The complete set of rates is shown in Table III.1. The following procedure was followed:

- Selected flow rates were used in increasing order, i.e. the experiment using 10 $L \cdot m^{-2} \cdot h^{-1}$ irrigation rate followed the experiment using 5 $L \cdot m^{-2} \cdot h^{-1}$ flow rate.
- Once the flow rate was set, the columns' weights were monitored. A new steady-state condition was considered to be reached if the column weight did not increase for 24 hours. The last weight was recorded as a new steady-state weight. Sometimes the column weight would start fluctuating with an amplitude of ± 10 g. In this case the time-average weight from the start of the fluctuation was taken as a new steady-state value.

8. Note on hysteresis. Although hysteresis is not the focus of these studies, no hydraulic research is complete without observing it. One set of four columns were subjected to increasing and decreasing sets of irrigation rates. The steady-state columns' weight was recorded at the same flow rates but with different previous rates: smaller and larger than the current rate respectively. Only blends GGS075(P11), GGS025(P12), GGS150(P13) and GGS097(P14) were used for hysteresis experiments (see Table III.1 for the blend descriptions). The weights were recorded at flow rates approximate to 10 $L \cdot m^{-2} \cdot h^{-1}$ and 20 $L \cdot m^{-2} \cdot h^{-1}$. These flow rates are "approximate" since the hysteresis experiment must be run uninterrupted on the decreasing set and, thus, it was not possible to calibrate the

pump. This, however, does not affect the results in a significant way as the hold-up is not sensitive to the flow rate change as will be shown in subsection 2.1 of Chapter IV.

9. Final drainage. After all the steady-state gravimetric and RTD experiments were completed (finishing at a flow rate close to 40 $\mathrm{L} \cdot \mathrm{m}^{-2} \cdot \mathrm{h}^{-1}$), the columns were drained for 48 hours. Their weights were recorded in short time intervals: 1 min at the start of the drainage and 15 min closer to the end. Due to the relatively short time of the drainage experiment it cannot be considered a complete drainage, but longer experiment times were not practical due to the coarse resolution of the load cells.

10. Intermittent infiltration studies. Intermittent flow experiments combined infiltration and drainage curves over a short period of time. The experiments were conducted on GGS075(P33) and GGS025(P34) columns (see Table III.1). No prior column flooding was performed resulting in "dry" infiltration. After the first run was completed, the columns were allowed to drain and the second run of the experiment was performed. This time, however, some moisture content was still present in the columns as complete drainage was not realistic to achieve. For each run the flow rate was set to about 8 $\mathrm{L} \cdot \mathrm{m}^{-2} \cdot \mathrm{h}^{-1}$ operating for one hour, switched off for the second hour and then repeating the cycle.

11. Conductivity meter calibration. Due to the use of tap water and variability of the temperature in the laboratory, the conductivity meter was calibrated before and after each experiment using this sequence of tracer concentrations: 0.03, 0.045, 0.06, 0.09, 0.12, 0.18 and 0.3 $\mathrm{mol} \cdot \mathrm{L}^{-1}$. The calibration solutions also contained BIOCIDE at the same concentration as the experimental solution, 10 g per 20 L. During the calibration, the voltage registered by the conductivity meter was recorded. The data from the calibration process was fitted into a curve

$$V = kC^{\beta},$$

where V is voltage, C is concentration in $\mathrm{mol} \cdot \mathrm{L}^{-1}$, and k and β are fitting parameters. The fit was performed using non-linear least squares implemented by the minimisation algorithm of the MS Excel's Solver tool. An example of the fitted curve is shown in Figure III.8. The details of calibration can be found in tables `RTD-calibration-measurements.csv` and `RTD-calibration-fit.csv` of Appendix C.

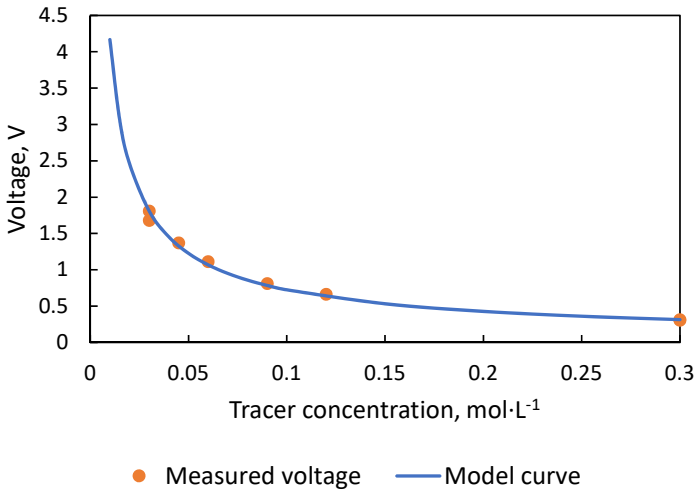

Figure III.8: An example of the conductivity meter calibration curve.

12. Residence time distribution (RTD) studies. For selected flow rates, steady-state gravimetric studies were followed by RTD experiments. The experiment was conducted in the following stages:

Preparation. For gravimetric studies the solution used for irrigation was recirculated. This, however, may have caused accumulation of electrolytes washed out from the ore. In preparation for RTD studies, the columns irrigation was switched to a fresh solution with low tracer concentration. No recirculation occurred until RTD studies were finished. The preparatory stage lasted until the conductivity meter reported a voltage in the outflow solution corresponding to the low tracer concentration. The irrigation flow rate was measured as it may have changed due to tube wearing in the pump (these flow rates are reported in Table III.1).

Step up. The feed was switched to the solution with the high tracer concentration. The concentration of the outflow solution was measured using the online conductivity meter. Once the outflow concentration matched the inlet tracer concentration, this stage was complete.

Step down. The feed was switched to the solution with the low tracer concentration. As in the step-up stage, the outlet concentration was measured until it became equal to the inlet concentration. At this point, the feed was switched to recirculation for the next gravimetric experiment.

The data was recorded as a voltage between the electrodes in the conductivity meter cell. These meas-

urements were converted to concentrations using conductivity meter calibration data. Finally, concentrations was linearly scaled to produce F-curves (Levenspiel, 1999).

13. Experimental matrix. Table III.1 summarises all the experiments that were performed. Each experiment is coded as "GGSxxx(Pyz)" where "xxx" denotes the value of GGS parameter λ (without a decimal point), "y" stands for the set of the experiments and "z" is the column number in the set. There were three sets of the experiments with four columns in each set. Distribution with $\lambda = 0.75$ is referred as "standard" since it has a moderate amount of fines and is close to PSDs typically used in heap leaching operations (Bouffard, 2003; Dixon and Afewu, 2010; Ghorbani et al., 2011). Due to its importance and "central" location among the PSDs, the experiments with this blend were repeated multiple times. When the experiments are compared, they are presented from coarser to finer PSD. Sometimes, however, it makes more sense to group the results by the set. In this case, for example, the range "GGS075(P11)–GGS097(P14)" includes GGS075(P11), GGS025(P12), GGS105(P13) and GGS097(P14).

Figure III.9 schematically demonstrates how the experimental procedure was carried out for each set (except for the blends GGS075(P33) and GGS025(P34)). First, the blends were prepared. This was followed by agglomeration and column packing. The columns were let to rest for 24 hours. The column flooding was started the following day. Once the complete flooding has occurred, the columns were drained for two days. After the drainage, irrigation with the first flow rate in series was started. It took between 3 and 7 days for the column weights to reach a steady state under low flow rates (below 40 $\mathrm{L \cdot m^{-2} \cdot h^{-1}}$), and between 7 and 10 days for high flow rates. Once the steady-state was reached, the column weight was taken and the irrigation was switched to a fresh feed with the low tracer concentration. The conductivity of the output was monitored, until it reached the expected value for this concentration. This usually took one day and was followed by the step-up RTD experiment which also lasted for about 24 hours (actual duration was dependent on the flow rate). Step-up experiment was followed by the step-down experiment. At the completion of the step-down experiment, the feed was switched to recirculation and the pump speed was changed to the next flow rate in series. The process of reaching the steady state, step-up and step-down RTD experiments was repeated for the new flow rate. Note, the RTD experiment was only conducted for some flow rates. Once the steady state weight at the highest flow rate in series was reached, the final drainage step commenced.

Table III.1: Overview of the experimental matrix.

Experiment code	GGS λ	Agglomerated with	wt% of -1.4 mm	Flow rates series, $L \cdot m^{-2} \cdot h^{-1}$	RTD flow rates, $L \cdot m^{-2} \cdot h^{-1}$
GGS150(P13)	1.5	Acid	1.2	2.4, 5.3, 7, 11.5, 20.1, 35.4, 42.7	N/A
GGS097(P14)	0.97*	Acid	0	2.4, 5.2, 7.1, 12.2, 20.7, 36.6, 42.8	2.9, 24.5
GGS075(P11)	0.75	Acid	11	3, 6.3, 8.4, 11.8, 20.5, 35.9, 43.5	26.1
GGS075(P21)	0.75	Water	11	3.3, 9.3, 40.2	3.5, 9.7
GGS075(P31)	0.75	Acid	11	2.7, 34.4	N/A
GGS075(P33)	0.75	Water	11	Intermittent infiltration	N/A
GGS060(P22)	0.60	Water	17	3.1, 9.5, 41.5	3.4, 9.8
GGS050(P23)	0.50	Water	23	3.6, 9, 39.8	3.2, 6
GGS040(P24)	0.40	Water	31	3.2, 9.1, 40.2	3.2, 9.8
GGS025(P12)	0.25	Acid	48	2.4, 5.4, 6.9, 12.2, 21, 32.8, 44.9	3, 24.2
GGS025(P32)	0.25	Acid	48	2.8, 35.9	N/A
GGS025(P34)	0.25	Water	48	Intermittent infiltration	N/A

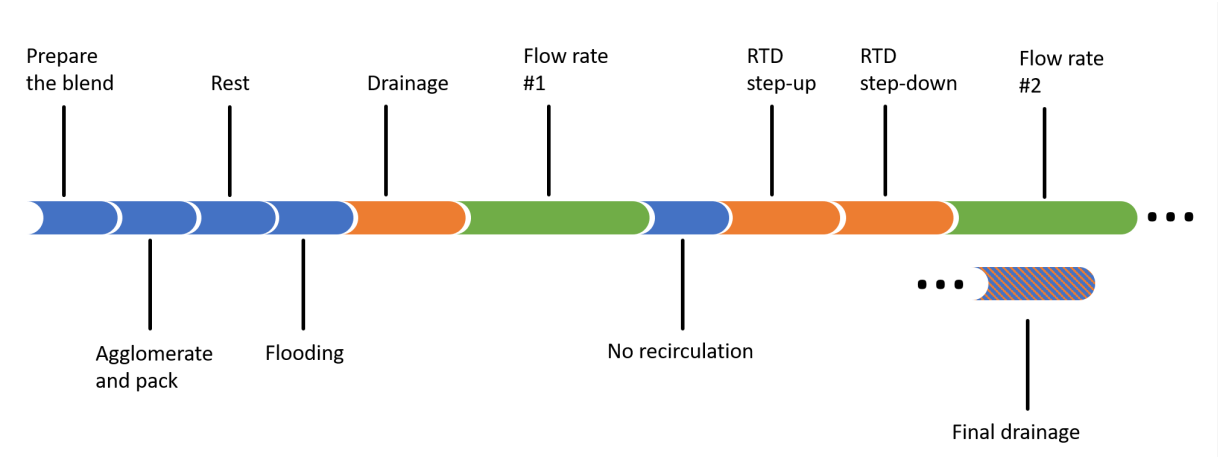

Figure III.9: Experimental procedure diagram. The approximate durations of each experimental step are encoded by colour: blue denotes the step that lasted one day, orange — two days, and green — five days. The final drainage lasted one day for some experiments and two days for others.

While Figure III.9 shows a typical experimental run, there were some variations. The first set of experiments (GGS075(P11)–GGS097(P14)) was used to study the hysteresis. Thus, the irrigation experiments did not stop at the highest flow rate. Instead, they continued with the lower flow rates (see subsection 2 on page 88). Before final drainage started, the columns were once again irrigated at the high flow rate. Blends GGS075(P33) and GGS025(P34) had completely separate experimental campaign that did not involve the initial flooding (see subsection 10 on page 82). The first experimental set took over 90 days to run (this includes downtime due to technical issues, such as tubing breakage or electricity outage). The second set took about 60 days, and the third set — just under 20 days.

Chapter IV

Experimental results and discussion

The purpose of mathematical models is not to fit to data but to sharpen the questions.

— Samuel Karlin

This chapter presents the results of the experiments along side their discussion. It is organised as follows:

- The results regarding flooding and hysteresis are presented first. While these results are not central to this thesis, they provide an important foundation and observations that are used later.
- Solution flow is examined next. Steady-state and transient state experiment results are shown. Application of various models to these results is discussed. In the light of the steady-state experiment results, a new simplified model is proposed and validated.
- The results of the RTD experiments are presented. Application of advection-dispersion and compartment models are examined.
- Finally, an alternative way to model the flow is presented. This model is based on the hypothesis of the stochastic movement of the liquid element in a discrete time. Possible formulation and results are shown.

The detailed experimental data can be found in Appendices B and C.

Table IV.1: Results of the flooding stage of the experiments.

Experiment	Dry ore in column, kg	Bed slump, %	Saturated water volume, including agglomeration moisture, L	Saturated water content, ϑ –	Bulk density, $\times 10^3$ kg · m^{-3}
GGS150(P13)	11.65	0.0	3.87	0.474	1.43
GGS097(P14)	11.57	0.0	3.61	0.451	1.45
GGS075(P11)	11.99	3.5	3.60	0.452	1.51
GGS075(P21)	12.15	12.3	2.95	0.408	1.68
GGS075(P31)	11.86	3.4	3.80	0.469	1.46
GGS060(P22)	12.5	13.3	2.72	0.393	1.80
GGS050(P23)	12.9	17.5	2.41	0.358	1.92
GGS040(P24)	11.93	24.6	2.05	0.340	1.98
GGS025(P12)	10.47	35.1	2.21	0.426	2.02
GGS025(P32)	11.32	23.4	2.14	0.344	1.82

§ 1. Preliminary and side experiments

1. Column flooding. Except for experiments P33 and P34, all the columns were flooded. The flooding results are shown in Table IV.1 (for the full details see table `gravimetric-general.csv` in Appendix B). There is an evident tendency for increased bed slumping and bulk density, and decreased saturated water content with the increasing presence of fines. There is, however, a high variability in these results showing the interference of some other factors, such as agglomeration and packing processes. This trend can be explained by the collapse of agglomerates during flooding. The blends with higher fines content tended to create the agglomerates consisting of mostly fines which were not tightly packed. This was in contrast to agglomerates of coarser blends were the fines were mostly coated on the surface of larger particles. Thus, the flooding caused the collapse of the former but had little effect on the latter.

2. Hysteresis. The results of the hysteresis experiments run on columns GGS075(P11)–GSS097(P14) are shown in Figure IV.1. There is a slight increase in liquid hold-up inside the medium at a given flow rate if the medium's prior hold-up was higher, or, equivalently, the prior irrigation flow rate was higher. The difference, however, is not significant compared to overall liquid hold-up which is in line with the results obtained by Dixon and Afewu (2010).

It must be noted that a rock-pile system may exhibit two kinds of hysteresis. The first kind occurs

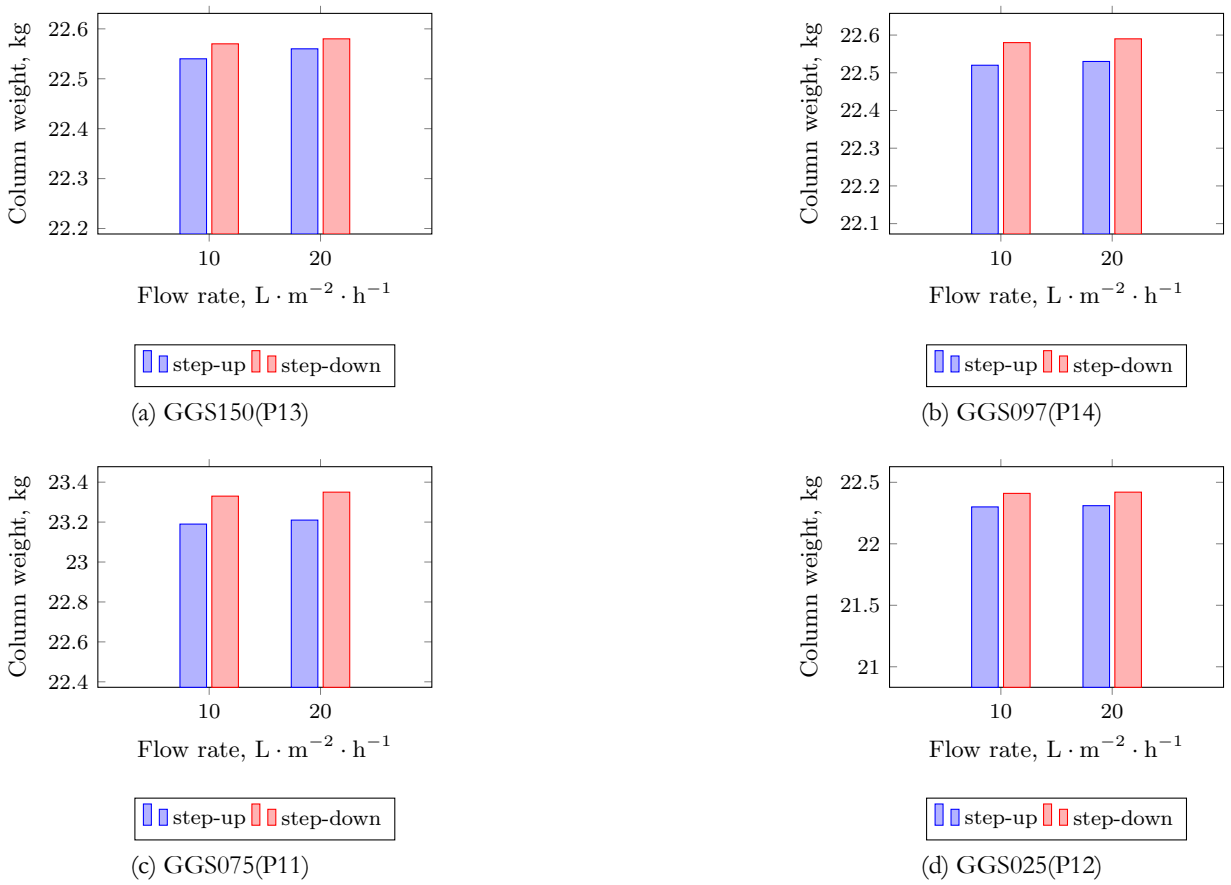

(a) GGS150(P13)

(b) GGS097(P14)

(c) GGS075(P11)

(d) GGS025(P12)

Figure IV.1: Hysteresis demonstrated by different liquid hold-ups at the same flow rates depending whether the rate was increased (step-up, infiltration) or decreased (step-down, drainage). The minimum weight value for each chart is set to the dry packed column weight emphasizing the overall liquid gain.

when the infiltration of dry rocks is compared with the infiltration of previously wetted rocks. The difference can be attributed to establishing new liquid channels (rivulets) in "dry" infiltration, whereas in "wet" infiltration liquid just saturates already established pathways (Ilankoon and Neethling, 2012). However, this type of hysteresis was avoided by flooding the columns prior to conducting gravimetric studies, thus establishing all the rivulets. The alternative explanation for the difference would be that the measured liquid hold-up, for the packing with a higher prior liquid hold-up, is actually not a true steady-state value. As was shown in §4 of Chapter II, any drainage takes much longer time to settle at a new steady-state compared to infiltration.

While hysteresis is an important phenomenon in hydrology, its thorough investigation lies outside the scope of this project and, thus, was not pursued any further.

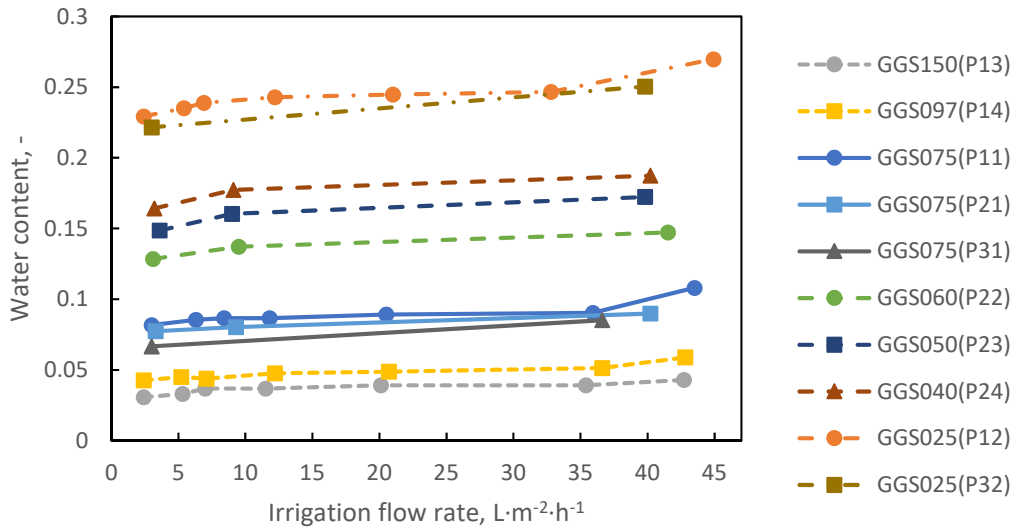

Figure IV.2: Steady-state experiments results showing little effect of different flow rates on water content. There is, however, a significant effect of PSD.

§ 2. Solution flow results

1. Summary of steady-state results. The results of the experiments in terms of the water content $\vartheta = V_{\text{water}}/V_{\text{bed}}$ are presented in Figure IV.2 (the raw weight measurements can be found in table `gravimetric-steady-state.csv` in Appendix B). It is evident that water content does not change significantly within the range of flow rates typical for heap leaching: the change in ϑ for a single PSD does not exceed 0.04 (maximum for GGS025(P12)) or 29% (maximum for GGS150(P13)). In contrast, it varies substantially with the change of PSD: from about 0.05 for GGS150(P13) to 0.27 for GGS025(P12).

2. Infiltration curves. Infiltration results for the first set of columns GGS075(P11)–GGS097(P14) are shown in Figure IV.3. Irrigation tubing breakage occurred for column GGS075(P11) resulting in a decreasing weight over one hour, after which the tubing was repaired.

As these experiments started with columns that were previously flooded, there was a significant amount of moisture already present in the columns. This resulted in very rapid weight gain over a narrow weight range. Surprisingly, the column with the largest fines content (GGS025(P12)) was the fastest to achieve a steady-state weight. This can be explained by smaller pore radii in this packing being able to hold and accumulate the incoming liquid before percolation occurred. In contrast, larger pore radii in GGS150(P13) resulted in smaller capillary forces allowing more liquid to percolate through right at the start of the irrigation process.

The short times to reach steady state and the narrow weight range of the infiltration experiments did not produce results with enough information in them for a substantial analysis using hydrology models: although the infiltration curves put some bounds on hydraulic parameters values, the subsequent steady-state and drainage experiments produced more reliable and richer datasets. Therefore, carefully measured infiltration experiments were not repeated.

3. Intermittent infiltration. produced results similar to normal infiltration. This time, however, the range of the weight was wider enabling a more detailed examination (Figure IV.3). Percolation in column GGS075(P33) was achieved within one hour, resulting in slight weight loss during the first no-flow period. In contrast, GGS025(P34) did not percolate in the first hour and the weight of the column stayed constant during the first no-flow period. Although no-flow periods were short, it is possible to see that drainage during these periods occurred more slowly compared to infiltration. The gradient of the weight loss became noticeably flatter at the end of the off-period in both columns. The second run of the column GGS025(P34) produced lower overall saturation values. This can be explained by the slumping of the bed during the first run: a 5.1 cm slump, compared to a 0.5 cm in column GGS075(P33). Despite this difference in GGS025(P34), the gradients of weight gain and loss are the same (by visual inspection) in the first "dry" run and the second "wet" run.

4. Drainage. The liquid loss during drainage for each set of experiments is shown in Figure IV.5. Due to different liquid content and overall volume of each packing (the latter even for columns with the same PSD), the data does not show any distinct trend. These results are used in the discussion of the Richards equation-based model application in subsection 3.3 further below.

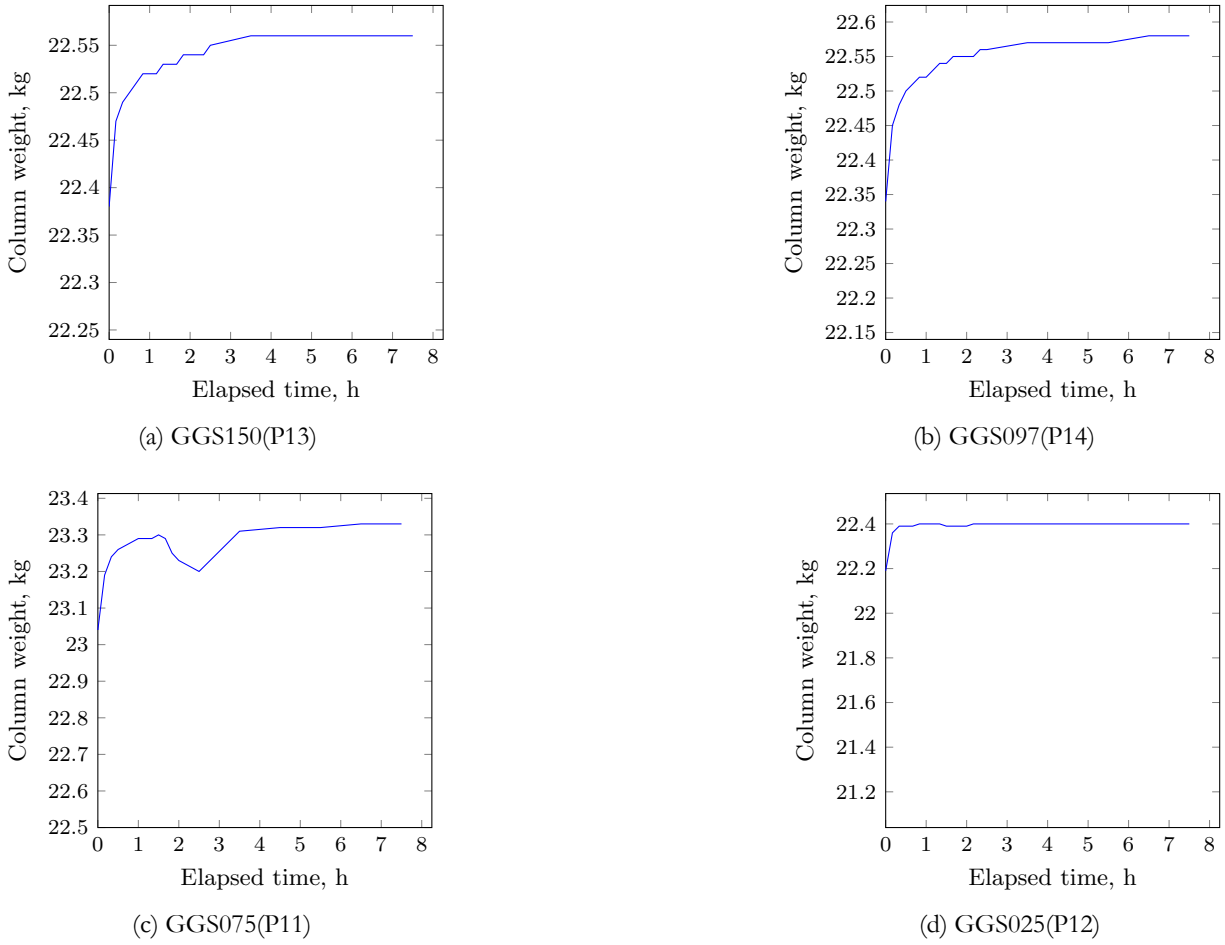

(a) GGS150(P13)

(b) GGS097(P14)

(c) GGS075(P11)

(d) GGS025(P12)

Figure IV.3: Example of the infiltration curve starting from some initial saturation (after two-day drainage), conducted at a flow rate of 40 $\mathrm{L} \cdot \mathrm{m}^{-2} \cdot \mathrm{h}^{-1}$. The smallest value of the y-axis on each chart is selected to be the dry column weight. The curve of the GGS075(P11) chart has a dip due to tubing breakage that occurred two hours after the start of the experiment.

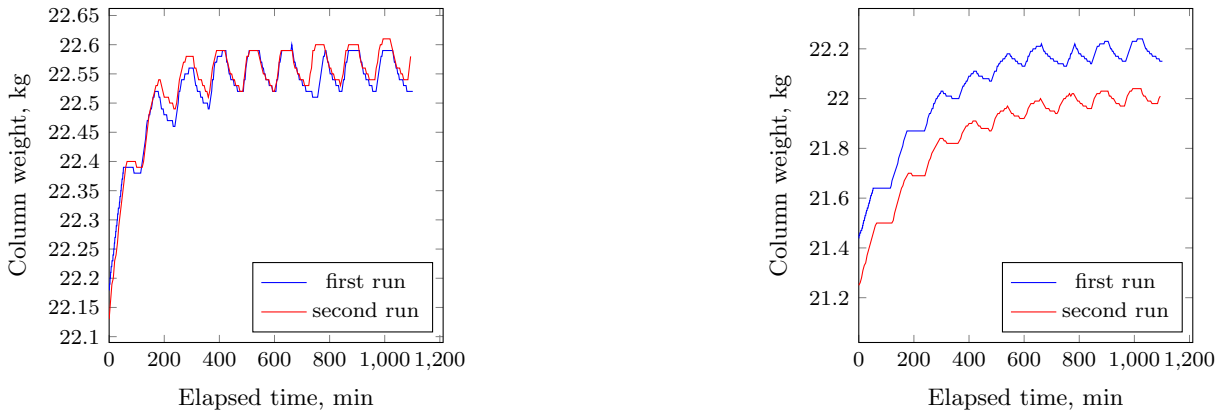

(a) GGS075(P33)

(b) GGS025(P34)

Figure IV.4: Results of intermittent flow experiments of columns that were not previously flooded.

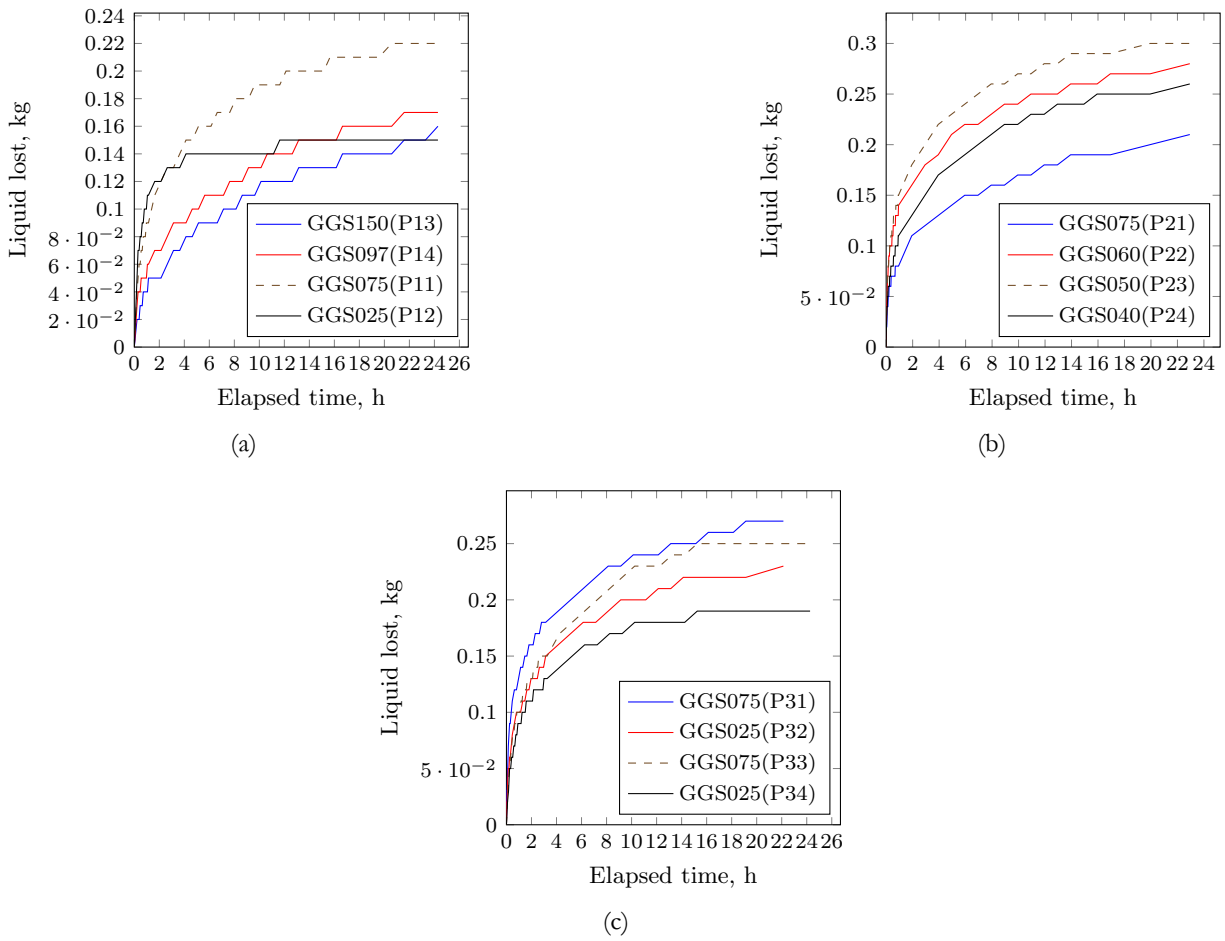

Figure IV.5: Results of the drainage experiment for the columns of the three sets.

§ 3. Solution flow discussion based on the Richards equation model

1. Choice of residual water content ϑ_r. The following analysis uses some form of the Richards equation to deduce the flow properties. This analysis requires transforming water content data to effective saturation

$$s = \frac{\vartheta - \vartheta_r}{\vartheta_s - \vartheta_r},$$

which, in turn, requires the values of saturated and residual water contents. The former is directly measured by flooding. The deduction of the latter from the drainage is problematic due to extremely slow rates of drainage (see section § 4 on page 33 of Chapter II). The alternative would be to retrospectively fit the value of ϑ_r using the model (Sheikhzadeh et al., 2005). It is, however, computationally

Table IV.2: Comparison of two heuristic rules to choose residual water content from drainage data.

Experiment	Estimated ϑ_r	
	95–94% rule	85% after 24 hours rule
GGS150(P13)	0.020	0.020
GGS097(P14)	0.026	0.028
GGS075(P11)	0.066	0.061
GGS075(P21)	0.055	0.049
GGS075(P31)	0.048	0.044
GGS060(P22)	0.10	0.091
GGS050(P23)	0.12	0.11
GGS040(P24)	0.13	0.12
GGS025(P12)	0.22	0.20
GGS025(P32)	0.20	0.18

expensive and there is a risk of over-fitting the model. A compromise approach is taken in this study by estimating residual water content from 24 or 48 hours of drainage experiments. It is a shortcut approach that is used in absence of a better practical method. After experimenting with different values, ϑ_r was set to 95% of the water content after 48 hours of drainage and 94% after 24 hours if the drainage did not last for 48 hours (see Table IV.2 comparing this heuristic to another one: 85% of the water content recorded after 24 hours of drainage). Although not firmly grounded in theory, the proposed heuristic provides a reasonable fit of the drainage data as will be shown in subsection 3 and is consistent with ϑ_r estimates in the literature from longer drainage experiments (Dixon and Afewu, 2010). Future studies may look at a more systematic way of estimating ϑ_r.

2. Application of the steady-state uniform model (SSUM) to experimental data. Table IV.3 summarizes the results of fitting the van Genuchten model parameters to experimental results obtained by minimizing the penalty function defined as follows:

$$\mathcal{P}(K_s, n) = \sqrt{\frac{1}{N}\sum_{i=1}^{N}\left(\lg\left[\frac{K(s_i;\{K_s,n\})}{V_i}\right]\right)^2} \tag{IV.1}$$

where s_i and V_i are experimentally measured effective saturation and specific discharge respectively. Equation (IV.1) uses the difference of logarithms (of base 10) of conductivity and specific discharge since their values change in order of magnitude. Thus, the use of direct values would have placed an unduly large weight on data points at high flow rates. The minimization procedure was restricted to

Table IV.3: Experimentally determined values of hydraulic parameters K_s and m.

Experiment	N	$K_s, \mathrm{m} \cdot \mathrm{s}^{-1}$	$n, -$	$m = 1 - 1/n, -$	$\mathcal{P}(K_s, n)$
GGS150(P13)	7	5.08	2.372	0.578	0.080
GGS097(P14)	7	2.81	2.197	0.545	0.160
GGS075(P11)	7	0.0102	9.257	0.892	0.195
GGS075(P21)	3	10	1.738	0.425	0.078
GGS060(P22)	3	0.548	1.788	0.441	0.050
GGS050(P23)	3	0.00861	2.483	0.597	0.094
GGS040(P24)	3	0.0108	2.066	0.516	0.114
GGS025(P12)	7	0.00149	10	0.9	0.178

$1.1 \leq n \leq 10$ and $0.001 \leq K_s \leq 10$. Only the first two sets of experiments were used for this analysis as the third set (GGS075(P31)–GGS025(P34)) has too few data points.

The confidence in hydraulic parameter estimates is low as it was expected for the experiments GGS075(P11) and GGS075(P21) to have similar parameters values. However, if the value of the penalty function is plotted against the variation of $\lg K_s$ and n, it can be seen that both sets of parameters' values for GGS075 experiments are close to the minimum of the penalty function (Figure IV.6). The issue is that the function $\mathcal{P}(K_s, n)$ does not have a definitive minimum. Instead, it forms an L-shaped valley of minima on the $\lg K_s$–n plane. This is in agreement with the observation made by Guzman et al. (2002). The main source of uncertainty is the value of saturated conductivity K_s since for practical reasons all the experiments were conducted at flow rates orders of magnitude lower than the expected values of K_s. This raises the question of validity of the van Genuchten hydraulic model and, more generally, the Richards equation model in the context of low flow rates (note, it only "raises the question" as by itself this result cannot provide the affirmative answer).

The investigation of parameter dependence of equation (II.11) of Chapter II on hydraulic parameters ℓ and n and dimensionless flow rate $\mathfrak{k} = q/K_s$ for the fitted values of Table IV.3 and irrigation flow rate $q_{\text{in}} = 5\ \mathrm{L} \cdot \mathrm{m}^{-2} \cdot \mathrm{h}^{-1}$ results in relative perturbance multiplier matrix $\mathbf{\Gamma}$ shown in Table IV.4 (see subsection 3.2 of Chapter II for matrix $\mathbf{\Gamma}$ definition). In this case $\mathbf{\Gamma}$ is a 1×3 row-matrix with each component corresponding to the variance of each of the parameters $\{\ell, n, \mathfrak{k}\}$. The results indicate amplified sensitivity towards variation of parameter n (and, as a result, $m = 1 - 1/n$). At the same time, this sensitivity will stay bound as far as saturation is not zero (or more precisely, separated from zero). Figure IV.7 demonstrates the dependence of saturation on n in the range 1.3–2.0 and $\mathfrak{k}$ in the

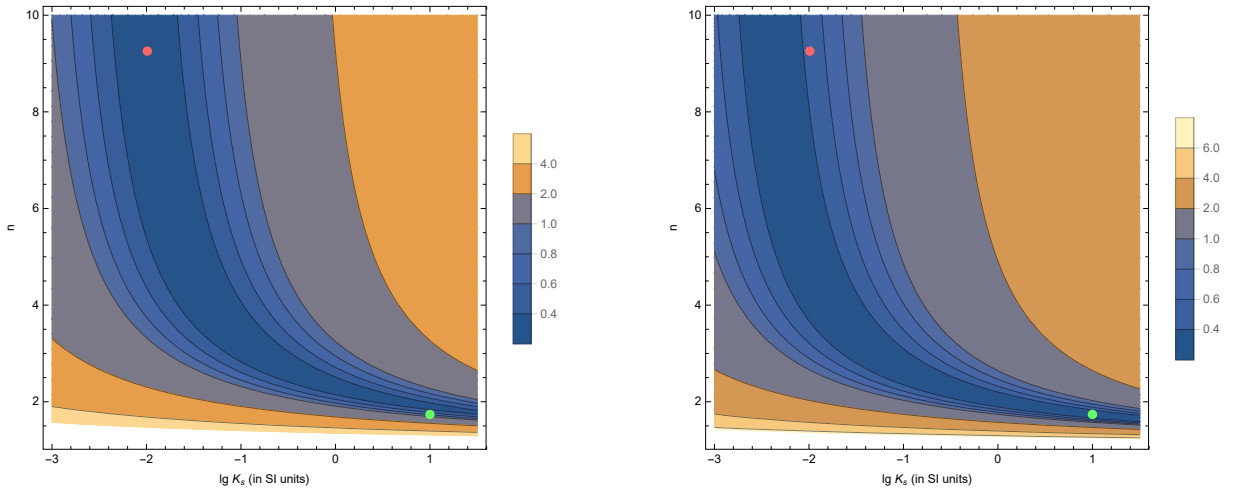

(a) GGS075(P11) (b) GGS075(P21)

Figure IV.6: Contour plots of the penalty function for GGS075(P11) and GGS075(P21) data with the light red and light green points showing the identified minimum for P11 and P21. These plot suggest no confident minimum of the penalty function can be determined from the experimental data.

Table IV.4: Sensitivities of saturation towards the change of hydraulic parameters for experiments and inlet flow rate $q_{\text{in}} = 5\ \text{L} \cdot \text{m}^{-2} \cdot \text{h}^{-1}$.

Experiment	s, –	Sensitivity towards, –		
		ℓ	n	$\lg \mathbb{k}$
GGS075(P11)	0.135	0.155	−4.28	−2.34
GGS075(P21)	0.144	0.134	−4.94	−2.27
GGS060(P22)	0.255	0.079	−4.65	−1.69
GGS050(P23)	0.395	0.034	−5.82	−1.20
GGS040(P24)	0.471	0.023	−5.92	−1.00
GGS025(P12)	0.520	0.020	−5.24	−0.90

range 10^{-10}–10^{-2}. At flow rates typical for heap leaching $\mathbb{k}$ (estimated as q_{in}/K_s) lies between 10^{-7} and 10^{-5}. It is evident that in this range saturation does not strongly depend on the correctness of K_s estimate or on flow rate. .

3. Application of the transient one-element model (TOEM) to the experimental data. It was demonstrated in section 5 of Chapter II that during drainage capillary pressure gradients vanish and the flow is driven by gravity only. Thus, a simplified transient-one-element model (TOEM) can be applied for experimental data analysis. Using the hydraulic parameter values obtained by fitting steady-state data (Table IV.3), the drainage curve of the TOEM was obtained (see Figures IV.9 and IV.10).

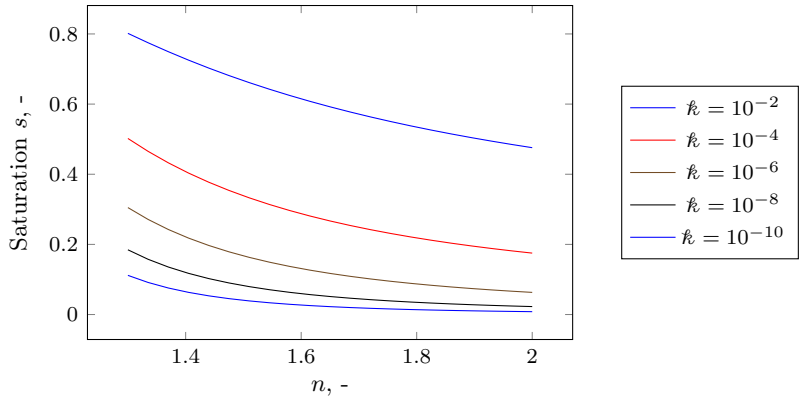

Figure IV.7: Dependence of saturation on hydraulic parameters n and $\hbar$.

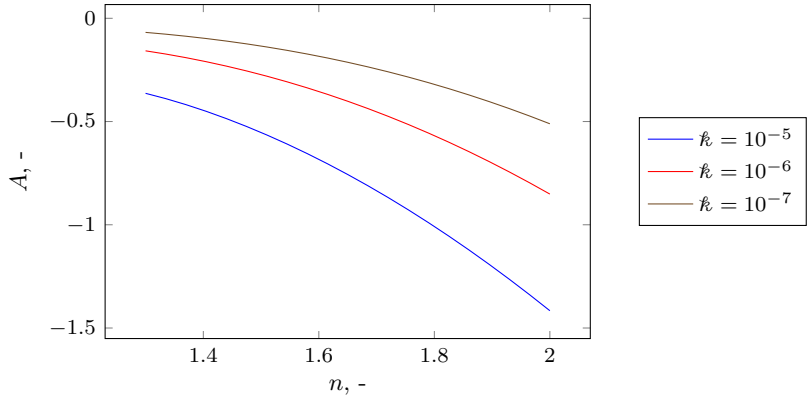

Figure IV.8: Jacobian A of ODE (II.10) as a function of hydraulic parameters n and $\hbar$.

Comparison of the experimental and model results for GGS075(P11) shows a significant difference between the curves: experimental data suggests that drainage would proceed more slowly and the saturation reached after 24 hours would be higher compared to the model prediction. The model results deviate even further from the experiment for GGS025(P12) — the model substantially over-predicts the liquid loss in the first 24 hours. Even though the model fits the second set of experiments, GGS075(P21)–GGS040(P24), better, there is still a difference in the dynamics.

The data in Table IV.3 was obtained by using the steady-state model to analyse steady-state results. The overall number of data points may be insufficient to provide a proper fit. Instead, drainage data with many more points (around 50) may be a better choice for calibration. In this case the penalty function is stated directly in terms of saturation:

$$\mathcal{P}_D(K_s, n) = \sqrt{\frac{1}{M}\sum_{i=1}^{M}(s_{\text{model}}(t_i; s_0, K_s, n) - s_{\text{experiment}}(t_i),}$$

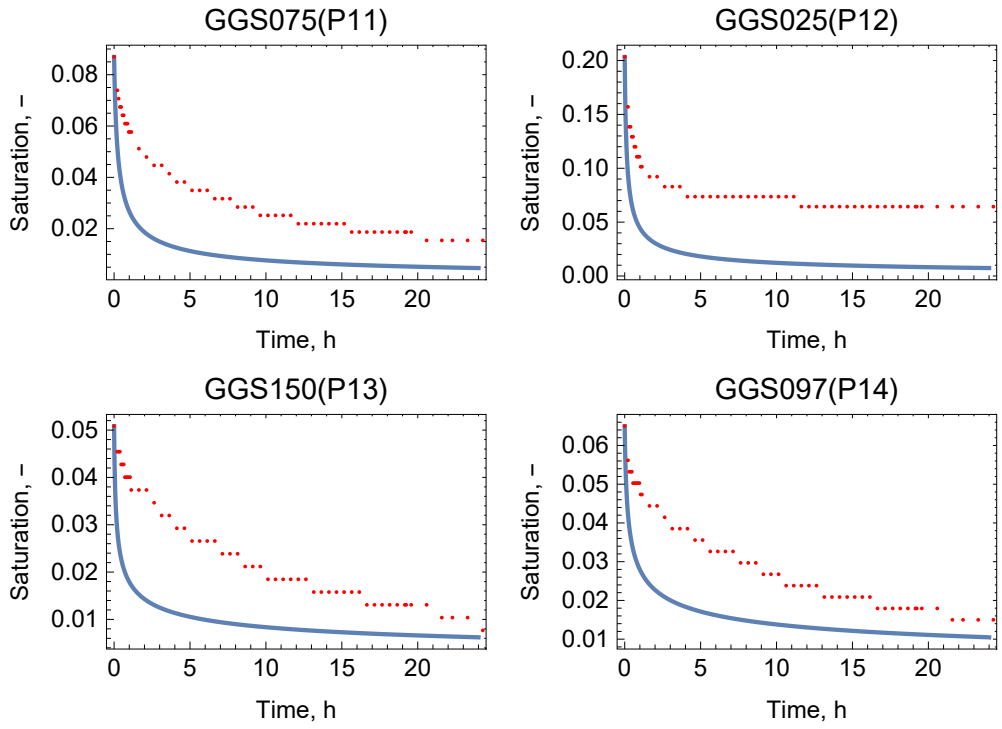

Figure IV.9: Comparison of the drainage experimental data and the results of TOEM with parameters listed in Table IV.3 for the first set of columns. Solid blue line refers to the model results. Dotted red line is showing experimental data.

where M is the number of data points used, $s_{\text{model}}(t; s_0, K_s, n)$ is the saturation predicted by TOEM and $s_{\text{experiment}}(t)$ is the experimentally obtained saturation at t. The results of the calibration are shown in Table IV.5 and Figures IV.11 and IV.12. Newly obtained values of K_s and n are significantly different compared to the steady-state calibration (Table IV.3). Furthermore, use of these new values of K_s and n to obtain the saturations for the steady-state experiments (with SSUM) produces values that are far off from experimental saturation (Figures IV.13 and IV.14).

This section has demonstrated a few issues arising from application of the Richards equation model to the liquid flow in packed rock beds. First and foremost, the model answers a wrong question: it establishes the saturation (water content) for a given irrigation flow rate. Steady state experiments, however, have demonstrated that the dependency of the water content on the irrigation flow rate in the range used in heap leaching context is weak. The effect particle size distribution (PSD) has on saturation is far greater. This effect, however, cannot be predicted by the Richards equation model as it is incorporated via hydraulic parameters which are the inputs to the model. Furthermore, the overall poor fit of the combination of the drainage curves and steady state saturations indicates unsatisfactory

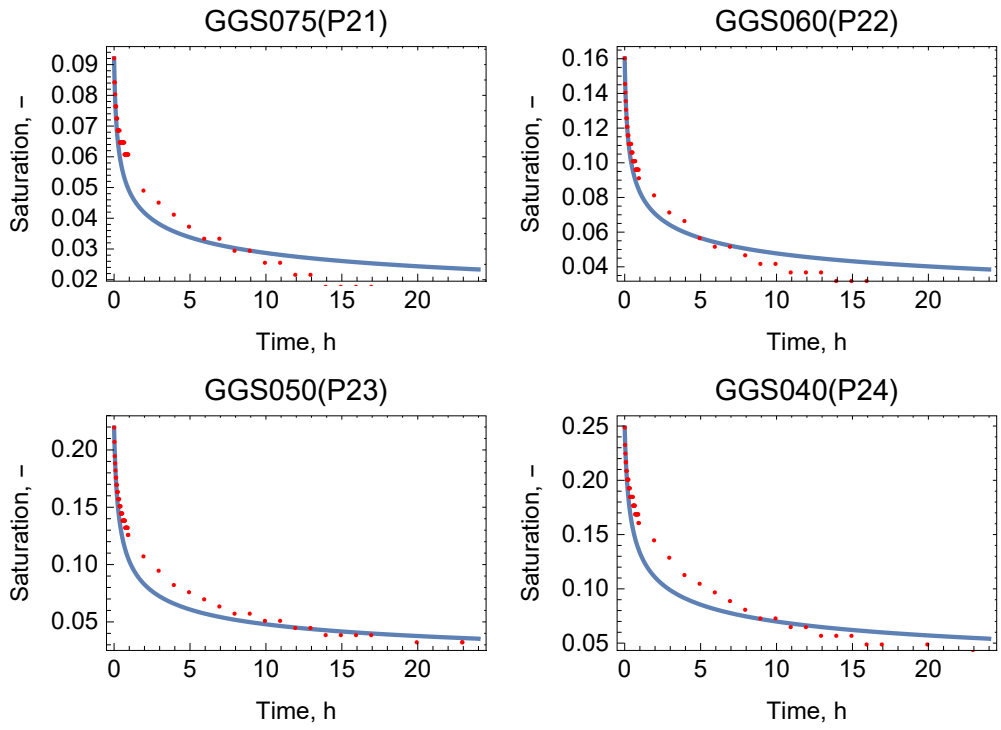

Figure IV.10: Comparison of the drainage experimental data and the results of TOEM with parameters listed in Table IV.3 for the second set of columns.

Table IV.5: Experimentally determined values of hydraulic parameters K_s and m from drainage data.

Experiment	$K_s, \mathrm{m} \cdot \mathrm{s}^{-1}$	$n, -$	$m = 1 - 1/n, -$	$\mathcal{P}_D(K_s, n)$
GGS150(P13)	0.00253	10	0.9	0.080
GGS097(P14)	0.00149	10	0.9	0.160
GGS075(P11)	0.00284	5.485	0.8177	0.195
GGS075(P21)	0.0518	2.616	0.6177	0.078
GGS060(P22)	0.0311	2.288	0.5629	0.050
GGS050(P23)	0.00415	2.617	0.6179	0.094
GGS040(P24)	0.00127	2.691	0.6284	0.114
GGS025(P12)	2.376	1.517	0.3408	0.178

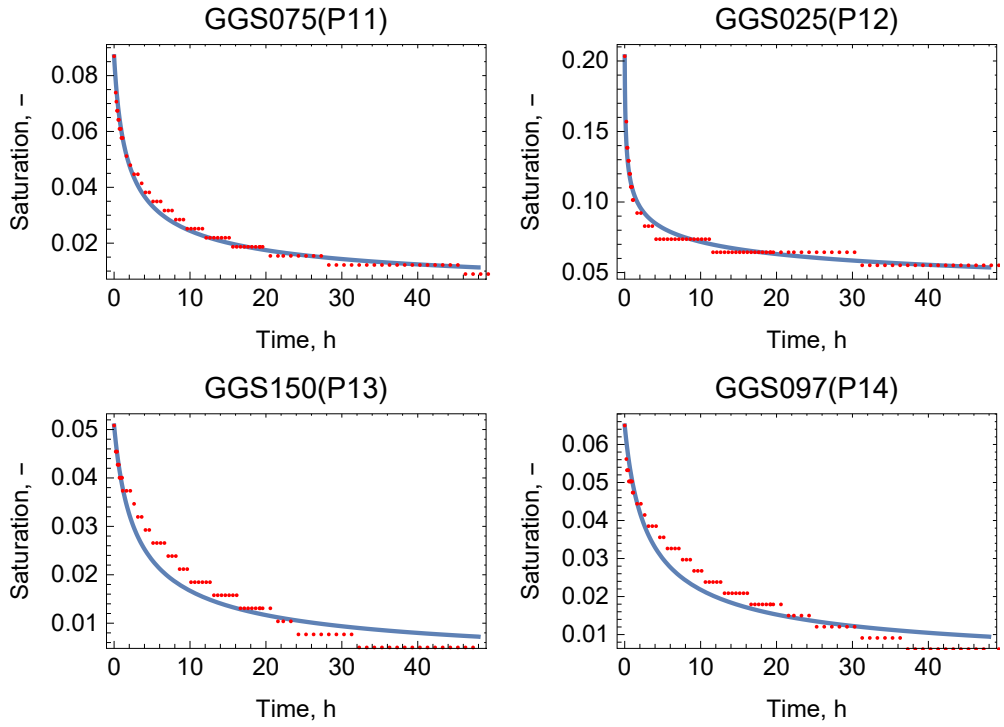

Figure IV.11: Result of calibration of TOEM for the first set of experiments.

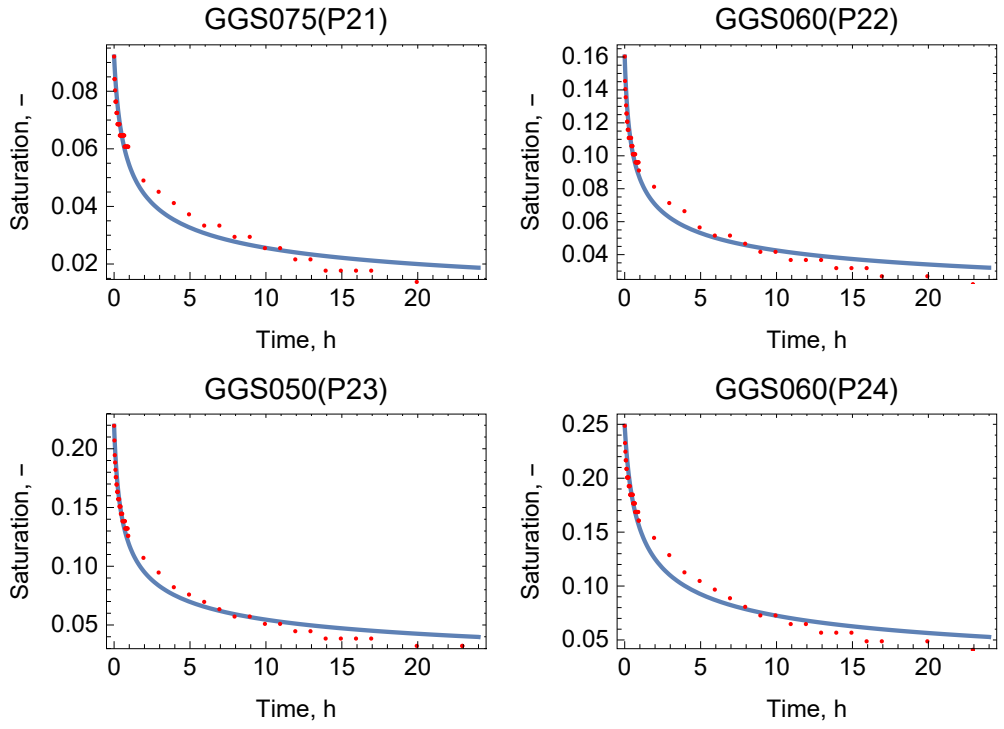

Figure IV.12: Results of calibration of TOEM for the second set of experiments.

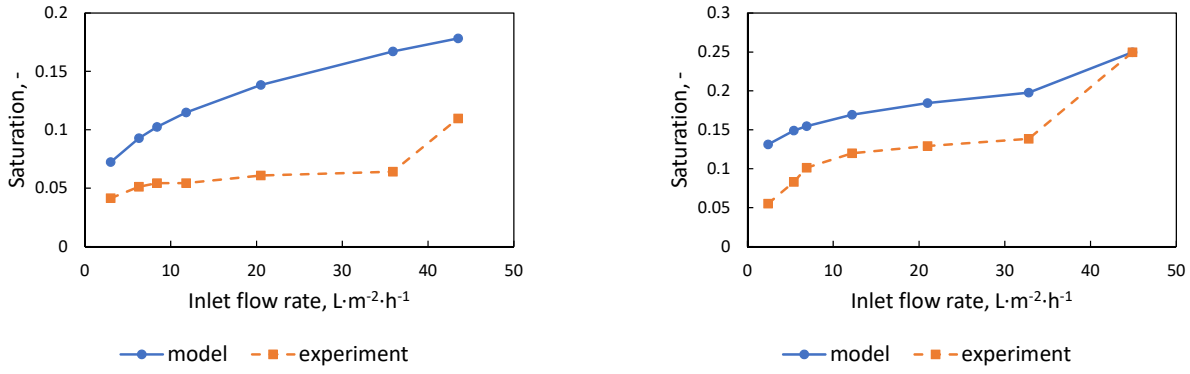

(a) GGS075(P11)

(b) GGS025(P12)

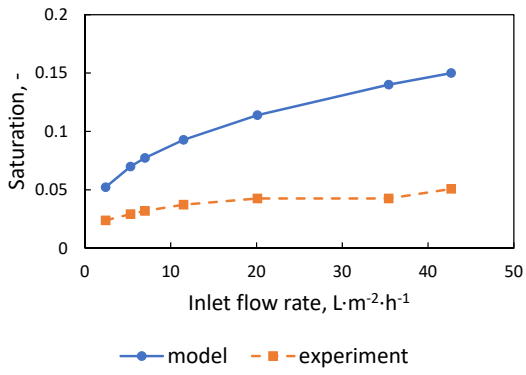

(c) GGS150(P13)

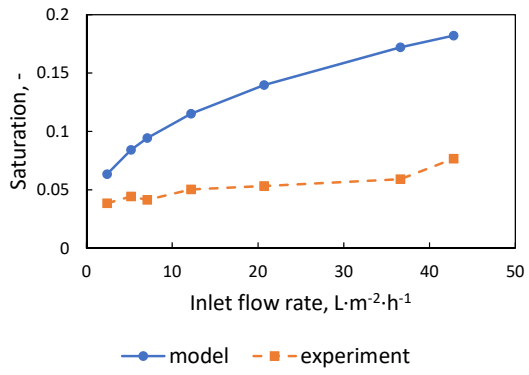

(d) GGS097(P14)

Figure IV.13: Comparison of steady-state saturations between the model and experimental results for the first set of experiments. The model parameters were set by fitting drainage data.

predictive capabilities of this model. There are two likely reasons for this. First, the range of the flow rates used in heap leaching is close to the point of inflection of the water retention curve $K_r(s)$. Secondly, the scale of the experiments is not big enough for the assumptions underlying the Richards equation model to be valid. The latter is also indicated by the preferential flow and tomography studies (see subsections 5.3 and 5.4 of Chapter I) that point towards a strong stratification between moving and stagnant liquid in packed rock beds, whereas the original form of the Richards equation requires a continuous distribution of liquid velocities across the domain. Hence, it must be concluded that the use of the Richards equation models for quantitative analysis is impractical in this context. The next section provides an alternative model with predictive capabilities to connect PSD and the liquid hold-up directly.

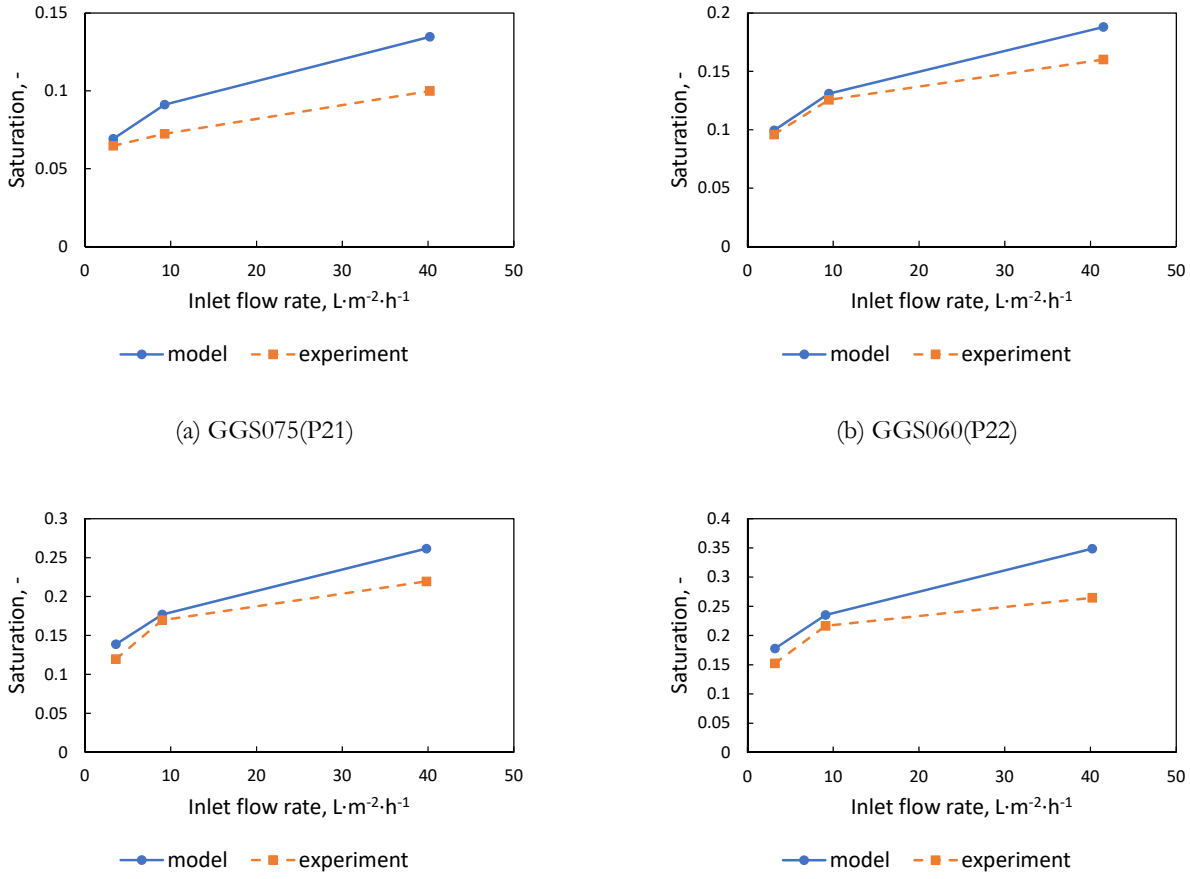

(a) GGS075(P21)

(b) GGS060(P22)

(c) GGS050(P23)

(d) GGS040(P24)

Figure IV.14: Comparison of steady-state saturations between the model and experimental results for the second set of experiments. The model parameters were set by fitting drainage data.

§ 4. A novel model for the steady-state liquid hold-up

1. Model assumptions. The results of the steady-state experiments (see Figure IV.2) point to the more important effect of PSD compared to irrigation flow rate on the liquid hold-up in packed rock beds. As the water content tends to positively correlate with the increase of fines in the packed bed, it is proposed that the moisture is kept on the particle surface. More precisely it can be stated as the series of the following assumptions:

Assumption 1. *The thickness of the liquid layer on the particle surface is small compared to the particle radius.*

Assumption 2. *Liquid occupies a fixed portion of a particle surface, independent of the particle size. The thickness of this liquid layer is also independent of the particle size.*

There are two points regarding Assumption 2 that require some unpacking. First, the assumption of the liquid thickness being the same for all particle sizes may be quite crude. A more careful derivation based on forces balance may provide a finer expression of the liquid layer thickness as a function of a particle radius. However, Assumption 1 provides a justification for it: since the liquid layer is thin, the surfaces at both interfaces, solid-liquid and liquid-air, can be assumed flat, and, thus, would result in the same force balance independent of particle size. Secondly, the effect of intra-particle pores is not considered. Although some research on the effect of particle porosity on the liquid hold up had been conducted (Ilankoon and Neethling, 2013), there are a few practical issues to include this effect into the present analysis:

- It is hard to differentiate between the liquid held on the particle surface and inside particle pores due to roughness of particle surface;
- The measurement of the liquid held inside the particle used by Ilankoon and Neethling (2013) is highly inaccurate since the removal of liquid from the particle surface also pulls the liquid from inside the particle.

Therefore, intra-particle liquid is assumed to be accounted for by the liquid on the particle surface.

From the above assumptions it follows that

Corollary 1. *Liquid volume retained in the packed rock bed under low irrigation rates is proportional to the total surface area of all the particles.*

The total surface area of all the particles in the bed can be estimated using the third

Assumption 3. *Each particle is a perfect sphere. The whole surface of each particle is exposed to the liquid, i.e. there is no surface that is covered by another particle.*

Finally, although not strictly necessary, the last assumption provides a simplification for the derivation to follow:

Assumption 4. *It is also assumed that the liquid occupies the whole particle surface.*

2. Model derivation. Let $m_s(x)\,\mathrm{d}x$ be the mass of particles with the size in the range $(x, x+\mathrm{d}x)$ where x is particle diameter. According to the PSD probability density function (PDF):

$$m_s(x)\,\mathrm{d}x = M_s \mathit{p}(x)\,\mathrm{d}x,$$

where M_s is the total solid mass and $\mathit{p}(x)$ is PDF of PSD. The mass can be expressed via bed volume $\mathscr{V}$, solids density ρ_s and porosity ϕ as follows:

$$M_s = \rho_s(1-\phi)\mathscr{V}.$$

Therefore,

$$m_s(x)\,\mathrm{d}x = \rho_s(1-\phi)\mathscr{V}\mathit{p}(x)\,\mathrm{d}x.$$

Conversely, the mass of these particles can be expressed using individual particle volumes:

$$m_s(x)\,\mathrm{d}x = \frac{\pi}{6}\rho_s \mathscr{N}(x)x^3\,\mathrm{d}x,$$

where $\mathscr{N}(x)\,\mathrm{d}x$ is the number of particles in the range $(x, x+\mathrm{d}x)$. Combining the last two equations, $\mathscr{N}(x)$ can be expressed as

$$\mathscr{N}(x) = \frac{6}{\pi}(1-\phi)\mathscr{V}\frac{\mathit{p}(x)}{x^3}.$$

The surface area $\mathscr{A}(x)\,\mathrm{d}x$ of particles in the size range $(x, x+\mathrm{d}x)$ is then

$$\mathscr{A}(x)\,\mathrm{d}x = \pi x^2 \mathscr{N}(x)\,\mathrm{d}x = 6(1-\phi)\mathscr{V}\frac{\mathit{p}(x)}{x^3}\,\mathrm{d}x.$$

It is more convenient to express the surface area $\mathscr{A}$ as the specific surface area defined per bed volume:

$$\mathscr{a}(x) = \frac{\mathscr{A}(x)}{\mathscr{V}} = 6(1-\phi)\frac{\mathit{p}(x)}{x}.$$

Thus, the total (specific) surface area is

$$\mathscr{a} = 6(1-\phi)\int_0^{\Xi}\frac{\mathit{p}(x)}{x}\,\mathrm{d}x, \tag{IV.2}$$

where Ξ is the top size of particles in the distribution (or infinity if the distribution is unbound).

3. Cut-off minimum size. Specific surface area for GGS. For some distributions, including GGS with the distribution modulus (exponent) $\lambda < 1$, the integral in equation (IV.2) will be divergent at $x = 0$ as in these distributions infinitely small particles would have infinitely large surface area. To avoid this problem, the distribution is adjusted such that $p(x) \equiv 0$ for $0 < x < \xi$ for some small value of ξ. The physics of this adjustment can be viewed in two ways. First, in reality PSD will have some smallest size after which the PDF will be nearly zero. Secondly, in relation to the liquid covering ore particles, it can be proposed that extremely small particles do not influence that coverage — they either get stuck to the surface of larger particles or get suspended in liquid. From the choice of ξ further below it will be apparent that it is too large to be the minimum size of distribution. Thus, the following assumption is stated:

Assumption 5. *Small particles with the diameter below some fixed value ξ do not affect the liquid hold-up as they tend to adhere to larger particles or become suspended in the surrounding liquid.*

Let's $\bar{\mathcal{P}}_\xi(x)$ denote a cumulative distribution function (CDF) of the PSD for particles that contribute to the liquid hold-up. If $\mathcal{P}(x)$ is the CDF of the overall PSD, these functions are related as follows:

$$\bar{\mathcal{P}}_\xi(x) = \mathcal{P}(x)\Theta(x - \xi),$$

where $\Theta(x)$ is the Heaviside theta-function (step-function). Using a generalized derivative of the Heaviside function:

$$\langle \Theta'(x), \varphi(x) \rangle = -\langle \Theta(x), \varphi'(x) \rangle = \varphi(0) = \langle \delta(x), \varphi(x) \rangle ,$$

where $\delta(x)$ is Dirac's delta-function (distribution), the distribution PDF has the form

$$\bar{p}_\xi(x) = p(x)\Theta(x - \xi) + \mathcal{P}(\xi)\delta(\xi).$$

Substitution of this expression in place of $p(x)$ in equation (IV.2) results in

$$\mathscr{a} = 6(1 - \phi) \left[\int_\xi^\Xi \frac{p(x)}{x} \, \mathrm{d}x + \frac{\mathcal{P}(\xi)}{\xi} \right].$$

Since the data is usually available in the form of CDF $\mathcal{P}(x)$, integration by parts can put the integral into a more convenient form:

$$\mathscr{a} = 6(1 - \phi) \left[\int_\xi^\Xi \frac{\mathcal{P}(x)}{x^2} \, \mathrm{d}x + \frac{1}{\Xi} \right]. \tag{IV.3}$$

Application of equation (IV.3) to GGS distribution

$$\mathscr{P}(x) = \left(\frac{x}{\Xi}\right)^{\lambda}$$

results in the following expression

$$\mathscr{a} = \frac{6(1-\phi)}{(1-\lambda)\Xi}\left[\left(\frac{\Xi}{\xi}\right)^{1-\lambda} - \lambda\right]. \tag{IV.4}$$

The advantage of equation (IV.3) over equation (IV.4) is that it can be applied to ore PSD data directly, avoiding fitting the distribution. It does, however, require approximation of the integral, which can be performed, for example, by the trapezoid rule:

$$\int_{\xi}^{\Xi} \frac{\mathscr{P}(x)}{x^2}\,\mathrm{d}x \approx \frac{x_1-\xi}{2}\left(\frac{\mathscr{P}(\xi)}{\xi^2} + \frac{\mathscr{P}(x_1)}{x_1^2}\right) + \sum_{i=2}^{N}\frac{x_i - x_{i-1}}{2}\left(\frac{\mathscr{P}(x_{i-1})}{x_{i-1}^2} + \frac{\mathscr{P}(x_i)}{x_i^2}\right),$$

where x_i, $i = 1, \ldots, N$ are screen sizes with x_1 being the smallest screen size large than ξ. If ξ does not coincide with any screen sizes, CDF value $\mathscr{P}(\xi)$ can be linearly approximated using neighbouring screen sizes $x_0 < \xi < x_1$:

$$\mathscr{P}(\xi) \approx \frac{\mathscr{P}(x_1)(\xi - x_0) + \mathscr{P}(x_0)(x_1 - \xi)}{x_1 - x_0}.$$

The minimum size cut-off approach requires a choice of ξ. In the following analysis three values of ξ were tested: 0.1325, 0.265 and 0.53 mm. These values were arbitrarily chosen such that $\Xi/\xi = 200, 100$ and 50 respectively.

4. Specific area of blends. Since the blends GGS150-GGS025 were prepared with particles of size $+1.4$ mm and for -1.4 mm particles only their overall content was varied but not their distribution, their CDFs do not follow GGS distribution exactly (see subsection 3.2 of Chapter III). Hence, the integral form of the specific area was used (equation (IV.3)) with trapezoid approximation of the integral as described in the previous subsection. The calculated values of $\mathscr{a}$ are shown in Table IV.6. Furthermore, to simplify the comparison, relative specific areas $\mathscr{a}_r$ were calculated as a ratio of the specific area $\mathscr{a}$ of the distribution to the specific area of GGS075 (thus, for GGS075, $\mathscr{a}_r = 1$). Table IV.6 shows the results for three different values of ξ: 0.1325, 0.265, and 0.530 mm.

While the actual specific area $\mathscr{a}$ changes significantly with the change of ξ (especially for the distribution with high fines content), relative area $\mathscr{a}_r$ remains more or less constant. This observation

Table IV.6: Specific area calculated for PSD blends used in the experiments. Relative specific area $\mathscr{a}_r$ is the fraction of the area when compared with GGS075 blend.

	GGS150	GGS097	GGS075	GGS060	GGS050	GGS040	GGS025
$\Xi/\xi = 200, \xi = 0.1325$ mm							
$\mathscr{a}$, mm^{-1}	0.487	0.399	2.512	4.042	5.581	7.533	11.35
$\mathscr{a}_r$, –	0.194	0.159	1.00	1.609	2.222	2.999	4.518
$\Xi/\xi = 100, \xi = 0.265$ mm							
$\mathscr{a}$, mm^{-1}	0.354	0.399	1.240	1.888	2.526	3.317	4.832
$\mathscr{a}_r$, –	0.286	0.322	1.00	1.522	2.036	2.674	3.895
$\Xi/\xi = 50, \xi = 0.530$ mm							
$\mathscr{a}$, mm^{-1}	0.350	0.399	1.203	1.825	2.436	3.194	3.677
$\mathscr{a}_r$, –	0.291	0.332	1.00	1.516	2.025	2.654	3.857

requires further investigation. Let $\mathscr{a}_i$ to be the specific area for a blend with $i = 0$ referring to GGS075 and $i = 1, 2, \ldots$ referring to other blends. These values can be viewed as functions of ξ: $\mathscr{a}_i(\xi)$. The observation about the relative specific area means that

$$\frac{\mathscr{a}_i(\xi)}{\mathscr{a}_0(\xi)} \approx \frac{\mathscr{a}_i(\xi+\Delta\xi)}{\mathscr{a}_0(\xi+\Delta\xi)} \quad \text{or} \quad \frac{\mathscr{a}_i(\xi+\Delta\xi)/\mathscr{a}_0(\xi+\Delta\xi)}{\mathscr{a}_i(\xi)/\mathscr{a}_0(\xi)} \approx 1$$

for ξ in the range between 0.1325 and 0.530 mm and $\Delta\xi$ ranging between 0.1325 and 0.265 mm. Recall that (equation (IV.3))

$$\mathscr{a}_i(\xi) = 6(1-\phi_i)\left(\int_\xi^\Xi \frac{\mathscr{P}_i(x)}{x^2}\,\mathrm{d}x + \frac{1}{\Xi}\right),$$

where $\mathscr{P}_i(x)$ is the CDF of distribution i. Therefore,

$$\mathscr{a}_i(\xi+\Delta\xi) = 6(1-\phi_i)\left(\int_\xi^\Xi \frac{\mathscr{P}_i(x)}{x^2}\,\mathrm{d}x - \int_\xi^{\xi+\Delta\xi} \frac{\mathscr{P}_i(x)}{x^2}\,\mathrm{d}x + \frac{1}{\Xi}\right) = \mathscr{a}_i(\xi) - 6(1-\phi_i)\int_\xi^{\xi+\Delta\xi} \frac{\mathscr{P}_i(x)}{x^2}\,\mathrm{d}x.$$

If $0.1325 \le \xi \le 0.530$, the CDF of each blend has the following form

$$\mathscr{P}_i(x) = \mathscr{P}_i(1.4)\mathscr{P}_{\text{fines}}(x), \quad 0 \le x \le 1.4,$$

where $\mathscr{P}_{\text{fines}}(x)$ is the CDF of -1.4 mm size fraction (see subsection 3.2 of Chapter III). Furthermore, the integral expression can be simplified using the mean value theorem:

$$\int_\xi^{\xi+\Delta\xi} \frac{\mathscr{P}_i(x)}{x^2}\,\mathrm{d}x = \mathscr{P}_i(1.4)\int_\xi^{\xi+\Delta\xi} \frac{\mathscr{P}_{\text{fines}}(x)}{x^2}\,\mathrm{d}x = \mathscr{P}_i(1.4)\frac{\mathscr{P}_{\text{fines}}(\tilde{\xi})}{\tilde{\xi}^2}\Delta\xi, \quad \xi \le \tilde{\xi} \le \xi+\Delta\xi.$$

Therefore, the ratio becomes

$$\frac{\mathscr{a}_i(\xi+\Delta\xi)}{\mathscr{a}_0(\xi+\Delta\xi)} = \frac{\mathscr{a}_i\left(\xi\right) - 6\left(1-\phi_i\right)\mathscr{P}_i(1.4)\frac{\mathscr{P}_{\text{fines}}(\tilde{\xi})}{\tilde{\xi}^2}\Delta\xi}{\mathscr{a}_i\left(\xi\right) - 6\left(1-\phi_i\right)\mathscr{P}_i(1.4)\frac{\mathscr{P}_{\text{fines}}(\tilde{\xi})}{\tilde{\xi}^2}\Delta\xi} = \frac{\mathscr{a}_i(\xi)}{\mathscr{a}_0(\xi)}\frac{1-\frac{6(1-\phi_i)\mathscr{P}_i(1.4)}{\mathscr{a}_i(\xi)}\frac{\mathscr{P}_{\text{fines}}(\tilde{\xi})}{\tilde{\xi}^2}\Delta\xi}{1-\frac{6(1-\phi_0)\mathscr{P}_0(1.4)}{\mathscr{a}_0(\xi)}\frac{\mathscr{P}_{\text{fines}}(\tilde{\xi})}{\tilde{\xi}^2}\Delta\xi}.$$

It remains to show that the second fraction in the last expression is close to one. First, note that the integral in the expression for the specific area can be split as follows:

$$\mathscr{a}_i(\xi) = 6(1-\phi_i)\left(\int_\xi^\Xi \frac{\mathscr{P}_i(x)}{x^2}\,\mathrm{d}x + \frac{1}{\Xi}\right) = 6(1-\phi_i)\left(\int_\xi^{1.4} \frac{\mathscr{P}_i(x)}{x^2}\,\mathrm{d}x + \int_{1.4}^\Xi \frac{\mathscr{P}_i(x)}{x^2}\,\mathrm{d}x + \frac{1}{\Xi}\right).$$

The first integral can be expressed via the CDF of fines:

$$\int_\xi^{1.4} \frac{\mathscr{P}_i(x)}{x^2}\,\mathrm{d}x = \mathscr{P}_i(1.4)\int_\xi^{1.4} \frac{\mathscr{P}_{\text{fines}}(x)}{x^2}\,\mathrm{d}x.$$

To simplify the notation, denote the parts of expressions that do not depend on the particular distribution as follows:

$$A = \frac{\mathscr{P}_{\text{fines}}(\tilde{\xi})}{\tilde{\xi}^2}\Delta\xi \quad \text{and} \quad B = \int_\xi^{1.4} \frac{\mathscr{P}_{\text{fines}}(x)}{x^2}\,\mathrm{d}x.$$

Therefore,

$$1 - \frac{6\left(1-\phi_i\right)\mathscr{P}_i(1.4)}{\mathscr{a}_i(\xi)}\frac{\mathscr{P}_{\text{fines}}(\tilde{\xi})}{\tilde{\xi}^2}\Delta\xi = 1 - \frac{\mathscr{P}_i(1.4)A}{\mathscr{P}_i(1.4)B + \frac{1}{\Xi} + \int_{1.4}^\Xi \frac{\mathscr{P}_i(x)}{x^2}\,\mathrm{d}x} = 1 - A\frac{1}{B + \frac{1}{\mathscr{P}_i(1.4)}\left(\frac{1}{\Xi} + \int_{1.4}^\Xi \frac{\mathscr{P}_i(x)}{x^2}\,\mathrm{d}x\right)}.$$

This expression can be used to estimate the change of the relative area with the change of ξ:

$$\frac{\mathscr{a}_i(\xi+\Delta\xi)}{\mathscr{a}_0(\xi+\Delta\xi)} = \frac{\mathscr{a}_i(\xi)}{\mathscr{a}_0(\xi)}\frac{1 - A\frac{1}{B + \frac{1}{\mathscr{P}_i(1.4)}\left(\frac{1}{\Xi} + \int_{1.4}^\Xi \frac{\mathscr{P}_i(x)}{x^2}\,\mathrm{d}x\right)}}{1 - A\frac{1}{B + \frac{1}{\mathscr{P}_0(1.4)}\left(\frac{1}{\Xi} + \int_{1.4}^\Xi \frac{\mathscr{P}_0(x)}{x^2}\,\mathrm{d}x\right)}}.$$

To avoid interpolation in integral approximations, the values of ξ aligned with the screening sizes of fines were chosen: $\xi = 0.125, 0.18, 0.25$, and 0.355 mm. The changes $\Delta\xi$ were also chosen to align with the screening sizes: $\Delta\xi = 0.18 - 0.125, 0.25 - 0.18, 0.355 - 0.25$, and $0.5 - 0.355$ mm. For GGS097 $\mathscr{P}(1.4) = 0$, which simplifies the ratio as follows:

$$\frac{\mathscr{a}_{\text{GGS097}}(\xi+\Delta\xi)}{\mathscr{a}_0(\xi+\Delta\xi)} = \frac{\mathscr{a}_{\text{GGS097}}(\xi)}{\mathscr{a}_0(\xi)}\frac{1}{1 - A\frac{1}{B + \frac{1}{\mathscr{P}_0(1.4)}\left(\frac{1}{\Xi} + \int_{1.4}^\Xi \frac{\mathscr{P}_0(x)}{x^2}\,\mathrm{d}x\right)}}.$$

Table IV.7: Ratio of the relative specific area change with the change of ξ.

ξ, mm	$\Delta\xi$, mm	$\frac{a_i(\xi+\Delta\xi)}{a_0(\xi+\Delta\xi)} \div \frac{a_i(\xi)}{a_0(\xi)}$, –						
		GGS150	GGS097	GGS075	GGS060	GGS050	GGS040	GGS025
0.125	0.055	1.10	1.22	1	0.989	0.983	0.978	0.972
0.18	0.07	1.10	1.20	1	0.988	0.981	0.975	0.968
0.25	0.105	1.11	1.21	1	0.984	0.975	0.968	0.958
0.355	0.145	1.11	1.19	1	0.982	0.972	0.963	0.952

Table IV.7 shows how the how the ratio

$$\frac{a_i(\xi+\Delta\xi)/a_0(\xi+\Delta\xi)}{a_i(\xi)/a_0(\xi)}$$

changes with ξ and $\Delta\xi$. It demonstrates that the specific area for each blend is proportional to the choice of the minimum size ξ. This is partially due to the same PSD of the fines across the blends (recall, it was only the overall fines content that was varied).

5. Average water content. Although the water content is not very sensitive to the change of the inlet flow rate in the range of 3–40 $\mathrm{L \cdot m^{-2} \cdot h^{-1}}$, it still changes. Furthermore, flow rates exceeding 20 $\mathrm{L \cdot m^{-2} \cdot h^{-1}}$ are above what is used in heap leaching operations. Thus, for this analysis the average value across the range of flow rates 2.4–21 $\mathrm{L \cdot m^{-2} \cdot h^{-1}}$ was used. The difference between the extremes and the average for each distribution does not exceed 11% in the extreme case and is below 4% in all but two cases. The most extreme variance is achieved with GGS150(P13) due to the overall low water content for this blend.

6. Model calibration. Comparison of relative water content (as a portion of water content for GGS075(P11)) and relative specific surface area is shown in Figure IV.15. It is evident that all experimental points fall close to a straight line. Furthermore, the the relation between relative specific area a_r and the relative water contnet ϑ_r is almost identical for all ratios Ξ/ξ. This is to be expected, since it was shown that the relative specific area a_r stays almost constant for all blends and for various choices of the minimum size ξ. Thus, the exact choice of the minimum size ξ is not critical. However, the ratio $\Xi/\xi = 50$ implies $\xi = 0.53$ mm which means cutting out even moderately sized particles. Furthermore, since the data for $\Xi/\xi = 100$ produces a slightly better fit compared to $\Xi/\xi = 200$, $\Xi/\xi = 100$ (with $\xi = 0.265$ mm) is used further below.

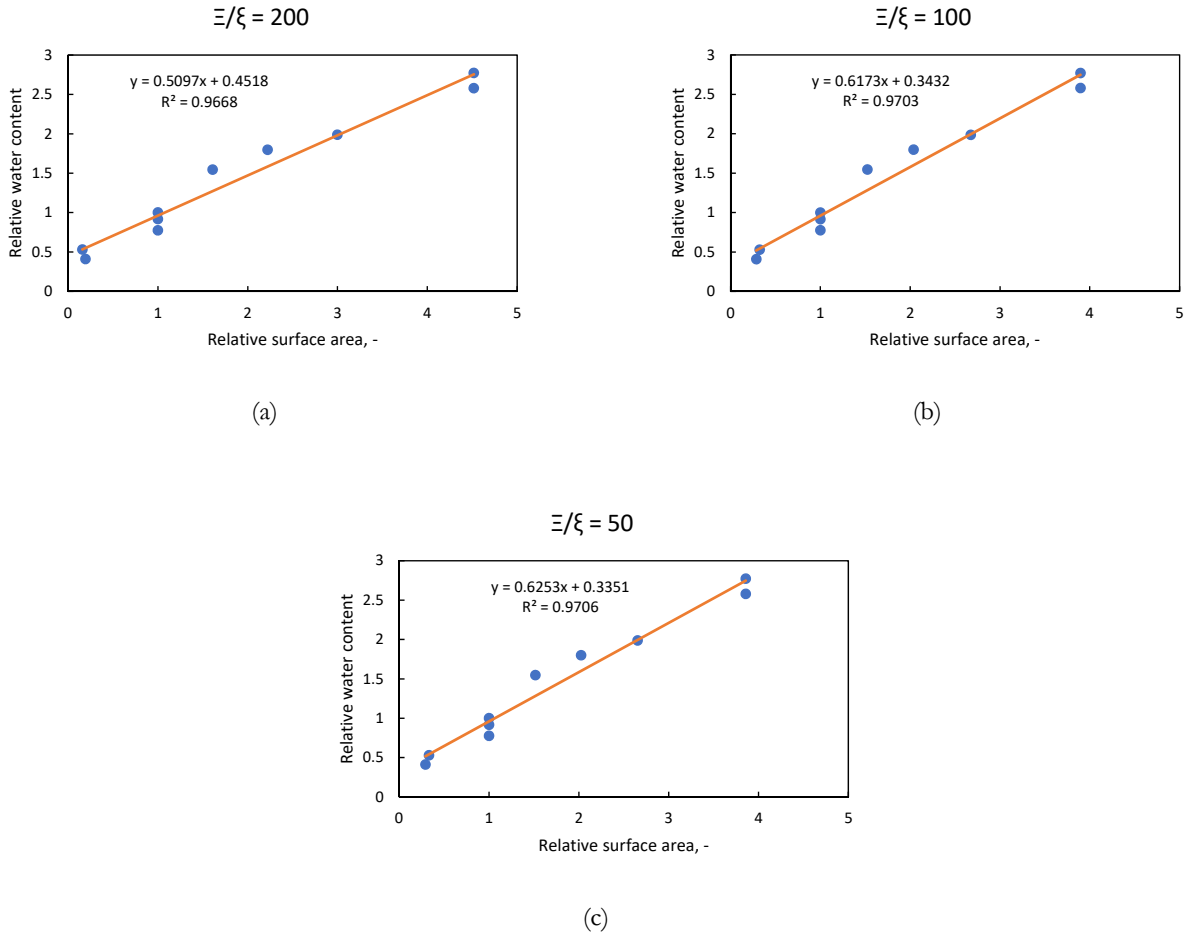

Figure IV.15: Comparison of water content and specific area for various Ξ/ξ ratios. All cases demonstrate a reasonable fit to a straight line.

The most important part of the result is nearly linear relation between a_r and ϑ_r. This validates the liquid hold-up model assumption of the liquid being spread on the surface of the particles at least for the experimental blends. Further validation against different ores is presented next.

7. Validation against independent data. Three extra points of comparison was found in the literature (Sheikhzadeh et al., 2005; de Andrade Lima, 2006; Dixon and Afewu, 2010) and two points were provided by industry. The latter are referred as "External K" and "External T" since permission to use the respective operation's name was not obtained. Comparison of the extra data with the experimental results shows a good agreement except for the extremely fine PSD of "External T" (Figure IV.16).

The levelling-off of the line for PSD with a large fines content can be explained by a reduction

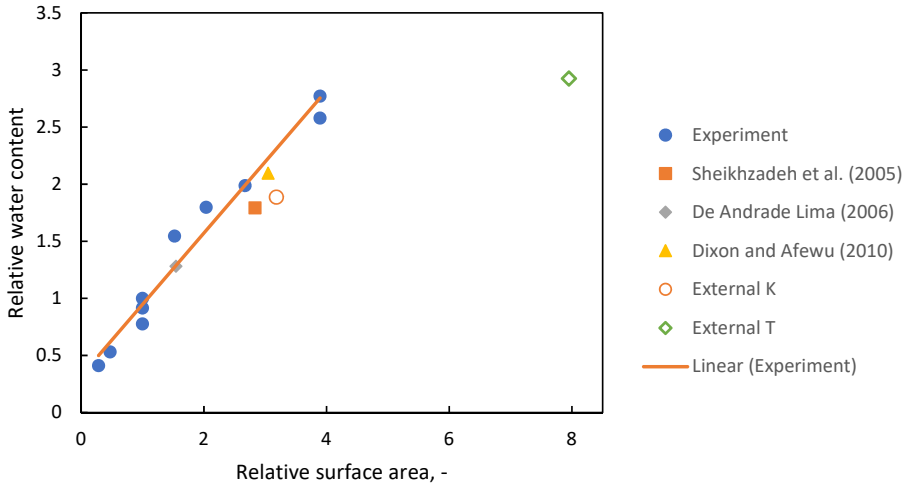

Figure IV.16: Comparison of the experimental data obtained in this study with the data from the literature and from industry using the cut-off size $\xi = 0.265$ mm.

in available pore space to be filled with liquid. Nonetheless, such PSDs are extremely unlikely as more typical PSDs found in heap leaching operations fall close to the GGS060 distribution. The data from de Andrade Lima (2006) presents an interesting case of mono-sized quartzite particles of size $+2$ mm -2.36 mm. The result of that study presented here corresponds, however, to an extremely high flow rate of 69 $\mathrm{L} \cdot \mathrm{m}^{-2} \cdot \mathrm{h}^{-1}$ (lowest in that study), whereas the water content at more typical 3–20 $\mathrm{L} \cdot \mathrm{m}^{-2} \cdot \mathrm{h}^{-1}$ flow rates would have been lower.

This data also enables estimation of the thickness of the water layer covering the particles, since it can be found as

$$\hbar = \frac{\mathcal{V}_{\text{water}}}{\mathcal{A}_{\text{solids}}} = \frac{\mathcal{V}_{\text{water}}/\mathcal{V}_{\text{total}}}{\mathcal{A}_{\text{solids}}/\mathcal{V}_{\text{total}}} = \frac{\vartheta}{a}.$$

Taking the average over all the data, average water layer thickness is $\hbar = 0.057$ mm with (population) variance $s^2 = 0.017$ (actual limits are 0.0255 and 0.0996 mm for the lowest and highest values). Although there is a considerable uncertainty in the value of $\hbar$, the small value of this thickness compared to the smallest particle size $\xi = 0.265$ mm confirms the use of water volume approximation (1) as $\mathcal{V}_{\text{water}} = \mathcal{A}\hbar$. It must be noted that a different choice of the value of ξ will result in a different value for

the water layer thickness. Furthermore, this calculation is made assuming full surface coverage of all ore particles by water. Experimental measurements of $\hbar$ using, for example, tomography techniques can provide indirect validation of the liquid hold-up model.

Overall, the above analysis showed that for a limited range of PSD and flow rates, both typical in heap leaching operations, liquid hold-up is proportional to the estimate of the particles' total spherical surface area. Furthermore, the predictions of this model are far more accurate compared to what is predicted by the Richards equation models. While this result shines some light on the heap hydrostatics, it does not say anything about actual flow. The following sections examine the flow based on residence time distribution (RTD) experiments.

§ 5. Solute transport results

1. The dataset from the first experiment. The first run of residence time distribution studies on columns GGS075(P11), GGS025(P12) and GGS097(P14) with the flow rate of 3 $\mathrm{L \cdot m^{-2} \cdot h^{-1}}$ indicated the discrepancy between the expected values and the measured results: the highest concentration achieved from columns GGS075(P11) and GGS097(P14) was lower than expected (Figures IV.17a and IV.17b). This discrepancy was attributed to a calibration error due to the high sensitivity of the concentration to small voltage changes at high concentration levels and possibly due to different solution temperatures during calibration and the actual experiment. To remove the discrepancy, measured concentrations were linearly scaled to fit within the limits of the expected values (see Figure IV.17c). This manipulation may have slightly affected the slopes of the F-curve. However, it did not affect the main features of the curve, such as initial time delay or time to achieve unity. Furthermore, the outflow from the column GGS075(P11) became blocked during the step-up stage of the experiment and thus its results were discarded.

2. Raw RTD results. Figures IV.18 and IV.19 show the F-curves of the RTD for experiments GGS097(P14), GGS075(P11), and GGS025(P12) at approximately 3 and 20 $\mathrm{L \cdot m^{-2} \cdot h^{-1}}$ flow rates, respectively. There is no data for GGS075(P11) at 3 $\mathrm{L \cdot m^{-2} \cdot h^{-1}}$ due to a temporary column blockage during the experiment. Small oscillations in GGS097(P14) and GGS025(P12) at 3 $\mathrm{L \cdot m^{-2} \cdot h^{-1}}$ on step-down was caused by the intermittent overflow in the conductivity cells that resulted in a larger area

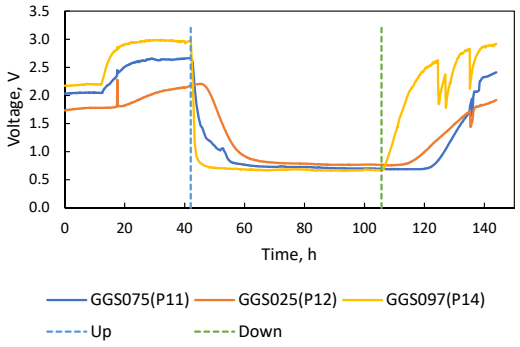

(a) Voltage

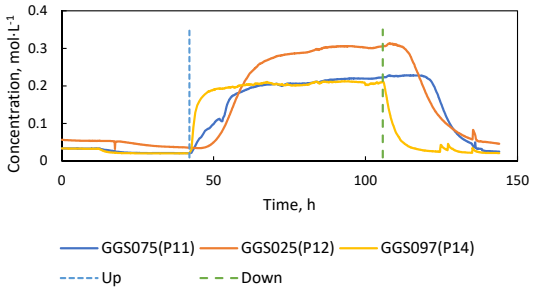

(b) Concentration

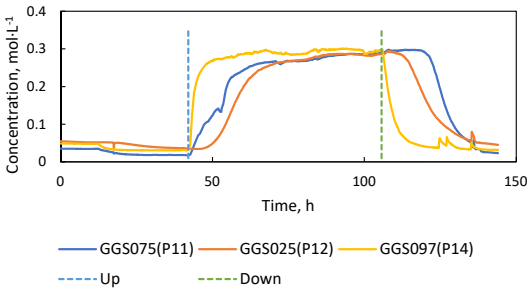

(c) Adjusted concentration

Figure IV.17: Conductivity measurement and its conversion to concentration for the first set of RTD studies.

of the electrodes being exposed to the solution and, as a result, a higher measured conductivity between the electrodes. The results show increased overall residence time with an increase in the amount of fines. Furthermore, GGS025(P12) at the low flow rate exhibits a time-delay typical of a plug-flow-kind reactor. However, no significant time delay is observed at the faster flow rate.

The fast flow rate of the first set of experiments is at least twice higher compared to a typical heap leaching flow rates. For the second set of experiments the flow rate of 10 $L \cdot m^{-2} \cdot h^{-1}$was used as a fast flow rate. Figures IV.20 and IV.21 show the results of the second set GGS075(P21)–GGS040(P24) at 3 and 10 $L \cdot m^{-2} \cdot h^{-1}$ flow rates respectively. Due to the smaller PSD difference, the trend of the increased residence time is only noticeable in transition from GGS075(P21) to GGS060(P22). Comparing step-up and step-down data from this and the previous series of experiments, it is apparent that

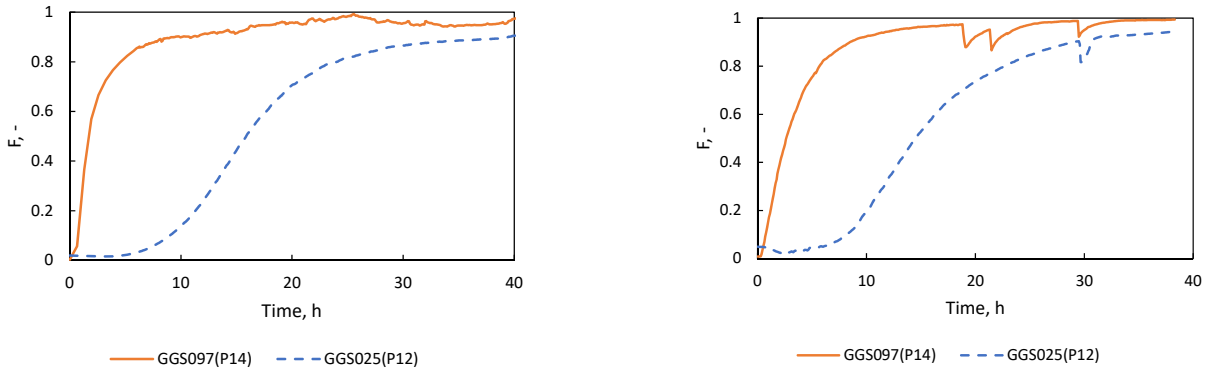

(a) step-up (b) step-down

Figure IV.18: F-curve for columns GGS025(P12) and GGS097(P14) at 3 L $\cdot$ m^{-2} $\cdot$ h^{-1}.

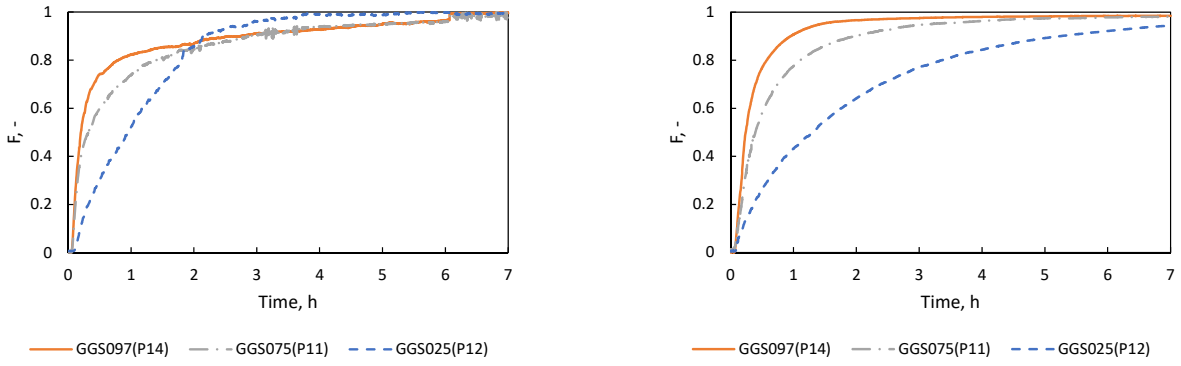

(a) step-up (b) step-down

Figure IV.19: F-curve for columns GGS075(P11), GGS025(P12) and GGS097(P14) at 20 L $\cdot$ m^{-2} $\cdot$ h^{-1}.

step-up data is noisier. This can be attributed to higher uncertainty in converting voltage to concentration at low voltage and respectively high concentration points: a small variation in voltage results in a large variation of concentration. Hence, the results of the step-down experiments were chosen for further discussion.

A deeper comparison of the data is not possible in its current form as different columns have different volumes due to slumping and different water contents due to different fines content. This, for example, may result in a larger residence time for some columns not only due to differences in PSD or flow rates but also due to different bed volumes. Homogenisation of the data by introducing

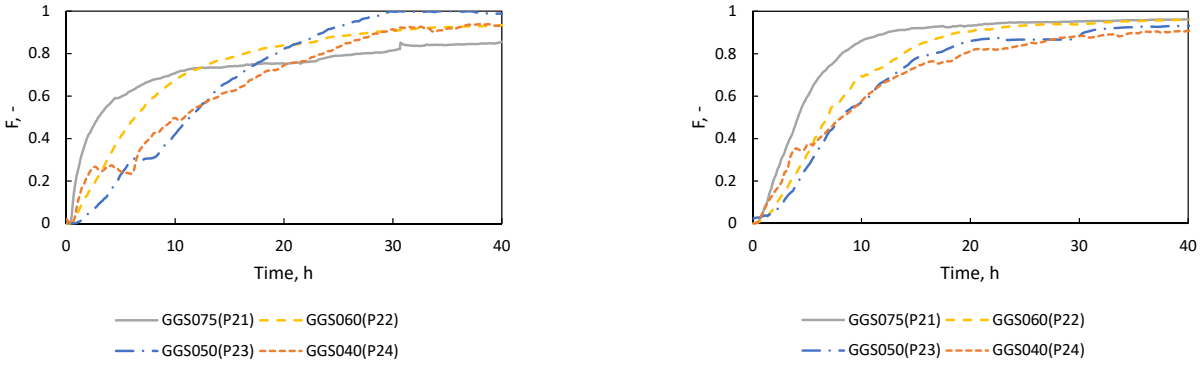

(a) step-up (b) step-down

Figure IV.20: F-curve for columns GGS075(P21)–GGS040(P24) at 3 $\mathrm{L \cdot m^{-2} \cdot h^{-1}}$.

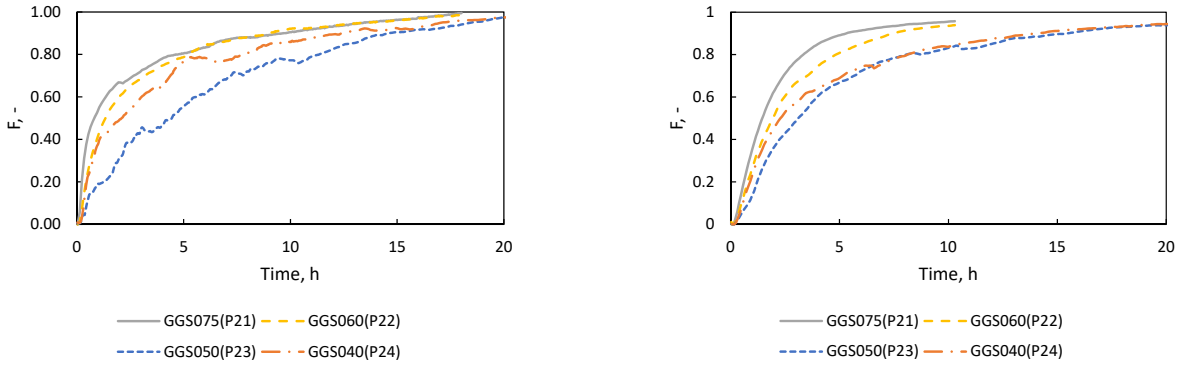

(a) step-up (b) step-down

Figure IV.21: F-curve for columns GGS075(P21)–GGS040(P22) at 10 $\mathrm{L \cdot m^{-2} \cdot h^{-1}}$.

unitless time is the first step towards a more meaningful comparison.

3. Dimensionless form. The dimensionless form of the results is derived using volumetric flow rate Q and liquid volume in the column $\mathcal{V}_{\text{water}}$ (true volume of the reactor) to produce dimensionless time

$$\tau = \frac{Q}{\mathcal{V}_{\text{water}}} t.$$

F-curves in this form for all step-down experiments (all blends and all flow rates) are shown in Figure IV.22. With a notable exception of the GGS025(P12) at 3 $\mathrm{L \cdot m^{-2} \cdot h^{-1}}$, F-curves for all the experiments indicate a mixed-type of the reactor behaviour. Furthermore, they all fall in a narrow

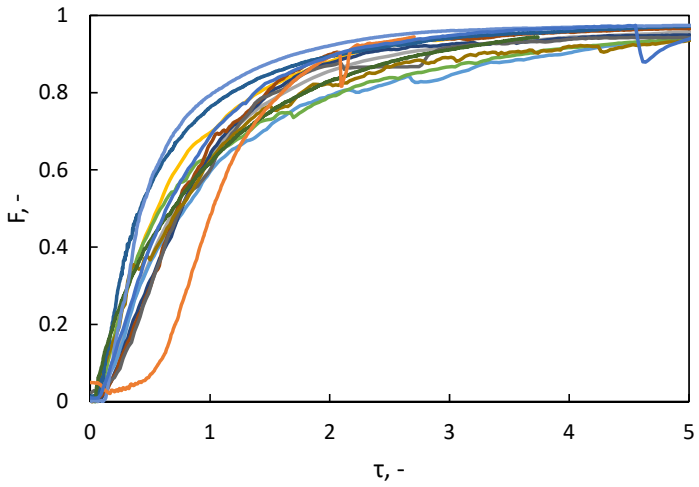

Figure IV.22: Unitless form of F-curves for all step-down experiments. No legend is given as the main purpose is to demonstrate the congruence of these curves.

band, indicating little variation between experiments with different PSD and flow rates (in relative terms of the unitless time, of course).

4. Comparison with the literature. A proper comparison of RTD results requires a few key pieces of information: F-curve, inlet flow rate and the liquid volume inside the rock matrix. It is uncommon to find all three pieces of information. Three studies have been identified to provide all the necessary data: Bouffard and Dixon (2001), de Andrade Lima (2006) and Dixon and Afewu (2010). The work by de Andrade Lima (2006) involves mono-sized particles and extremely high flow rate and, thus, is not discussed. Although Bouffard and Dixon (2001) did not report the water content, from the data that was presented, the water content can be estimated to be either $\vartheta = 0.13$ or $\vartheta = 0.17$. Figure IV.23 shows the comparison of the results by Bouffard and Dixon (2001) using both estimates of the water content and Dixon and Afewu (2010) with the selected results from this study. The experiments in both Bouffard and Dixon (2001) and Dixon and Afewu (2010) were conducted in a taller column (height of 0.584 m and 1 m respectively), hence there is more visible initial delay. The fact that this delay is not proportional to the overall residence time points out to a change in the flow dynamics (see subsection 2.4 of Chapter V on the discussion of future work to scale up the present experiments). Furthermore, the slope of the F-curve from those studies is noticeably steeper

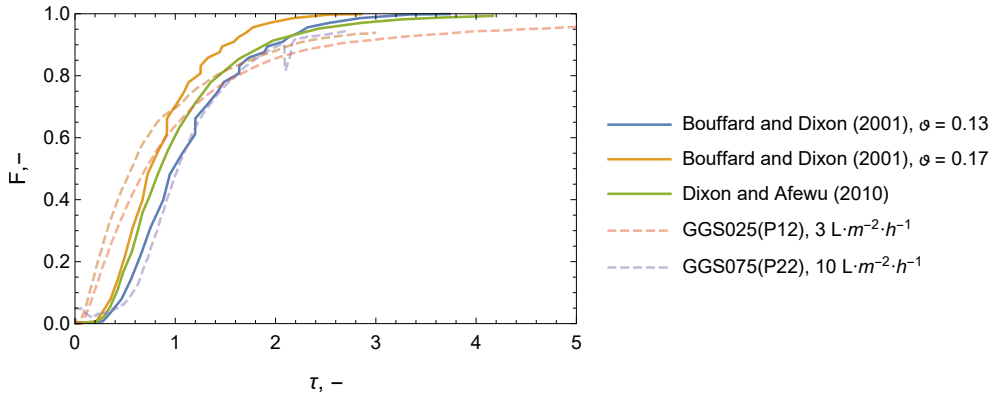

Figure IV.23: Comparison of the RTD experiments results with the results of Bouffard and Dixon (2001) and Dixon and Afewu (2010).

compared to the results of the present study. Nonetheless, all the results still fall close to each other, suggesting similar hydrodynamics between the experiments.

§ 6. Discussion of solute transport

1. Advection-dispersion model (ADM) ADM cannot successfully fit experimental data: for small Péclet numbers ADM predicts fast back-mixing, whereas for large Péclet numbers there is too big a delay in the rise of the F-curve, i.e. the plug-flow component of the flow is too large (see Figure IV.24). Although a more complex two-dimension ADM or a an ADM expanded to account for flowing and stagnant liquid may provide a better fit (Bujalski et al., 2003), this exercise was not pursued since the experimental data does not contain enough information to validate these models. However, it is worth noting that a shallow slope of the experimental F-curves may be explained by two-dimensional spread of the tracer solution.

2. Single CSTR and 2-CSTR in parallel. The single CSTR model shows a good general agreement with the experimental results (Figure IV.25). However, on average it underestimates the time it takes to reach $F \approx 1$. 2-CSTR in parallel (see subsection 8.1 of Chapter II) provides a similar fit with parameters $\mathcal{V}_1/\mathcal{V} = 0.8045$ and $Q_1/Q = 0.9316$ resulting in the equation

$$F(\tau) = 1 - 0.9316 \exp(-1.158\tau) - 0.0684 \exp(-0.1499\tau).$$

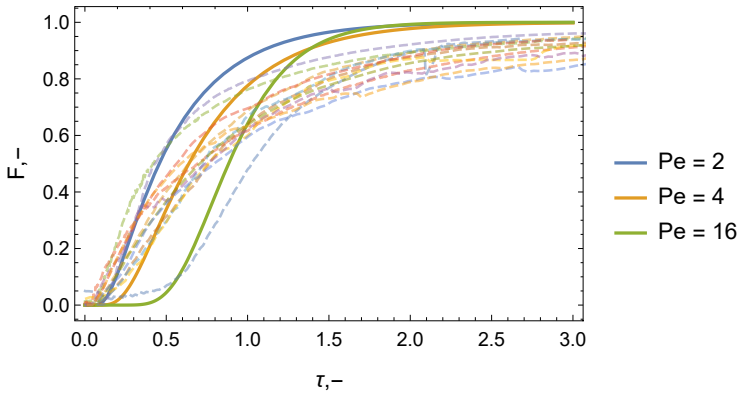

Figure IV.24: Comparison of ADM with experimental data for various Péclet numbers.

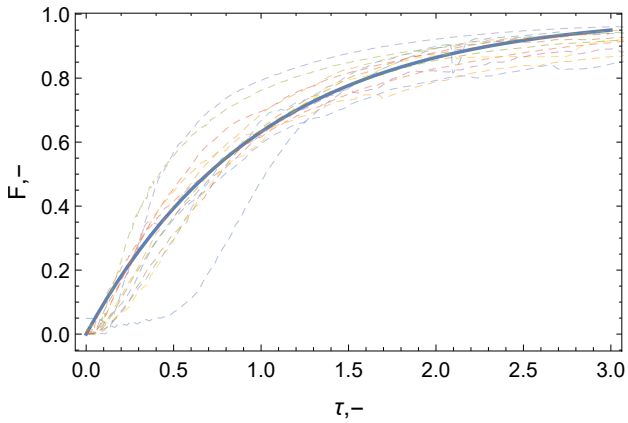

Figure IV.25: Comparison of a single CSTR model and RTD experiments.

These parameters were found through the minimisation of the following penalty function:

$$\mathscr{P}_{\text{2-CSTR-P}}(\mathscr{V}_1/\mathscr{V}, Q_1/Q) = \sum_{\text{experiments}} \left(\sum_i \left(F_{\text{model}}\left(\mathscr{V}_1, \mathscr{V}, Q_1/Q, t_i\right) - F_{\text{experiment}}(t_i) \right)^2 \right).$$

The minimisation was performed by the `NMinimize` function of the *Mathematica* package, resulting in $\mathscr{P}_{\text{2-CSTR-P}} = 32.48$ using a total of 8151 experimental data points. As can be seen in Figure IV.26, the overall difference between single CSTR and 2-CSTR models as applied to this experimental data is insignificant. Therefore, it can be concluded that solute flow in short columns resembles the flow typical for single CSTR. This begs the question: *How does the system that has no mixing or at best localised micro-mixing exhibit near-perfect mixed behaviour?*

3. E-curves, being the derivatives of F-curves, provide more detailed information regarding the residence time distribution. The reconstruction of the E-curves from the F-curves, however, is not

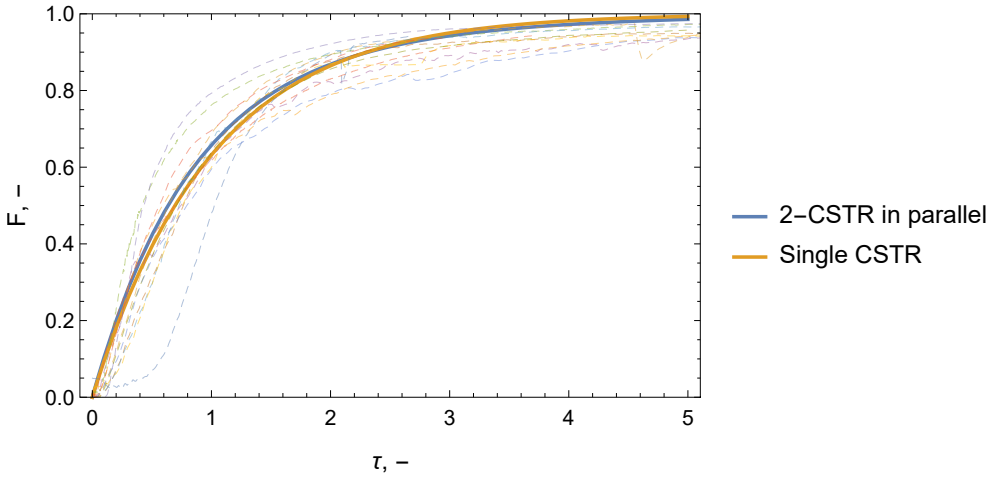

Figure IV.26: Comparison of 2-CSTR in parallel, single CSTR and experimental data.

trivial since any noise present in the data defining an F-curve is amplified when the derivative is taken. The following procedure was followed to filter the noise from the F-curves and to get the E-curves:

1. A moving median over 20 data points up and downstream (radius 20) was applied;
2. This was followed by the application of the Gaussian filter with the same radius 20;
3. Then the data was interpolated using cubic splines;
4. The derivative of the interpolated function was taken;
5. The set of data points was produced from the derivative function between the interpolation bounds with step size of $\Delta\tau = 0.01$;
6. This data was filtered using moving median average with radius 10;
7. The filtered derivative data was interpolated using cubic splines to produce the E-curve.

All the calculations were performed using the *Mathematica* package. The result of applying this procedure to all step-down data sets is shown in Figure IV.27. Due to a large amount of filtering used, the shape of the E-curves must be viewed qualitatively. It is evident that most of the E-curves (about 2/3) form a bundle with the maximum around $\tau = 0.5$ and a tail stretching to $\tau = 2.5$ (Figure IV.28). There are four outlier curves that have peaks that are higher and shifted (Figure IV.29).

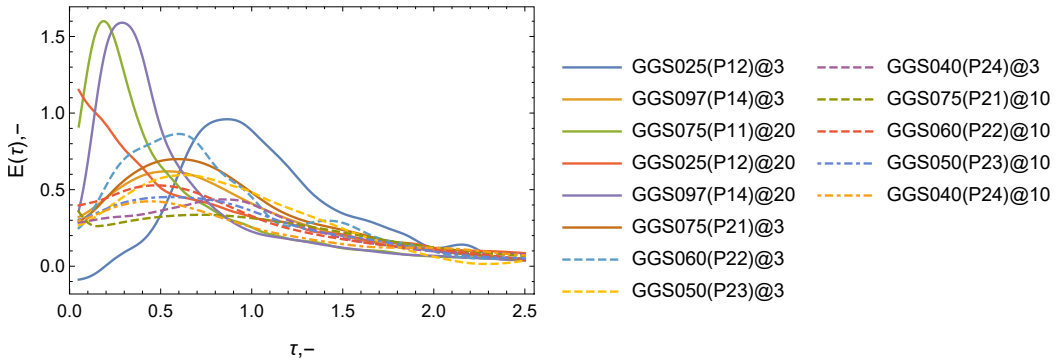

Figure IV.27: *E*-curves for all step-down experiments.

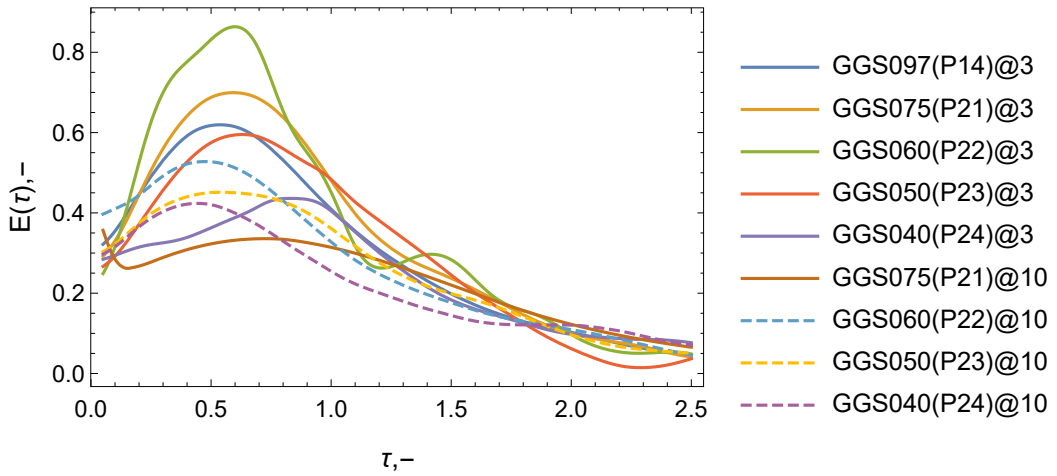

Figure IV.28: The selection of *E*-curves forming a bundle.

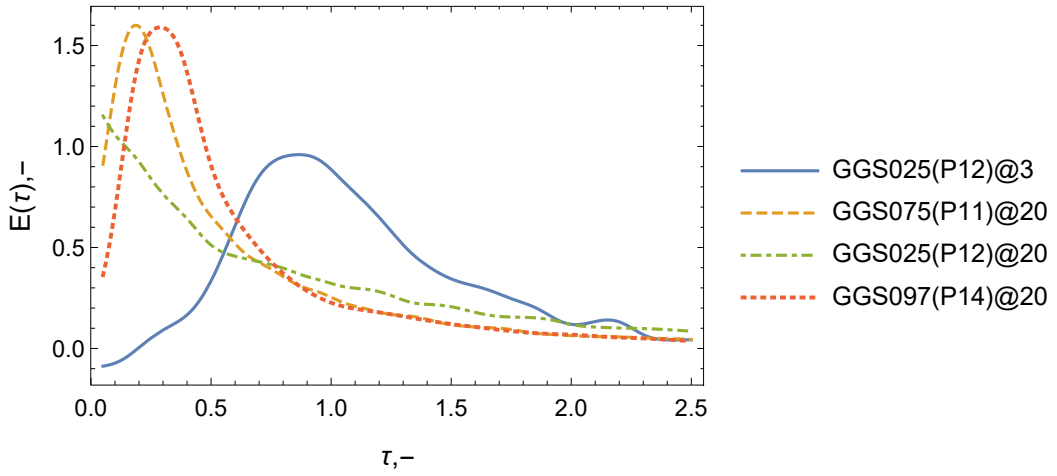

Figure IV.29: The outliers among the *E*-curves.

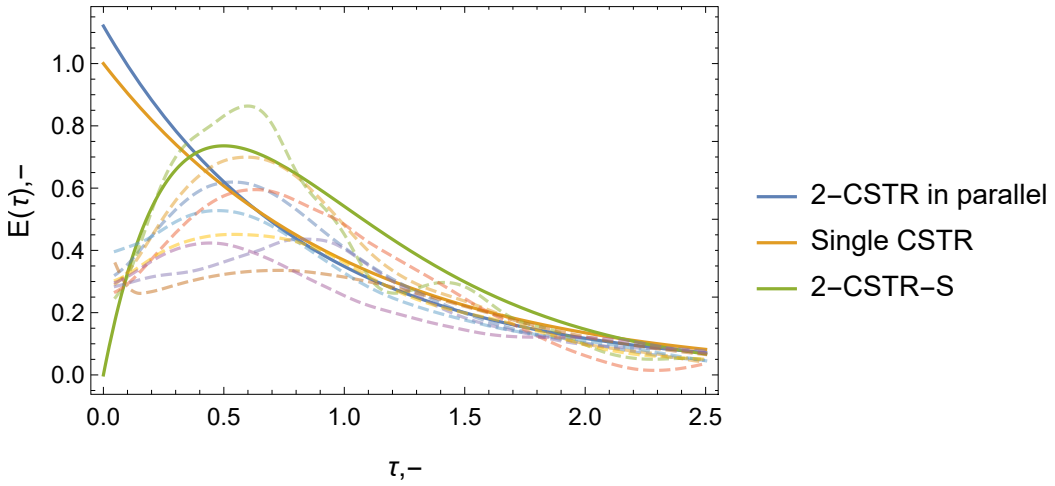

Figure IV.30: Comparison of the experimental E-curves with the selected models.

Comparison of the E-curves with the selected models is shown in Figure IV.30. Experimental E-curves emphasised the effect of a slight initial delay, which makes 2-CSTR-S model (see subsection 8.3 of Chapter II) a better fit at lower values of τ. However, a single CSTR model fits better at larger τ. It can be concluded that although the flow through packed rock beds exhibit some features typical of a mixed reactor, it would be a mistake to consider it ideally-mixed.

4. PFRP to rescue. The mixed behaviour is only observable in these experiments because there are no reactions between solutes and solids (see section §9 of Chapter II). It is likely that in a densely packed bed such as heaps the actual flow occurs through a number of channels of various length with these channels connecting and splitting at different points throughout the bed, creating an illusion of mixing. PFRP can be postulated to be the right model for such a flow. While CSTR and compartment models provide a conceptual view of the liquid particle movement, the foundation of the PFRP model, the distribution of the channels, maps directly to a physical picture of the liquid droplet movement. It must be noted that PFRP models a possibly multi-dimensional flow phenomena using a simplified one-dimensional formulation. Validation of this model assumptions requires carefully obtained experimental data on a reacting system with known RTD and known basic reaction kinetics which lies beyond the scope of this work.

While it is not possible to conclude the validity of PFRP without further experimentation, an alternative view on the flow process can be offered. One deficiency of the PFRP is that the liquid entering a short channel stays in this channel, it cannot exchange with liquid in a longer channel.

Conceptually, however, it is possible that this can happen. The following model demonstrates how this concept can be realised.

§ 7. Potential route forward: stochastic pore model

Considering the physical picture of the flow process (see Figure I.3 on page 18), a more direct approach to flow may become more useful. In this approach individual liquid "particles" (droplets) are moving through the network of pores. Diffusion-type models, including flow through porous media, are statistical limits of this concept. These limits, however, can only be achieved if the number of pores and particles are very large. This is not a problem for a classical diffusion process where each particle is a molecule. The case of solution flow in heaps and dumps, however, is different: the coarseness of the rocks limits the number of pores. This limitation is exacerbated in column experiments which are orders of magnitude smaller in all dimensions. Thus, while a pore-scale model does reduce to a diffusion-type form "when $N \to \infty$", it may not do so when the number of pores or liquid particles is restricted.

This section shows an approach of constructing a model that takes this into consideration. This model is inspired by pore network models (Sahimi, 1993), but not actually based on them. In particular, the model postulated here calculates the liquid particle movement directly, whereas the latter requires some form of momentum balance. This way this model is closer to cellular automata, such as Conway's Game of Life (Wolfram, 1982). While direct calculation of the movement simplifies computation, it introduces some irregularities that need to be resolved before this model can be fully applicable. Nonetheless, a stochastic pore model presents a framework within which future models may be developed.

1. Domain: lattice. As with numerical methods for continuous models, this model splits the domain into finite parts. The resulting structure is essentially a lattice with sites and bonds. Graphically, a site is a point connecting bonds that are represented by lines. Mathematically, the lattice is just a graph whose vertices are sites and edges are bonds.

A bond represents a single pore within the domain. There are three kinds of bonds: *body*, *throat* and *drain*. A body pore has characteristics of a typical wide pore: it easily accepts a liquid particle, it has

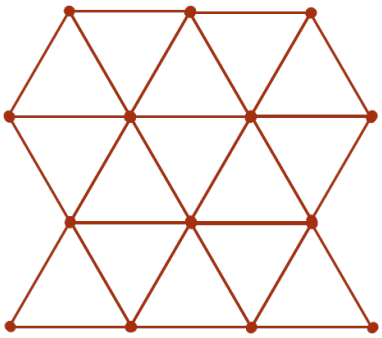

Figure IV.31: Graphical representation of the domain lattice with each line being a bond and each point being a site.

high capacity, and it easily expels the liquid. Furthermore, it is unable to draw the liquid "upwards", against gravity. A throat pore is a thin pore which would have high (in absolute value) capillary pressure. Thus, it is able to retain more liquid particles before expelling them, but it has a lower capacity and liquid does not easily enter a dry throat pore. Finally, drain pores have characteristics of body pores with the exception that they do not expel liquid into other bonds. Instead, liquid that reaches drain pores is taken out of the domain.

Sites are the points of bond connection: a bond can only take a liquid particle from the bond with which it shares a common site. Bonds can only be connected at their ends.

The lattice is formed by domain triangulation. Potentially it can be done in numerous ways, resulting, for example, in bonds that span the whole domain. Since this model exists for demonstration purposes only, a regular lattice is built. The domain is assumed to be rectangular. One side, which is assumed vertical, is split into layers. On each layer, site points are placed: N points on even layers and $N-1$ points on odd layers. On every even layer the first and the last site is placed on the left and the right edge of the rectangle. Other sites are equally distributed on the line with distance h between them. On odd layers the first and the last site are shifted into the domain by distance $h/2$. With this site placement, it is easy to connect sites between the layers by bonds of equal length. Furthermore, if the distance between the layers is chosen as $\sqrt{3}h/2$, all the bonds will have length h (Figure IV.31). This construction signifies one important aspect about the bonds: they may differ in type and orientation, but their lengths do not affect their properties.

After the sites are placed, each site is connected with a bond to its nearest neighbours, forming a regular hexagon for all internal sites. Throat and body bond types within the lattice are assigned

randomly, potentially with unequal probabilities. The bottom pores are assigned the drain type.

2. Time is discrete: there are two definite moments i and $i + 1$ with the specified system state. Transition from the state at time i to the state at time $i + 1$ occurs instantaneously.

3. Irrigation is simulated by placing some number of liquid particles in specified bonds at the top of the lattice at each time point. These otherwise normal body or pore bonds are referred to as *entry* bonds. Different flow rates are modelled by changing the number of these particles. By changing the entry bonds, one can model, for example, a single drip emitter or uniform irrigation.

4. Simulation : rules. At each time step each liquid particle within the lattice is given an opportunity to move. First, particles are introduced through the entry bonds and taken away from the drain pores. Then, depending on the bond type and current bond saturation, each particle can move to one of the neighbouring bonds or stay in its current position. Each particle is allowed to move more than one bond at the time, but the probability of it moving decreases with the number of its movements within a step.

Particle movements are directed by a set of rules. Each rule is essentially a probability or a coefficient associated with each action: probability of expelling from the current bond combined with the probability of being accepted into a particular connecting bond, coefficient controlling the decrease of expelling probability if the particle has moved multiple times in one time step, and the coefficient controlling the bias for the downward movement. An action is chosen probabilistically for each particle based on its current state. This state comprises the state of its current bond (type of the bond, current number of particles in the bond), the state of the neighbouring bonds, and the number of moves this particle has already made in this time step. Once the current particle cannot move any further, the simulation proceeds to the next particle. Table IV.8 shows an example of parameters for the stochastic model. In this example, each bond has four possible states, 0–3, defined by a states-particle vector. State 0 is associated with no particles in the bond. State 1: one particle. A bond has state 2 if there are 2–5 particles. State 3 if it has 6 particles or more. Accept and expel probability coefficients are associated with each bond type and state: the higher the coefficient, the higher the probability of the action taking place. The moving direction factor modifies the probability of the movement creating

Table IV.8: Example of stochastic model parameters.

Rule	Pore type		
	Throat	Body	Drain
Accept probability coefficient	[5, 100, 100, 0]	[20, 80, 20, 0]	[20, 80, 20, 0]
Moving direction factor	left: 1, right: 1, up: 1, down: 1	left: 2, right: 2, up: 0.1, down: 5	N/A
Expel probability coefficient	[0, 0.02, 5, 50]	[0, 1, 50, 100]	[0, 0, 0, 0]
Other rules			
States-particles vector	[0, 1, 2, 2, 2, 2, 3]		
Moving probability factors	[1, 1, 1, 1, 1, 1, 1/2, 1/2, 1/5, 1/10, 1/30, 1/100]		

a bias towards downward movement. Finally, moving probability factors modify the probability of a particle to move if it has moved before.

There is some flexibility in choosing the rules: capacities of bonds, exact probabilities of expelling and accepting, coefficients that govern downward bias of the movement, and the possibility of multiple moves. It is expected that by changing these parameters, different flow pictures will emerge.

5. Particle residence time. This model possesses an important advantage over a classical flow-through-porous-medium model. It can establish residence time of liquid particles. This is done by marking each liquid particle entering the domain with the current time. At the time when the particle is taken out at the drainage, the difference between the current time and the particle entry time is taken. This allows the investigation of the residence time distribution in the presence of the intermittent flow.

6. Results. The results shown here are qualitative. The model shows the spread of liquid within the domain (Figure IV.32). In contrast to the classical flow through porous medium theory, the percolation can occur earlier (especially in presence of a large proportion of body pores). Furthermore, the model shows slow gain in overall liquid hold-up over a long period of time (Figure IV.33). Although the exact flow pattern is dependent on a particular set of parameters, some qualitative observations can be made. First, the dynamics of the liquid particles accumulation in the lattice during infiltration is

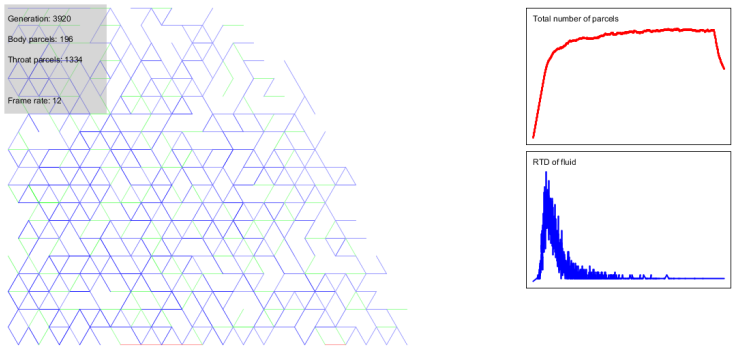

Figure IV.32: Screenshot of the running program.

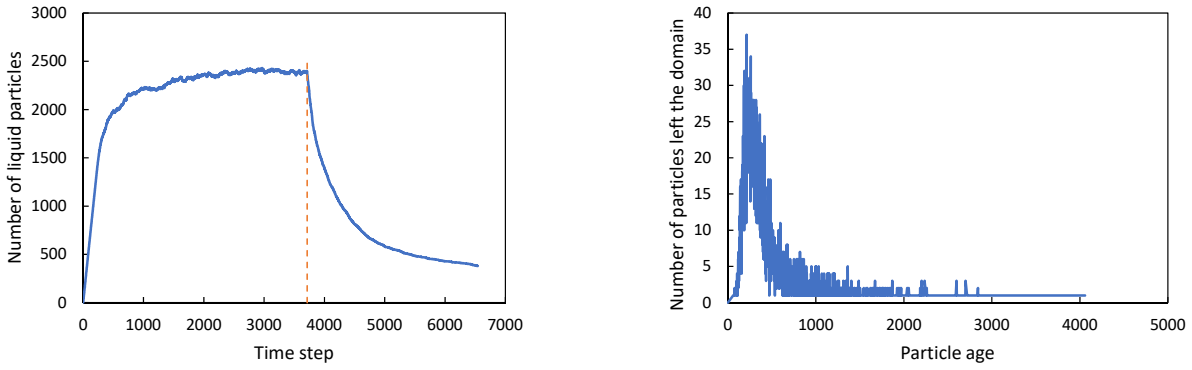

(a) (b)

Figure IV.33: Example of the stochastic model results: (a) liquid hold-up and (b) RTD. Flow was stopped at time step 3714.

similar to the dynamics observed with the infiltration experiments of previously non-flooded columns GGS075(P33) and GGS025(P34) (see subsection 2.3, except the experiments were running under the intermittent irrigation). Secondly, the shape of the RTD curve of the liquid particles (E-curve) is similar to the shape observed during the RTD experiments (subsection 6.3). However, the position and the height of the peak of the model curve is different. Finally, the curve showing the loss of the liquid particles has a shape similar to the final drainage curves. However, currently it is uncertain if it is possible to fit the models parameters to fit the experimental curves quantitatively.

The model in its current form suffers from two drawbacks. First, it is impossible to prevent over-filling of pores: the pore acceptance probability depends on its status at the previous time step and, as a result, multiple liquid particles can land there resulting in over-filling. If the pore's state is changed

in place for each droplet, there is a potential to create bias in the flow. For example, if the pores iterate from left to right, there will be additional flow to the right of the lattice as pores on the left side become full. The second problem is slow processing time: it is orders of magnitude slower compared to running the Richards equation model: a single simulation runs for minutes compared to seconds. This can be remedied by choosing data structures with faster read and write access to represent pores and rules, and by algorithm parallelisation. Currently, hash-maps built on top of prefix trees ("tries") are utilised due to their ease of use (especially in Clojure, the programming language in which the model is implemented). However, tries are much less performant compared to plain arrays: the program profiling indicated that most of CPU time is spent looking up the items in tries. Furthermore, the transition from one time step to the next is independent of the order in which the pores are traversed. Thus, algorithm parallelisation can significantly boost the performance.

As this approach to flow modelling in heaps is new, there is a large amount of work required to test its viability. First, the range of rules needs to be systematically tested to build up the idea of the spectrum of flow patterns possible with them. Secondly, the rules must be calibrated for particular cases of experimental data. And finally, the model must be validated against scaled-up experimental data. This process, however, lies beyond the scope of this work.

Chapter V

Conclusions

> *I have yet to see any problem, however complicated, that when looked at in the right way did not become still more complicated!*
>
> — Anderson's law

Wider commercial application of heap leaching is still hindered by low recovery rates. Solution flow in heaps is the key phenomenon controlling the mineral dissolution and the transport of the products out of a heap. Application of the established theory of flow based on the Richards equation requires careful model calibration to establish hydraulic parameter values. These values are case specific and no data exists that can support some material model linking them to easily measurable ore and/or packing properties. This research project aimed to establish a reliable simplified approach to find flow properties based on measurable properties. Particle size distribution (PSD) and the flow rate were identified as key parameters. Examination of existing models and experimental data resulted in a re-developed approach for solution flow understanding.

The Richards equation model was examined numerically and analytically by introducing various simplifications, such as steady-state or domain uniformity. Numerical solution provided validation for analytical results. This analysis laid the foundation for the subsequent experimental work. Steady-state liquid hold-up, infiltration and drainage dynamics, and solute flow in packed rock beds were studied experimentally. Gravimetric and residence time distribution studies were performed. The link between PSD and hydrodynamic response was examined by preparing artificial blends typical for heap leaching. To strengthen the connection to industrial application, low flow rates were the main focus of this investigation.

The Richards equation model was found to be inadequate to represent the flow in packed rock beds in the context of heap leaching. Instead, an effective model predicting liquid hold-up based on PSD was formulated and validated. The solute flow was found to be uniform in the dimensionless form across PSDs and irrigation rates. The following section details these findings.

§ 1. Key findings

All models are wrong, but some are useful.

— George Box

1. The Richards equation models. The key finding regarding application of Richards equation to heap leaching is the non-uniqueness of hydraulic parameters values fitting the model (subsection 3.2, Chapter IV). This is primarily due to the fact that experiments were conducted at low saturation levels as to be expected in heaps. However, it has also emphasised another problem with the Richards equation. The objective of this model is to predict the flow and liquid distribution based on the infiltration or drainage conditions (boundary conditions) and hydraulic properties of the solid matrix. The experimental results have shown that in the range of irrigation flow rates typical for heap leaching, the flow is practically independent of the rate (subsection 2.1, Chapter IV). While this result is qualitatively consistent with the solutions of the Richards equation (sections §3 and §4 of Chapter II), it means that the model is not useful for quantitative prediction of saturation based on the infiltration or drainage conditions. Furthermore, experimental results (conducted at flow rates typical to heap leaching) failed to provide a consistent connection between PSD and hydraulic parameters.

2. Liquid hold-up model. A direct method of estimating the liquid hold-up based on PSD was proposed (see §4, Chapter IV). This model assumes: (a) the liquid covers a fixed portion of all ore particles with the same liquid layer thickness and (b) particles are spheres. Despite this model being quite crude, it has been demonstrated that it not only fits the experimental data obtained in this study but it also fits reasonably well with other data from the literature. The use of this model can help to reduce the amount of test work performed by industry in designing heap leaching operations.

3. Solute flow. RTD results in a dimensionless form have demonstrated the uniformity of the flow properties across PSD and irrigation flow rates. Although they have shown the distribution typical of the combination of two-CSTRs-in-series and a single CSTR it is in contradiction to the physical reality as there is no forced mixing. An alternative model (PFRP) based on channel distribution was proposed. This model receives RTD data and reaction kinetics as inputs and aims to predict mineral conversion. The PFRP model is a conceptual simplified one-dimensional model that potentially incorporates two- or three-dimensional effects present in the experimental data. A further extension on PFRP that incorporates two-dimensional effects more explicitly was formulated — the stochastic pore model. This model combines two-dimensional network of channels and simple discrete time dynamics to produce the liquid flow pattern. Validation of these new models lies beyond the scope of this thesis and is a part of the proposed future work.

§ 2. Future work

1. Further validation of liquid hold-up model. Model improvements. Currently available data in the literature enables only limited model validation. There are two key pieces of information that are necessary to get a result from the model: PSD of ore and steady-state water content during irrigation. There are very few studies where both of these pieces are presented (Sheikhzadeh et al., 2005; de Andrade Lima, 2006; Dixon and Afewu, 2010). There are two routes by which further validation can be approached. First, the study can replicate this work with artificial blends but using a different kind of ore. This approach would also test the effect of mineralogy. Secondly, the study can be performed on an ore with the PSD as used in operation. One aspect of this model validation that requires a special attention is the choice of the minimum size ξ. The current study found that the choice is not critical for the blends that was used in the study. However, this just might be a result of how the blends were made. Thus, further experimental work with various values of ξ but with different blends is required.

This project focused on PSD alone. The effects of the presence of clay, mineralogy, and particle morphology were deliberately disregarded. It is possible, however, that the liquid hold-up can be considerably affected by these attributes. This is especially true for the presence of clay due to molecular level interaction of pore water with the clay matrix, resulting in such effects as swelling. Thus, further experimental work incorporating these effects is necessary.

2. PFRP validation. PFRP was formulated as an explanation of the results of RTD experiments (see §9 of Chapter II and subsection 3.4 in Chapter IV). The validity of the model, however, can only be established by introducing a reaction effect into the study. One possible way of conducting the study would be doping the ore with some chemical that is not easily soluble but can be targeted by a specific reagent with known reaction kinetics. For example, gold or silver can be used with cyanide as a reagent. Classical RTD studies can then be performed using an inert tracer (e.g. potassium nitrate as in this study). These studies would provide the F-curve for the PFRP model. This is then followed by introduction of the reagent into the irrigation solution. The product and reagent outflow from the reactor over the time will provide necessary data to validate the PFRP model.

3. Stochastic pore model improvements. The stochastic pore model presented in section §7 of Chapter IV aims only to show a possible approach to flow description. As it has been already mentioned, the current model implementation may result in pore over-saturation and its performance is slow. The former can be addressed by changing the way how liquid particles find their new position in the lattice. Instead of each particle finding its position independently, an approach similar to the Lattice Boltzmann Method (LBM) may be used in which some form of energy is formulated and it is minimised at each time step (Pan et al., 2004). The performance issue can be resolved by parallelisation of computation and performing it on a graphical processing unit (GPU) or a cluster. Another model extension would be the introduction of an unstructured lattice, enabling a single pores to connect sites at the top and at the bottom of the lattice. Finally, the flow description, obtained from the stochastic pore model, needs to be connected with an appropriate reaction model to be relevant to heap leaching.

4. Addressing experimental caveats. These studies were confined to the scale of 30×20 cm columns. The RTD experiments results are directly affected by the scale, as it is expected to see a significant initial time delay for a taller column. Furthermore, both liquid flow and solute transport experimental results may be affected by the two- or three-dimensional nature of the flow. It is necessary, therefore, to conduct the experiments at a larger scale.

Initial flooding of the columns presents another experimental caveat that can be addressed in future work. One possible way to introduce the initial moisture content into the packing is to perform initial slow irrigation before carrying out main experimental program.

5. Initial infiltration, final drainage and hysteresis. The core experiments of this study have avoided the question of initial infiltration, during which the water needs to go through dry rock, by flooding the columns. However, initial infiltration is an important aspect of heap leaching operations. While the liquid hold-up model can estimate the steady-state water content in the heap, it is still uncertain if this hold-up is practically attainable. Furthermore, drainage results of this study failed to find any correlation between ore properties and drainage dynamics. Hence, it warrants further investigation. Linked to initial infiltration and drainage is the question of hysteresis, as its effects may be exploited by using intermittent irrigation.

Bibliography

Arezki, R., Matsumoto, A., Zhao, H., 2015. Commodity special feature. Technical Report. URL: https://www.imf.org/external/np/res/commod/pdf/WEOSpecialOCT15.pdf.

Arya, L.M., Leij, F.J., Shouse, P.J., van Genuchten, M.T., 1999. Relationship between the hydraulic conductivity function and the particle-size distribution. Soil Science Society of America Journal 63, 1063. URL: https://www.soils.org/publications/sssaj/abstracts/63/5/1063, doi:10.2136/sssaj1999.6351063x.

Augier, F., Idoux, F., Delenne, J., 2010. Numerical simulations of transfer and transport properties inside packed beds of spherical particles. Chemical Engineering Science 65, 1055–1064. URL: http://linkinghub.elsevier.com/retrieve/pii/S0009250909006629, doi:10.1016/j.ces.2009.09.059.

Bao-hua, Y., Ai-xiang, W.U., Huai-chun, J., Xue-song, C., 2008. Evolvement of permeability of ore granular media during heap leaching based on image analysis. Transactions of Nonferrous Metals Society of China 18, 426–431.

Barker, D., Parameswaran, G., Neethling, S., 2012. SPH Simulation of Packed-beds and Columns Applied to Heap-leaching. 9th International Conference on CFD in the Minerals and Process Industries , 1–6.

Bear, J., 1969. Hydrodynamic dispersion, in: De Wiest, R. (Ed.), Flow Through Porous Media. Academic Press, pp. 109–200.

Bear, J., 1976. Dynamics of fluids in porous media.

Bear, J., 2018. Modeling phenomena of flow and transport in porous media. Springer.

Bear, J., Verruijt, A., 1987. Modeling groundwater flow and pollution. D. Reidel Publishing Company.

Belfort, B., Younes, A., Fahs, M., Lehmann, F., 2013. On equivalent hydraulic conductivity for oscillation-free solutions of Richard's equation. Journal of Hydrology 505, 202–217. doi:10.1016/j.jhydrol.2013.09.047.

Bennett, C., McBride, D., Cross, M., Gebhardt, J., 2012. A comprehensive model for copper sulphide heap leaching. Part 1 Basic formulation and validation through column test simulation. Hydrometallurgy 127-128, 150–161. URL: http://linkinghub.elsevier.com/retrieve/pii/S0304386X12001831, doi:10.1016/j.hydromet.2012.08.004.

Bird, R.B., Stewart, W.E., Lightfoot, E.N., 2002. Transport phenomena. volume 1. Second ed., John Wiley & Sons. doi:10.1017/CBO9781107415324.004, arXiv:arXiv:1011.1669v3.

Bouffard, S.C., 2003. Understanding the heap biooxidation of sulfidic refractory gold ores. Ph.D. thesis.

Bouffard, S.C., 2008. Agglomeration for heap leaching: Equipment design, agglomerate quality control, and impact on the heap leach process. Minerals Engineering 21, 1115–1125. URL: http://linkinghub.elsevier.com/retrieve/pii/S0892687508000368, doi:10.1016/j.mineng.2008.02.010.

Bouffard, S.C., Dixon, D.G., 2001. Investigative study into the hydrodynamics of heap leaching processes. Metallurgical and Materials Transactions B 32, 763–776. URL: http://www.springerlink.com/index/10.1007/s11663-001-0063-1, doi:10.1007/s11663-001-0063-1.

Bouffard, S.C., West-Sells, P.G., 2009. Hydrodynamic behavior of heap leach piles: Influence of testing scale and material properties. Hydrometallurgy 98, 136–142. URL: http://linkinghub.elsevier.com/retrieve/pii/S0304386X0900084X, doi:10.1016/j.hydromet.2009.04.012.

Brooks, R., Corey, A., 1964. Hydraulic properties of porous media. Hydrology Papers, Colorado State University 3, 37 pp. URL: http://www.citeulike.org/group/1336/article/711012.

Bujalski, J., Tiller-Jefferey, R., Watling, H., Schwarz, M., 2003. CFD Modeling and Comparison with Experimental Residence Time Distributions in Single and Two Phase Flows. 3rd International Conference on CFD in the Minerals and Process Industries , 463–468.

Cariaga, E., Concha, F., Sepúlveda, M., 2005. Flow through porous media with applications to heap leaching of copper ores. Chemical Engineering Journal 111, 151–165. URL: http://linkinghub.elsevier.com/retrieve/pii/S1385894705000628, doi:10.1016/j.cej.2005.02.019.

Cariaga, E., Martínez, R., Sepúlveda, M., 2015. Estimation of hydraulic parameters under unsaturated flow conditions in heap leaching. Mathematics and Computers in Simulation 109, 20–31. doi:10.1016/j.matcom.2014.07.006.

Celia, M.A., Bouloutas, E.T., Zarba, R.L., 1990. A general mass-conservative numerical solution for the unsaturated flow equation. Water Resources Research 26, 1483–1496.

Cumming, B., Moroney, T., Turner, I., 2011. A mass-conservative control volume-finite element method for solving Richards' equation in heterogeneous porous media. BIT Numerical Mathematics 51, 845–864. doi:10.1007/s10543-011-0335-3.

de Andrade Lima, L., 2006. Liquid axial dispersion and holdup in column leaching. Minerals Engineering 19, 37–47. URL: http://linkinghub.elsevier.com/retrieve/pii/S089268750500172X, doi:10.1016/j.mineng.2005.05.020.

Deloitte, 2013. Tracking the trends 2014. The top 10 issues mining companies will face in the coming year. Technical Report. URL: http://www.deloitte.com/assets/Dcom-Ireland/LocalAssets/Documents/Energy/2013/ca{_}en{_}energy{_}Tracking{_}the{_}trends{_}2013{_}112812.pdf.

Dixon, D.G., 1992. Predicting kinetics of heap leaching with unsteady-state models. Ph.D. thesis. University of Nevada, Reno.

Dixon, D.G., 2003. Heap leach modeling — the current state of the art, in: Young, C., Alfantazi, A., Anderson, C., Dreisinger, D., Harris, B., James, A. (Eds.), Hydrometallurgy, TMS. pp. 289–314.

Dixon, D.G., Afewu, K., 2010. AMIRA P768A — module C (heap hydrology). Final Report. Technical Report. UBC.

Dixon, D.G., Afewu, K.I., 2011. Mathematical modelling of heap leaching under drip irrigation, in: Percolation leaching: The status globally and in southern Africa, Muldersdrift. pp. 255–284.

Extrand, C.W., 2015. Forces, pressures and energies associated with liquid rising in nonuniform capillary tubes. Journal of Colloid and Interface Science 450, 135–140. URL: http://dx.doi.org/10.1016/j.jcis.2015.03.007, doi:10.1016/j.jcis.2015.03.007.

Eymard, R., Gutnic, M., Hilhorst, D., 1999. The finite volume method for Richards equation. Computational Geosciences 3, 259–294. doi:10.1023/A:1011547513583.

Fagan, M., Sederman, A., Harrison, S., Johns, M., 2013. Phase distribution identification in the column leaching of low grade ores using MRI. Minerals Engineering 48, 94–99. URL: http://linkinghub.elsevier.com/retrieve/pii/S0892687512003421, doi:10.1016/j.mineng.2012.10.005.

Fagan, M.a., Ngoma, I.E., Chiume, R.a., Minnaar, S., Sederman, A.J., Johns, M.L., Harrison, S.T.L., 2014. MRI and gravimetric studies of hydrology in drip irrigated heaps and its effect on the propagation of bioleaching micro-organisms. Hydrometallurgy 150, 210–221. URL: http://dx.doi.org/10.1016/j.hydromet.2014.04.022, doi:10.1016/j.hydromet.2014.04.022.

Fala, O., Molson, J., Aubertin, M., Bussière, B., 2005. Numerical modelling of flow and capillary barrier effects in unsaturated waste. Mine Water and Environment 24, 172–185.

van Genuchten, M.T., 1980. A closed-form equation for predicting the hydraulic conductivity of unsaturated soils. Soil Science Society of America Journal 44, 892. doi:10.2136/sssaj1980.03615995004400050002x.

Ghorbani, Y., Becker, M., Mainza, A., 2011. Large particle effects in chemical/biochemical heap leach processes — A review. Minerals Engineering 24, 1172–1184. URL: http://linkinghub.elsevier.com/retrieve/pii/S0892687511001178http://www.sciencedirect.com/science/article/pii/S0892687511001178, doi:10.1016/j.mineng.2011.04.002.

Ghorbani, Y., Franzidis, J.p., Petersen, J., 2015. Heap leaching technology — current state , innovations and future directions : A review. Mineral Processing and Extractive Metallurgy Review 7508, 1–83. doi:10.1080/08827508.2015.1115990.

Ghorbani, Y., Petersen, J., Becker, M., Mainza, A.N., Franzidis, J.P., 2013. Investigation and modelling of the progression of zinc leaching from large sphalerite ore particles. Hydrometallurgy 131-132, 8–23. URL: http://linkinghub.elsevier.com/retrieve/pii/S0304386X12002216, doi:10.1016/j.hydromet.2012.10.004.

Guzman, A., Filippone, C., Uhrie, J., Green, C., 2002. Hydraulic parameter estimation from metallurgical column test data, in: SME Annual Meeting, SME. pp. 25–28.

Hairer, E., Norsett, S., G., W., 2008. Solving ordinary differential equations I. 2nd revise ed., Springer-Verlag.

Hassanizadeh, M., Gray, W., 1983a. General conservation equations for multi-phase systems: 1. Averaging procedure, in: Pinder, G. (Ed.), Flow through porous media. A Computational Mechanics Publication.

Hassanizadeh, M., Gray, W., 1983b. General conservation equations for multi-phase systems: 2. Mass, momentum, energy and entropy equations, in: Pinder, G. (Ed.), Flow Through Porous Media. A Computational Mechanics Publication.

Haverkamp, R., Vauclin, M., Touma, J., Wierenga, P., Vachaud, G., 1977. A comparison of numerical simulation models for one-dimensional infiltration. Soil Science Society of America Journal 41, 285–294.

Hindmarsh, A.C., 1983. ODEPACK, a systematized collection of ODE solvers, in: Stepleman, R.S. (Ed.), Vol. 1 of IMACS Transactions on Scientific Computation. Amsterdam, pp. 55–64.

Ilankoon, I., Cole, K., Neethling, S., 2013. Measuring hydrodynamic dispersion coefficients in unsaturated packed beds: Comparison of PEPT with conventional tracer tests. Chemical Engineering Science 89, 152–157. URL: http://linkinghub.elsevier.com/retrieve/pii/S0009250912006598, doi:10.1016/j.ces.2012.11.013.

Ilankoon, I., Neethling, S., 2012. Hysteresis in unsaturated flow in packed beds and heaps. Minerals Engineering 35, 1–8. URL: http://linkinghub.elsevier.com/retrieve/pii/S0892687512001975, doi:10.1016/j.mineng.2012.05.007.

Ilankoon, I., Neethling, S., 2013. The effect of particle porosity on liquid holdup in heap leaching. Minerals Engineering 45, 73–80. URL: http://linkinghub.elsevier.com/retrieve/pii/S0892687513000435, doi:10.1016/j.mineng.2013.01.016.

Ilankoon, I., Neethling, S., 2014. Transient liquid holdup and drainage variations in gravity dominated non-porous and porous packed beds. Chemical Engineering Science 116, 398–405. URL: http://linkinghub.elsevier.com/retrieve/pii/S0009250914002279, doi:10.1016/j.ces.2014.05.017.

Jafari, A., Zamankhan, P., Mousavi, S., Pietarinen, K., 2008. Modeling and CFD simulation of flow behavior and dispersivity through randomly packed bed reactors. Chemical Engineering Journal 144, 476–482. URL: http://linkinghub.elsevier.com/retrieve/pii/S1385894708004300, doi:10.1016/j.cej.2008.07.033.

John, L.W., 2011. The art of heap leaching — the fundamentals, in: Percolation leaching: The status globally and in southern Africa, Muldersdrift. pp. 17–43.

Kartha, S.A., Srivastava, R., 2012. Slow and fast transport in heap leaching of precious metals. Transport in Porous Media 94, 707–727. doi:10.1007/s11242-012-0020-2.

Khlaifat, A.L., 2008. Two-fluid mathematical model for compressible flow in fractured porous media. Latin American Applied Research 38, 213–225.

Lai, W., Ogden, F.L., 2015. A mass-conservative finite volume predictor-corrector solution of the 1D Richards' equation. Journal of Hydrology 523, 119–127. doi:10.1016/j.jhydrol.2015.01.053.

Lefebvre, R., Hockley, D., Smolensky, J., Gélinas, P., 2001. Multiphase transfer processes in waste rock piles producing acid mine drainage 1: Conceptual model and system characterization. Journal of contaminant hydrology 52, 137–64. URL: http://www.ncbi.nlm.nih.gov/pubmed/11695739.

Leij, F.J., Russell, W.B., Lesch, S.M., 1997. Closed-form expression for water retention and conductivity data. Ground Water 35, 848–858.

Lenhard, R., Parker, J., Mishra, S., 1989. On the Correspondence between Brooks-Corey and van Genuchten Models. Journal of Irrigation and Drainage Engineering 115, 744–751.

Levenspiel, O., 1999. Chemical reaction engineering. Third edit ed., John Wiley & Sons.

Manzini, G., Ferraris, S., 2004. Mass-conservative finite volume methods on 2-D unstructured grids for the Richards' equation. Advances in Water Resources 27, 1199–1215. doi:10.1016/j.advwatres.2004.08.008.

Mbonimpa, M., Aubertin, M., Chapuis, R.P., Bussière, B., 2002. Practical pedotransfer functions for estimating the saturated hydraulic conductivity. Geotechnical and Geological Engineering 20, 235–259. doi:10.1023/A:1016046214724.

McBride, D., Cross, M., Croft, N., 2006. Computational modelling of variably saturated flow in porous media with complex three-dimensional geometries. International journal for numerical methods in fluids 50, 1085–1117. URL: http://onlinelibrary.wiley.com/doi/10.1002/fld.1087/abstract.

McBride, D., Ilankoon, I.M., Neethling, S.J., Gebhardt, J.E., Cross, M., 2017. Preferential flow behaviour in unsaturated packed beds and heaps: Incorporating into a CFD model. Hydrometallurgy 171, 402–411. URL: http://dx.doi.org/10.1016/j.hydromet.2017.06.008, doi:10.1016/j.hydromet.2017.06.008.

Molson, J.W., Fala, O., Aubertin, M., Bussière, B., 2005. Numerical simulations of pyrite oxidation and acid mine drainage in unsaturated waste rock piles. Journal of contaminant hydrology 78, 343–71. URL: http://www.ncbi.nlm.nih.gov/pubmed/16039751, doi:10.1016/j.jconhyd.2005.06.005.

Mostaghimi, P., Tollit, B.S., Neethling, S.J., Gorman, G.J., Pain, C.C., 2013. A control volume finite element method for adaptive mesh simulation of flow in heap leaching. Journal of Engineering Mathematics , 111–121URL: http://link.springer.com/10.1007/s10665-013-9672-3, doi:10.1007/s10665-013-9672-3.

Moukalled, F., Mangani, L., Darwish, M., 2016. The finite volume method in computational fluid dynamics. Springer.

Mualem, Y., 1976. A new model for predicting the hydraulic conductivity of unsaturated porous media. Water Resources Research 12, 513–522. doi:10.1029/WR012i003p00513.

Nichol, C., Smith, L., Beckie, R., 2005. Field-scale experiments of unsaturated flow and solute transport in a heterogeneous porous medium. Water Resources Research 41, 1–11. doi:10.1029/2004WR003035.

Ogata, A., Banks, R.B., 1961. A solution of the differential equation of longitudinal dispersion in porous media. United States Government Printing Office, Washington.

Ogbonna, N., 2006. Mathematical modelling of agglomerate scale phenomena in heap bioleaching. Ph.D. thesis. University of Cape Town.

Ogbonna, N., Petersen, J., Dixon, D.G., 2005. HeapSim — unravelling the mathematics of heap bioleaching, in: Computational Analysis in Hydrometallurgy, 35th Annual Hydrometallurgy Meeting, pp. 225–240.

O'Kane Consultants Inc, 2000. Demonstration of the application of unsaturated zone hydrology for heap leach optimization, Industrial research assistance program contract #332407. Technical Report.

Orr, S., Vesselinov, V., 2002. Enhanced heap leaching — part 2 : applications. Mining Engineering , 33–38.

Pan, C., Prins, J.F., Miller, C.T., 2004. A high-performance lattice Boltzmann implementation to model flow in porous media. Computer Physics Communications 158, 89–105. URL: http://linkinghub.elsevier.com/retrieve/pii/S0010465504000049, doi:10.1016/j.cpc.2003.12.003.

Pantelis, G., Ritchie, A., Stepanyants, Y., 2002. A conceptual model for the description of oxidation and transport processes in sulphidic waste rock dumps. Applied Mathematical Modelling 26, 751–770. URL: http://linkinghub.elsevier.com/retrieve/pii/S0307904X01000853, doi:10.1016/S0307-904X(01)00085-3.

Petersen, J., 2015. Heap leaching as a key technology for recovery of values from low-grade ores - A brief overview. Hydrometallurgy URL: http://dx.doi.org/10.1016/j.hydromet.2015.09.001, doi:10.1016/j.hydromet.2015.09.001.

Petersen, J., Dixon, D., 2007. Modelling zinc heap bioleaching. Hydrometallurgy 85, 127–143. URL: http://linkinghub.elsevier.com/retrieve/pii/S0304386X06002283, doi:10.1016/j.hydromet.2006.09.001.

Petrova, T., 2014. Revised release on surface tension of ordinary water substance. Technical Report June. The International Association for the Properties of Water and Steam. Moscow.

Philip, J., 1957a. The theory of infiltration: 1. The infiltration equation and its solution. Soil Science 83, 345–358.

Philip, J., 1957b. The theory of infiltration: 2. The profile of infinity. Soil Science 83, 435–448.

Pop, I.S., Radu, F., Knabner, P., 2004. Mixed finite elements for the Richards' equation: Linearization procedure. Journal of Computational and Applied Mathematics 168, 365–373. doi:10.1016/j.cam.2003.04.008.

Reddy, B.D., 2007. Introductory functional analysis with applications to boundary value problems and finite elements.

Richards, L.A., 1931. Capillary conduction of liquids through porous mediums. Journal of Applied Physics 1, 318–333. doi:10.1063/1.1745010, arXiv:/dx.doi.org/10.1063/1.1745010.

Richardson, L.F., 2007. Weather prediction by numerical process. 2nd ed., Cambridge University Press, New York.

Robertson, S., 2017. Development of an integrated heap leach solution flow and mineral leaching model. Hydrometallurgy 169, 79–88. URL: http://dx.doi.org/10.1016/j.hydromet.2016.12.010, doi:10.1016/j.hydromet.2016.12.010.

Roman, R.J., Benner, B.R., Becker, G.W., 1974. Diffusion model for heap leaching and its application to scale-up. Transactions of the Society of Mining Engineers of AIME 256, 247–252.

Rucker, D.F., Schindler, A., Levitt, M.T., Glaser, D.R., 2009. Three-dimensional electrical resistivity imaging of a gold heap. Hydrometallurgy 98, 267–275. URL: http://linkinghub.elsevier.com/retrieve/pii/S0304386X09001261, doi:10.1016/j.hydromet.2009.05.011.

Sahimi, M., 1993. Flow phenomena in rocks — from continuum models to fractals, percolation, cellular-automata, and simulated annealing. Reviews of Modern Physics 65, 1393–1534. doi:10.1103/RevModPhys.65.1393.

Schaap, M., Shouse, P., Meyer, P., 2003. Laboratory measurements of the unsaturated hydraulic properties at the vadose zone transport field study site. Technical Report May. Pacific Northwest National Laboratory.

Schaap, M.G., Leij, F.J., Van Genuchten, M.T., 1998. Neural network analysis for hierarchical prediction of soil hydraulic properties. Soil Science Society of America Journal 62, 847–855. URL: isi:000075455900001.

Schaap, M.G., Leij, F.J., Van Genuchten, M.T., 2001. Rosetta: a computer program for estimating soil hydraulic parameters with hierarchical pedotransfer functions. Journal of Hydrology 251, 163–176. doi:10.1016/S0022-1694(01)00466-8.

Sheikhzadeh, G., Mehrabian, M., Mansouri, S., Sarrafi, A., 2005. Computational modelling of unsaturated flow of liquid in heap leaching—using the results of column tests to calibrate the model. International Journal of Heat and Mass Transfer 48, 279–292. URL: http://linkinghub.elsevier.com/retrieve/pii/S0017931004003746, doi:10.1016/j.ijheatmasstransfer.2004.08.007.

Smith, G., 1985. Numerical solution of partial differential equations: finite difference methods. 3rd ed., Oxford University Press, New York.

van Staden, P.J., Naseri, A., Petersen, J., 2017. Heapsim modelling of high temperature heap bioleaching data, in: Proceedings of ALTA 2017 Nickel-Cobalt-Copper Sessions, ALTA Metallurgical Services, Perth. pp. 210–246.

van Staden, P.J., Petersen, J., 2019. The effects of simulated stacking phenomena on the percolation leaching of crushed ore, Part 2: Stratification. Minerals Engineering 131, 216–229. doi:10.1016/j.mineng.2018.11.021.

Strauss, W.A., 2008. Partial differential equations: an introduction. 2nd ed., John Wiley & Sons.

Tracy, F.T., 1995. 1-D, 2-D, and 3-D analytical solutions of unsaturated flow in groundwater. Journal of Hydrology 170, 199–214. URL: http://www.sciencedirect.com/science/article/pii/002216949402674Z, doi:10.1016/0022-1694(94)02674-Z.

Tracy, F.T., 2007. Three-dimensional analytical solutions of Richards' equation for a box-shaped soil sample with piecewise-constant head boundary conditions on the top. Journal of Hydrology 336, 391–400. doi:10.1016/j.jhydrol.2007.01.011.

Tracy, F.T., 2011. Analytical and numerical solutions of Richards' equation with discussions on relative hydraulic conductivity. Hydraulic Conductivity-Issues, Determination and … URL: http://cdn.intechopen.com/pdfs-wm/23451.pdf.

Trang, S.C., Stephens, D.W., Schwarz, M.P., 2006. Modelling heat transfer in the dripper zone of a heap leaching operation, in: Fifth International Conference on CFD in the Process Industries, CSIRO, Melbourne. pp. 1–6.

Tupikina, O.V., Minnaar, S.H., Rautenbach, G.F., Dew, D.W., Harrison, S.T., 2014. Effect of inoculum size on the rates of whole ore colonisation of mesophilic, moderate thermophilic and thermophilic acidophiles. Hydrometallurgy 149, 244–251. URL: http://dx.doi.org/10.1016/j.hydromet.2013.10.010, doi:10.1016/j.hydromet.2013.10.010.

Watling, H., 2006. The bioleaching of sulphide minerals with emphasis on copper sulphides — A review. Hydrometallurgy 84, 81–108. URL: http://linkinghub.elsevier.com/retrieve/pii/S0304386X06001125, doi:10.1016/j.hydromet.2006.05.001.

Watling, H., 2013. Chalcopyrite hydrometallurgy at atmospheric pressure: 1. Review of acidic sulfate, sulfate-chloride and sulfate-nitrate process options. Hydrometallurgy 140, 163–180. URL: http://linkinghub.elsevier.com/retrieve/pii/S0304386X13001989, doi:10.1016/j.hydromet.2013.09.013.

Watling, H., 2014. Chalcopyrite hydrometallurgy at atmospheric pressure: 2. Review of acidic chloride process options. Hydrometallurgy 146, 96–110. URL: http://linkinghub.elsevier.com/retrieve/pii/S0304386X14000693, doi:10.1016/j.hydromet.2014.03.013.

Wolfram, S., 1982. Cellular automata as simple self-organizing systems. Caltech preprint CALT-68-938 URL: http://cds.cern.ch/record/140047.

Wu, A., Yin, S., Yang, B., Wang, J., Qiu, G., 2007. Study on preferential flow in dump leaching of low-grade ores. Hydrometallurgy 87, 124–132. URL: http://linkinghub.elsevier.com/retrieve/pii/S0304386X07000643, doi:10.1016/j.hydromet.2007.03.001.

Appendix A

Program listings

The source code for TOEM, Richards1D, Richards2D, PFRP, and the stochastic model can be found on Github under the following link: https://github.com/mobius-eng/phd-source-code and the following doi: http://dx.doi.org/10.25375/uct.7645127.. The source code is published under GPL 2+ license.

TOEM source code

The program is written in Fortran 2008 and needs to be compiled to a dynamically linked library (DLL on Windows). The code requires ODEPACK. The program consists of the following modules:

- `GENERAL`: General-purpose data and procedures.
- `UNSATURATED`: Procedures implementing the van Genuchten unsaturated model.
- `TOEM`: Driver procedure of the TOEM.
- `TOEM.xlsm`: Excel spreadsheet, interface. Note, the linking to the DLL is done under the assumption that the DLL is compiled into 64 bit format and MS Office 64 bit is used.

Richards1D source code

The program is written in Fortran 2008 and needs to be compiled to a dynamically linked library (DLL on Windows). The code requires ODEPACK. The program consists of the following modules:

- `GENERAL`: General-purpose data and procedures.
- `GROWING_ARRAY_MOD`: Procedures implementing the array that can extend its size. It is used to implement varying inlet flow rate.
- `INLETFLOW_MODULE`: Procedures implementing various regimes of the inlet flow.
- `UNSATURATED`: Procedures implementing the van Genuchten unsaturated model.
- `DARCY_MODULE`: Implementation of the finite volume method for the Richards equation.
- `RUNRICHARDS`: Driver procedures for DLL.
- `Richards1D.xlsm`: Excel spreadsheet, interface. Note, the linking to the DLL is done under the assumption that the DLL is compiled into 64 bit format and MS Office 64 bit is used.

Richards2D source code

The program is written in Fortran 2008 and needs to be compiled to a dynamically linked library (DLL on Windows). The code requires ODEPACK. The program consists of the following modules:

- `GENERAL`: General-purpose data and procedures.
- `CONSTANTS`: Constants defining spatial and temporal discretisation.
- `GEOMETRY2D`: Procedures operating on the two-dimensional domain and extracting finite volume method features.
- `INLETFLOW_MOD`: Procedures implementing various regimes of the inlet flow.
- `UNSATURATED`: Procedures implementing the van Genuchten unsaturated model.
- `DARCY_MOD`: Implementation of the finite volume method for the Richards equation.
- `DRIVER`: Driver procedures for DLL.
- `Richards2D.xlsm`: Excel spreadsheet, interface. Note, the linking to the DLL is done under the assumption that the DLL is compiled into 64 bit format and MS Office 64 bit is used.

PFRP source code

The program is written in Fortran 2008 and needs to be compiled to a dynamically linked library (DLL on Windows). The program consists of the following modules:

- `ENV`: Defines constants determining calculation precision.
- `CSTR`: Defines the CSTR with a reaction.
- `GAUSS_SEIDEL`: Implements the Gauss-Seidel method.
- `NEWTON`: Implements the Newton method.
- `MPFP`: Contains the driver function for the model.
- `PLUG_FLOW_IN_PARALLEL`: Contains exportable functions that will be visible in the DLL.
- `PFRP.xlsm`: Note, the linking to the DLL is done under the assumption that the DLL is compiled into 64 bit format and MS Office 64 bit is used.

Stochastic model source code

The program is written in Clojure 1.8 and is used directly from the REPL (read-evaluate-print-loop). The program depends on `quil` 2.6 and `docjure` 1.11 libraries for visualization and saving the data into an Excel spreadsheet respectively. The program consists of the following namespaces:

- Namespace `lattice`: Contains the definition of the lattice structure.
- Namespace `simulation`: Contains functions implementing model simulation.
- Namespace `plot`: Implements simple plotting facilities to display "mass" and "RTD" plots in the program window.
- Namespace `simulation-visualization`: Implements lattice and simulation visualization.
- Namespace `core`: Contains the driver of the model.

Appendix B

Gravimetric data

The raw gravimetric data can be found online under the following link doi: http://dx.doi.org/10.25375/uct.7644347. The repository contains the following files:

- `gravimetric-general.csv`: General information about blends, packing, column flooded weight, and etc.
- `gravimetric-PSD.csv`: Particle size distribution of the blends.
- `gravimetric-PSD-fines.csv`: Particle size distribution of the -1.4 mm fraction of the sample.
- `gravimetric-steady-state-weight.csv`: Steady state weights of blends under various irrigation rates.
- `gravimetric-intermittent-*.csv`: The record of the intermittent irrigation of GGS075(P33) and GGS025(P34) columns.
- `gravimetric-infiltration-weight.csv`: The record of the infiltration of the first set of columns (GGS075(P11)–GGS097(P14)).
- `gravimetric-drainage-*.csv`: The record of the drainage experiments.

Appendix C

RTD data

The raw RTD data and the details of the transformation of this data to the F- and E-curves can be found online under the following link doi: http://dx.doi.org/10.25375/uct.7645043. The repository contains the following files:

- `RTD-meta.csv`: General information on RTD experiments.
- `RTD-calibration-measurements.csv`: The data that was used to fit the conductivity-voltage curve; conductivity meter calibration.
- `RTD-calibration-fit.csv`: The values of the coefficients of the conductivity-voltage curve that was found as a fit from the calibration measurements.
- `Bouffard-U10Z058.csv`: The table representing the F-curve of the RTD experiments from Bouffard and Dixon (2001). The data was obtained by tracing the plot in the publication.
- `RTD-P11-P14-3.csv` : Raw time-voltage data from RTD experiments of GGS075(P11) – GGS025(P14) under low irrigation flow rate.
- `RTD-P11-P14-20.csv`: Raw time-voltage data from RTD experiments of GGS075(P11) – GGS025(P14) under high irrigation flow rate.
- `RTD-P21-P22-3.csv` and `RTD-P23-P24-3.csv`: Raw time-voltage data from RTD experiments of GGS075(P21) – GGS040(P24) under low irrigation flow rate.

- `RTD-P21-P22-10.csv` and `RTD-P23-P24-10.csv`: Raw time-voltage data from RTD experiments of GGS075(P21) – GGS040(P24) under high irrigation flow rate.

- `RTD-analysis.nb`: Mathematica notebook detailing the transformation of the raw time-voltage data to the dimensionless F- and E-curves.